SCIENCE CHINA Chemistry



INVITED REVIEWS

https://doi.org/10.1007/s11426-024-2458-3

Recent progress in metal-organic frameworks (Part II—material application)

Jiandong Pang^{1†}, Wentao Jiang^{2†}, Xue-Wen Zhang^{3†}, Hao-Long Zhou^{4†}, Yuxiu Sun^{5†}, Wei Gong^{6†}, Bin Wang^{7†}, Fuyin Ma^{7†}, Linwei He^{7†}, Long Chen^{7†}, Qiang Chen^{8†}, He-Qi Zheng^{9†}, Yuanjing Cui^{9†}, Wen-Jie Shi^{10†}, Chao Zhang^{10†}, Mei Wang^{10†}, Yue-Biao Zhang^{2*}, Jie-Peng Zhang^{3*}, Chongli Zhong^{5*}, Yong Cui^{6*}, Shuao Wang^{7*}, Jian-Rong Li^{8*}, Guodong Qian^{9*}, Tong-Bu Lu^{10*}, Huan Pang^{11*} & Xian-He Bu^{1*}

¹School of Materials Science and Engineering, Nankai University, Tianjin 300350, China
²School of Physical Science and Technology, ShanghaiTech University, Shanghai 201210, China
³MOE Key Laboratory of Bioinorganic and Synthetic Chemistry, GBRCE for Functional Molecular Engineering, School of Chemistry, IGCME,
Sun Yat-sen University, Guangzhou 510275, China
⁴Department of Chemistry, Shantou University, Shantou 515063, China

⁵School of Chemical Engineering and Technology, Tiangong University, Tianjin 300387, China

⁶School of Chemistry and Chemical Engineering, Shanghai Jiao Tong University, Shanghai 200240, China

⁷State Key Laboratory of Radiation Medicine and Protection, School for Radiological and Interdisciplinary Sciences, Soochow University,

Suzhou 215123, China

⁸College of Materials Science & Engineering, Beijing University of Technology, Beijing 100124, China
⁹State Key Laboratory of Silicon and Advanced Semiconductor Materials, Cyrus Tang Center for Sensor Materials and Applications, School of Materials Science & Engineering, Zhejiang University, Hangzhou 310027, China
¹⁰Institute for New Energy Materials and Low Carbon Technologies, School of Materials Science and Engineering, Tianjin University of Technology, Tianjin 300384, China

¹¹School of Chemistry and Chemical Engineering, Yangzhou University, Yangzhou 225009, China

Received October 11, 2024; accepted December 5, 2024; published online January 3, 2025

As a class of functional crystalline porous materials, metal-organic frameworks (MOFs) gained rapid development in the past three decades and a large number of MOFs with ordered structures, high surface areas, and functionalized channels have been investigated. MOFs and MOF-derived/composite materials show great potential in many application fields. In this review, we discussed the main applications of MOFs and MOF-derived/composite materials in small molecule storage, separation, luminescence, sensing, multitype catalysis, and energy storage. In addition, challenges and problems in the future research of MOFs-related fields are also discussed.

metal-organic frameworks, storage and separation, sensing and detection, multitype catalysis, energy storage

Citation: Pang J, Jiang W, Zhang XW, Zhou HL, Sun Y, Gong W, Wang B, Ma F, He L, Chen L, Chen Q, Zheng HQ, Cui Y, Shi WJ, Zhang C, Wang M, Zhang YB, Zhang JP, Zhong C, Cui Y, Wang S, Li JR, Qian G, Lu TB, Pang H, Bu XH. Recent progress in metal-organic frameworks (Part II—material application). Sci China Chem, 2025, 68, https://doi.org/10.1007/s11426-024-2458-3

Equally contributed to this work

^{*}Corresponding authors (email: zhangyb@shanghaitech.edu.cn; zhangjp7@mail.sysu.edu.cn; zhongchongli@tiangong.edu.cn; yongcui@sjtu.edu.cn; shuaowang@suda.edu.cn; jrli@bjut.edu.cn; gdqian@zju.edu.cn; lutongbu@tjut.edu.cn; panghuan@yzu.edu.cn; buxh@nankai.edu.cn)

CONTENTS

1	Intro	oduction	2
2	Sma	all molecule storage	
		Methane storage	3
		Hydrogen storage	3
		Atmospheric water harvesting	
		Acetylene storage	5
3		aration	ϵ
	-	Adsorptive separation of small molecules	6
		Small molecule separation through membranes	ç
		Enantioseparation	14
	3.4	Extraction of radioactive substances	17
	3.5	Capture and separation of environmental pollutants	20
4		ical performance	22
	4.1	Luminescence mechanism	23
	4.2	White emission	23
5	Sens	sing and detection	24
	5.1	Temperature	24
	5.2	Pressure	25
	5.3	Small molecules or ions	26
6	Che	mocatalysis	27
	6.1	Coupling reactions	27
	6.2	Catalytic asymmetric reactions	29
	6.3	Catalytic biomass conversion	33
	6.4	CO ₂ fixation	36
7	Pho	tocatalysis	38
	7.1	Photocatalytic CO ₂ reduction	39
		Photocatalytic hydrogen production	40
	7.3	Photocatalytic organic transformation	43
8	Elec	etrochemistry and electrocatalysis	45
	8.1	Electrochemistry	45
		Electrocatalytic reactions	47
9	Ene	rgy storage	50
	9.1	Cathode materials	50
	9.2	Anode materials	52
		Separator film	52
		Supercapacitor	52
10	Su	mmary and outlooks	53

1 Introduction

Metal-organic frameworks (MOFs), also known as porous coordination polymers (PCPs) or porous coordination networks (PCNs), are a class of novel crystalline porous materials that have attracted more and more attention. MOFs are composed of metal ions or clusters coordinated to organic ligands, creating porous structures with high surface areas and tunable pore environments. In the past three decades, enormous research results related to the synthesis, structure, and property studies of MOFs have been reported, since the concept of MOF was established in the early 1990s. For a better reviewing of the MOFs field, we briefly divided the MOFs research field into two parts: material preparation and

material application. In our previous review, we systematically summarized the structural design principles and strategies, synthesis methods, and structure characteristics of MOFs, as well as the preparation of MOF-derived and composite materials, and MOF-based films/membranes. As a kind of novel functional materials, MOFs show versatility in applications across various research fields, due to their diverse composition, structure, active sites, and pore environment. Their well-defined and customizable structures allow for the establishment of clear structure-property relationships, which is crucial for the design of new materials.

MOFs are well-known for their ultra-high specific surface areas and diverse pore structures, and most of the application research of MOFs is closely related to their porous structures. For example, the open pores in MOFs provide available space for the adsorption and enrichment of guest molecules, which is the basis for the application of MOFs in small molecule storage. By controlling the pore size of MOFs or introducing specific active sites showing discriminatory interactions with different guest molecules, efficient separation of small molecule mixtures can be achieved. Introducing corresponding catalytic active centers within the framework can achieve activation and catalytic conversion of guest molecules enriched in the pores. In addition, the pores in MOFs also provide the necessary space for structural changes, making it possible to generate dynamic response behavior under external stimuli, which is crucial for sensing and detection applications. Therefore, the regulation and optimization of the property of MOFs are mainly based on the control of their pore structures and precise regulation of the pore microenvironments. Herein, we provide a detailed review of research on the properties and potential applications of MOF materials in small molecule storage, separation, optical performance, sensing and detection, chemocatalysis, photocatalysis, electrocatalysis, and energy storage. We hope this review will stimulate further research interest in developing MOF materials with excellent performances and push forward the application of MOFs.

2 Small molecule storage

Small molecules are of great importance in the new era of carbon neutrality [1]: (1) H_2 is the cleanest secondary energy gas-energy storage from solar photovoltaic, wind power, and nuclear energy for zero-emission vehicular applications; (2) CH_4 is a primary energy gas cleaner than those of gasoline or diesel as an alternative internal combustion engine (ICE) fuel with combustion calorific value and less particulate matter or carbon emission for greener transportation; (3) H_2O is an ideal heat carrier used in the adsorptive thermal battery, and the indoor humidity control also required energy-efficient

dehumidifier, fresh water is daily-life needed, especially for arid area and islands, where water harvesting from atmospheric air will play an important role; (4) industrial gases, such as C₂H₂, with the caution of explosive risk, which demands safer storage technologies with the retention of high purity.

Porous materials for small molecule storage were primarily explored using zeolites [2] and activated carbons [3]. However, these materials suffered from limited porosity and challenges in controlling pore size and multifunctionality, which impeded the development of high-performance storage solutions. Featuring high surface area, defined gas adsorptive sites, tunable pore metrics, and multivariate functionalities, MOFs are designable porous materials aiming for small molecule storage with high uptakes, optimal working capacity, and lower regeneration energy consumption.

The tunable pore structures allow for the precise design of both high specific surface area (>4,000 m² g⁻¹) and narrow pore size distribution (0.8 to 1.5 nm) for gas storage [4,5]. The ultra-high surface area provides a large number of adsorption sites for gas molecules. Well-designed pores can provide more effective gas diffusion and reduce the energy required for gas adsorption or desorption. The interplay between these factors maximizes the capacity for gas adsorption while maintaining a balance between the accessibility of pores and the strength of interactions with gas molecules, making MOFs ideal candidates for small molecule storage applications.

2.1 Methane storage

In comparison with compressed natural gas (CNG) and liquefied natural gas (LNG), adsorbed natural gas (ANG) has been considered to be more environmentally friendly and safer on-board storage of methane by filling the tank with porous materials to facilitate the physical adsorption [6]. MOFs have been intensively studied for the improvement of gas uptake, enhancement of adsorption affinity, and, ultimately, optimization of working capacity. At present, delicate control of MOF structures is well-excised in the finetuning gas uptake isotherms for balancing volumetric and gravimetric working capacity in the working pressures ranges of 5.8–60, 5.8–80, and 5.8–200 bar.

The hierarchical pore structure of MAF-38, composed of single-wall nanocages, has appropriately sized and shaped organic binding sites with methane storage working capacity of 197 cm³_{STP} cm⁻³ at 298 K and 5–80 bar [7]. The design of cavities to enhance methane affinity, and the introduction of mesopores, have led to increasingly higher working capacities. In 2017, a series of multicomponent MOFs with different topologies (**muo**, **umt**, **ith-d**, and **ott**) were synthesized by mixing bitopic and tritopic linkers, termed

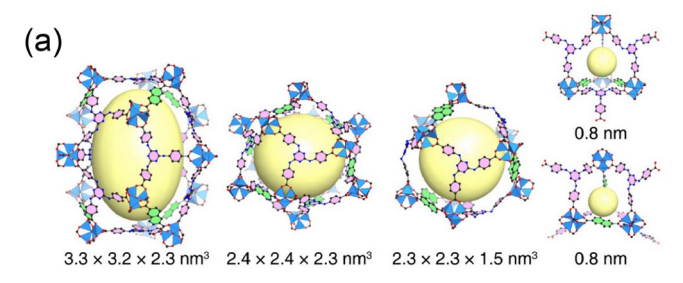
ST-1, -2, -3, and -4 [8]. Incorporating linkers with different lengths, angles, and coordination numbers allows the systematic engineering of pore metrics. Strikingly, ST-2 surpassed all previously reported records in porous materials, achieving a volumetric working capacity of 289 cm³_{STP} cm⁻³ within the pressure range of 5–200 bar at 298 K (Figure 1a, b).

Through subtle structural and chemical adjustments, NJU-Bai 43 demonstrated an optimized methane storage working capacity of 198 cm³_{STP} cm⁻³ at 298 K and 65 bar [9]. By using an extended linker with high density of functional nitrogen sites, UTSA-110a demonstrated exceptional gravimetric and volumetric working capacities of 317 and 190 cm³_{STP} cm⁻³, respectively [10]. The incorporation of functional groups or open metal sites (OMSs) possessing strong interactions with methane molecules can effectively regulate the working capacity of methane storage for the framework [11-13]. An electron-withdrawing fluoro-functional group was added to a Zr-based MOF to synthesize ZJU-800, demonstrating a methane storage capacity of 10.0 mmol g⁻¹ at 65 bar [11]. FJU-101a functionalized with naphthalene diimide groups, has a methane storage capacity of cm³_{STP} cm⁻³ at 298 K and 65 bar [12].

The multivariate (MTV) strategy allows elaborate controlling over the pore environment through the incorporation of multiple linkers with various functionalities [14]. MTV-MOFs constructed from a combination of functionalized (pyrimidine-containing) and unfunctionalized organic linkers, including NOTT-101a (0%), UTSA-77a (20%), UTSA-78a (66.7%), UTSA-79a (80%), and UTSA-76a (100%), showed enhanced methane storage capacities as the proportion of functionalized linkers increased [15,16]. The immobilized functional groups notably improved methane storage capacities at 65 bar and these MOFs demonstrated excellent methane storage working capacities of 188–197 cm³_{STP} cm⁻³ (Figure 1c).

With no framework interpenetration observed, ST-150 exhibits a significantly improved volumetric deliverable capacity of 244 cm 3 _{STP} cm $^{-3}$ at 298 K, representing a ~70% enhancement over its interpenetrated counterpart, MOF-150 [17]. Precise manipulation of breathing behavior for MIL-53(Al) type MOFs has been achieved by introducing hydrogen bonding sites, resulting in increased deliverable capacity for methane storage of 164 cm 3 _{STP} cm $^{-3}$ or 118 mg g $^{-1}$ between 5.8 and 65 bar at 298 K [18], close to the record flexible MOF, Co-BDP, of 197 cm 3 _{STP} cm $^{-3}$. By adjusting factors such as gas pressure, temperature, and density, the adsorption capacity of these MOFs can be further optimized.

Replaceable coordination sites enable post-synthetic modifications (PSM) through reversible attachment of spacers with varying lengths and functionalities [19–25]. A durable Zr-based MOF, named LIFM-28, has been utilized to fine-tune the functionalities to obtain LIFM-82 with high



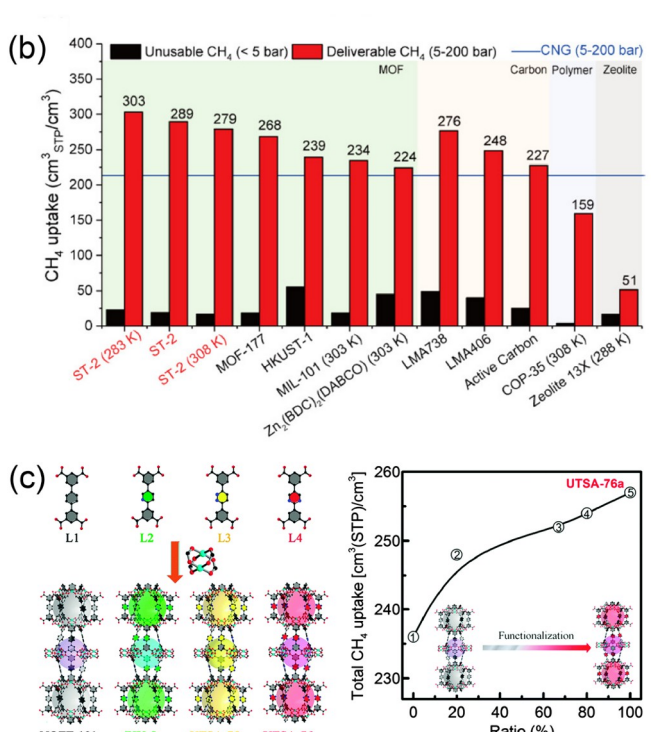


Figure 1 (Color online) (a) Engineering of pore geometry of ST-2. (b) Comparison of methane total uptake of benchmark MOFs. Reproduced with permission from Ref. [8]. Copyright@2017, American Chemical Society. (c) The fine-tuning of methane total uptake through MTV strategy. Reproduced with permission from Ref. [15]. Copyright@2015, Royal Society of Chemistry.

volumetric working capacity of 218 cm³_{STP} cm⁻³ at 298 K and 5–80 bar [26].

Introducing greater structural complexity can incorporate more variables, enabling finer control over methane storage capacity adjustments. A semi-rigid tricarboxylate ligand, H₃TATAB, was chosen to create a zirconium-based **spe**-MOF, exhibiting a novel (3,3,12,12)-c nondefault topology, demonstrates increased structural complexity, hierarchical micropores, OMSs, and electronegative groups on pore surfaces, leading to enhanced methane storage capacity [27]. Isoreticular nine-connected trinuclear iron-based Fe-**ncb**-MOFs without OMSs were designed and exhibited remarkable gravimetric and volumetric methane storage capacities [28]. Utilizing a mixed multinuclear cluster strategy, three new heterometallic MOFs (SNNU-328–330) were developed, offering a diverse range of OMSs and large cluster

sizes [29].

Overall, the delicate control of MOF structures has shown a positive impact in the enhancement of methane storage working capacity, but the scale-up synthesis, monolith shaping, and evaluation of ANG cylinder prototype are yet to be further investigated, heading to practical industry applications (Table 1) [30,31].

2.2 Hydrogen storage

MOFs hold great promise for hydrogen storage based on physical adsorption for high deliverable capacity (up to 14 wt%), fast adsorption kinetics, and decent cycling durability, in comparison with the metal hydride and organic liquid-based on chemical reactions [4,32,33]. Well-defined adsorptive sites, high surface area, large pore volumes, and appropriate pore geometry are the keys to high hydrogen uptakes [34,35].

The delicate control of pore sizes and shapes in the isoreticular series of [Ni₃(OH)(COO)₆L₃]-based MOFs with **ncb** net have shown over 7 wt% of H₂ uptake [36,37]. In 2020, Zhang *et al.* [38] explored the relationship between pore volume and hydrogen storage capacity in MOFs, deriving empirical equations to predict hydrogen storage capacity based on pore geometry. By applying these equations, the Zr-MOF NPF-200 demonstrates exceptional hydrogen adsorption capacity (65.7 mmol g⁻¹) at 77 K and a remarkable volumetric working capacity of 37.2 g L⁻¹ between 100 and 5 bar at 77 K. A highly stable microporous Al(III)-base MOF, named BUT-22, was synthesized, exhibiting gravimetric H₂ uptakes of 12 wt% and gravimetric H₂ deliverable capacity of 11.6 wt% assuming temperature and pressureswing operation between 100 bar–77 K and 5 bar–160 K [30].

Recently, the new observation of back donating of $\rm H_2$ binding to $\rm Cu^I$ has shown a significant enhancement in the heat of adsorption (up to 32 kJ mol⁻¹) and high hydrogen storage capacity of $10.4~\rm g~L^{-1}$ from 233 K/100 bar to 296 K/5 bar [39]. On the other hand, triptycene linkers have shown high hydrogen uptakes both in MOFs [4] and covalent-organic frameworks (COFs) [40], revealing a deliberate manipulation of organic linkers and their functionalities could be crucial [41].

2.3 Atmospheric water harvesting

As the world's population and energy demand continue to grow, the shortage of freshwater resources becomes increasingly apparent, especially in arid areas with extreme water shortages. In underdeveloped arid areas, compared with desalination plant or water conservancy projects with complex processes and high costs, water harvested from the atmosphere by absorbent is a more efficient method of

Table 1	The representative	MOFs with optimized	d methane storage	working	capacity under	various	working	pressure	ranges (C_{vol} ,	volumetric	working
capacity;	C_{gray} , gravimetric v	working capacity)										

MOFs	$C_{\rm vol}~({\rm cm}^3~{\rm cm}^{-3})$	$C_{\rm grav}~({\rm mg~g}^{-1})$	P (bar)	T (K)	Ref.
MAF-38	197	227	5-80	298	[7]
LIFM-82	218	169	5-80	298	[26]
ST-2	289	567	5–200	298	[8]
NJU-Bai 43	198	_	5–65	298	[9]
UTSA-76a	187	267	5.8-65	298	[16]
UTSA-110a	190	317	5.8–65	298	[10]
ZJU-800a	-	110	5–65	298	[11]
FJU-101a	144	122	5–65	298	[12]
spe-MOF	183	_	5-80	298	[27]
ST-150	244	_	5.8-200	298	[17]
BUT-22	178	334	5-80	296	[30]
Fe-ncb-ABDC	196	302	5-80	298	[28]
SNNU-329	156	_	5-80	298	[29]
NPF-200	207	380	5–100	296	[31]
Zr -fcu- H	187	_	5-80	298	[13]

capturing water, studied in depth in the past decade based on indicators such as adsorption capacity, operating humidity, adsorption and desorption rate, and regeneration energy consumption [42–46].

Exceptional chemical stabilities are essential for atmospheric water harvesting, exemplified by high-valency MOFs based on $Al^{III}/Cr^{III}/Zr^{IV}/V^{III}$ metal centers [47]. Modification of terminal ligands on the 9-connected Zr_6 cluster has shaped the water adsorption isotherm in serials of (6,9)-connected Zr MOFs, BUT-46F, -46A, -46W, and -46B (Figure 2a, b) [48] (Table 2). High water uptake capacity, steep uptake at low RH, and excellent durability were observed in (8,8)-connected Zr MOFs, unraveling strong water binding initiated from the narrow confinement space (Figure 2c, d) [49]. Gigantic Al_{24} clusters have been utilized in the construction of 12-connected robust MOFs, FDM-92 and FDM-93, by post-synthetic linker exchanges of FDM-91, which have shown exceptional water harvesting capacity (up to 0.53 g g⁻¹) and outstanding cycling performance (Figure 2e–g) [50].

Engineering of MOF materials including scale-up synthesis, composite, shaping and evaluation of prototypes under outdoor climate have been studied in China. A 2D MOF, MWH-1, has shown the highest water uptake capacity of 259 cm³ cm⁻³ at low RH (< 5%) based on strong interlayer hydrogen bonds, whose shaped beads show strong mechanical stability and good water adsorption performance, for potential application in round-the-clock water harvesting in extremely arid regions [51]. A composite of hygroscopic salt in MOFs is a viable way to improve water uptake at low RH. Cost-effective composite sorbent of CaCl₂@MOF-808-11.8

exhibits excellent water uptake of 0.56 g g⁻¹ under low RH (RH = 30% at 25 °C), and its outdoor water harvesting device demonstrates a daily collection of 1.8 kg water per kilogram of material using only a solar-driven power supply system [52]. Composite sorbent of LiCl@MIL-101(Cr) shows 0.77 g g⁻¹ water sorption capacity at 1.2 kPa vapor pressure (RH = 30% at 30 °C), whose prototype enables the harvesting of 0.45-0.7 kg water per kilogram of material under laboratory and outdoor ambient conditions powered by natural sunlight without optical concentration and additional energy input [53]. By virtue of the fast adsorption kinetics of Ni₂Cl₂(BTDD), a rotating operational device with three adsorbent modules generating 2.11 L_{wate} kg_{MOF}⁻¹ d⁻¹ by 12 continuous harvest processes, using electric heating or lowgrade energy (e.g., waste heat) with natural cooling to achieve continuous operation [54].

At present, manipulating the interior surface of MOFs with atomic precision and understanding the evolution of water structure within the confinement space are undergoing tasks in seeking the next ideal materials [42,55–60].

2.4 Acetylene storage

Acetylene is a commonly used industrial gas. What is significantly different from other hydrocarbons is that acetylene becomes more active and polymerization under high pressure, with a higher risk of explosion [61]. Therefore, it is of great significance to develop a solvent-free high purity acetylene storage technology. As a long-range ordered porous crystalline material, MOF can enhance the host-guest interaction between framework and acetylene by the mod-

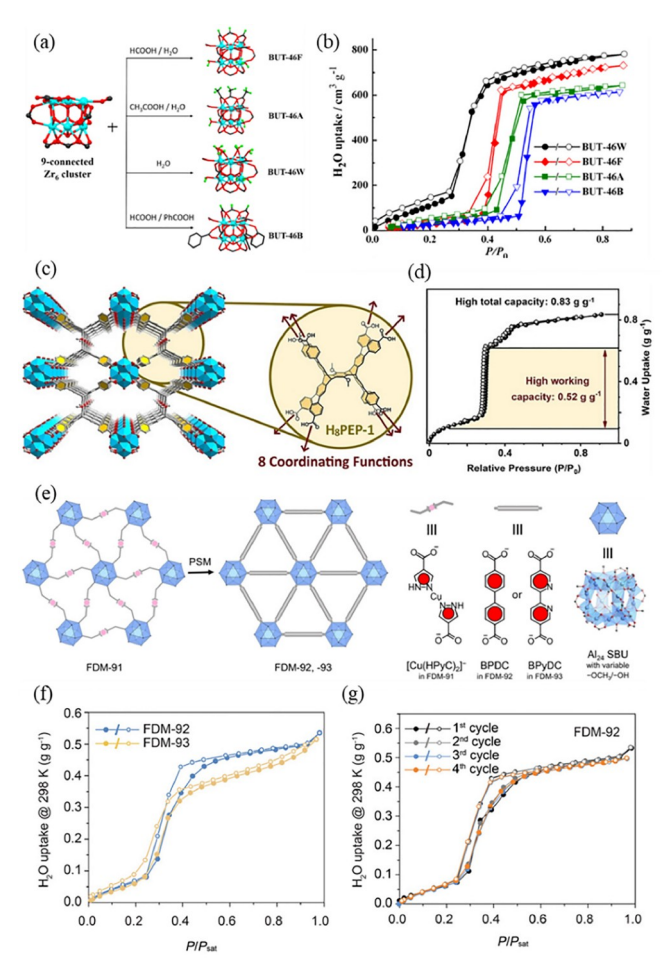


Figure 2 (Color online) (a) Zr₆ clusters in four BUT-46 MOFs with different terminal functional groups. (b) Water vapor adsorption/desorption isotherms of four BUT-46 MOFs at 298 K. Reproduced with permission from Ref. [48]. Copyright@2018, American Chemical Society. (c) Crystal structure of ZrMOF-1 viewed along *a* axis. (d) Working capacity of water harvesting of ZrMOF-1. Reproduced with permission from Ref. [49]. Copyright@2023, Wiley-VCH GmbH. (e) Single crystals of FDM-92 and FDM-93 are prepared by selectively substituting the FDM-91 in a post-synthetic manner. (f) Water adsorption isotherms of FDM-92 and FDM-93 at 298 K. (g) Four consecutive water adsorption measurements on FDM-92 at 298 K. Reproduced with permission from Ref. [50]. Copyright@2022, Wiley-VCH GmbH.

ification of metals and ligands, thereby achieving high acetylene adsorption capacity at room temperature and normal pressure [62].

A Cu-MOF, ZJU-5a exhibits extremely high C_2H_2 uptake capacity of 193 cm³ g⁻¹ at 298 K and 1 bar, attributed to the OMSs present in the framework and additional supramolecular interactions [57]. With a higher OMS density, FJI-H8 shows a record-high gravimetric acetylene uptake of 224 cm³ g⁻¹ and the second-highest volumetric uptake of 196 cm³ cm⁻³ at 295 K and 1 bar [58]. With Lewis basic nitrogen sites, ZJU-40a possesses an acetylene adsorption capacity of up to 216 cm³ g⁻¹ [59]. A series of ultra-microporous tetrazolate MOFs (SNNU-98-M, M = Mn, Co, Ni, Zn) exhibit high volumetric C_2H_2 uptake capacity as high as

222.9 cm³ cm⁻³ at 1 bar and 298 K [60].

Although high-purity acetylene storage at room temperature and near-normal pressure has attracted great interest in China, the practical application in industrial is yet to be explored.

3 Separation

Chemical separation accounts for 10%–15% of global energy consumption, with the major contribution coming from distillation [63]. Adsorptive separation and membrane separation can reduce energy consumption by approximately 70% and 90%, respectively [64,65]. While adsorptive separation and membrane separation share many fundamental principles, they also exhibit significant differences in the separation process, device design, and efficiency. Although membrane separation offers lower energy consumption, the fabrication of membranes is very challenging, especially using crystalline/particulate materials. Currently, most membrane separation applications are based on non-porous polymers [66,67].

Compared to membrane separation, adsorptive separation has the advantage of being easier to separate trace components [68]. Moreover, various conventional porous materials such as activated carbons and zeolites have been widely used in practical applications. The rich structural diversity, facile crystallization ability, and remarkable flexibility of MOFs have attracted intense attention for chemical separation in various aspects such as small molecule adsorptive separation, chiral separation, isotope separation, pollutant capture, and membrane separation.

3.1 Adsorptive separation of small molecules

Among a wide variety of chemical separation systems, the majority are small molecules [69,70]. In addition to traditional methods such as distillation and extraction, adsorption is currently the most widely applied technique for the separation of small molecules [71–75]. By interacting with a porous host material, the difference between guest molecules can be enlarged or even reversed [76]. Just like other physicochemical processes, adsorption/separation mechanisms can be divided into thermodynamics and/or kinetics. Molecular sieving is an ideal case of kinetic separation which completely excludes the oversized guests.

As the most important parameters for adsorptive separation, adsorption amount/capacity (strictly speaking, working capacity) and adsorption selectivity have a trade-off relationship [77]. For mixtures with almost the same properties, such as enantiomers and isotopes, selectivity is the primary focus (see Sections 3.2 and 3.3). In contrast, for mixtures with substantially large differences, such as cap-

Table 2 Water harvesting capacity and acetylene storage capacity of selected MOFs

MOFs	$C_{\rm grav}~({\rm cm}^3~{\rm g}^{-1})$	P	T(K)	Ref.
		Water harvesting capacity		
BUT-46F	605	$0.43^{b)} (P/P_0)$	298	[48]
BUT-46A	575	$0.49^{b)} (P/P_0)$	298	[48]
BUT-46W	630	$0.37^{b)} (P/P_0)$	298	[48]
BUT-46B	560	$0.55^{b)} (P/P_0)$	298	[48]
BIT-66	653	$0.60^{b)} (P/P_0)$	298	[47]
ZrMOF-1	772	$0.32^{b)} (P/P_0)$	298	[49]
FDM-92	532	$0.47^{b)} (P/P_0)$	298	[50]
FDM-93	436	$0.40^{b)} (P/P_0)$	298	[50]
MWH-1a	250 ^{a)}	$0.03^{b)} (P/P_0)$	293	[51]
		Acetylene storage capacity		
ZJU-5a	193	1 (bar)	298	[57]
FJI-Н8	224	1 (bar)	295	[58]
ZJU-40a	216	1 (bar)	298	[59]
SNNU-98-Mn	175 ^{a)}	0.1 (bar)	298	[60]

a) cm 3 cm $^{-3}$, b) $P_{\rm end}$ of the steep stage of adsorption curve.

turing CO₂ and pollutants from the air, researches mainly focus on capacity because the selectivity is intrinsically high (see Section 3.4). H₂O adsorption applications, such as drying, water harvesting from air, adsorption refrigeration, and humidity control, are H₂O/air separation processes but can also be regarded as H₂O storage processes because the air adsorption is negligible (see Section 2.3). For most mixtures, neither selectivity nor capacity can be neglected. Nevertheless, fundamental researches pay more attention to improving the selectivity of challenging mixtures such as those with similar boiling points [78].

Just like adsorptive storage, adsorptive separation also requires a cyclic process involving both adsorption and desorption. In addition to pressure swing adsorption (PSA), a simple and energy-efficient method commonly used for storage, separation processes often involve vacuum swing adsorption (VSA, a subset of PSA), temperature swing adsorption (TSA), or pressure and temperature swing adsorption (PTSA). Besides, the guest pressure/concentration can also be conveniently decreased by purging with inert gas, which is similar to the VSA process. In other words, the principles of adsorptive separation and storage are the same in terms of working capacity. Therefore, abnormal isotherm shapes (arise from guest-induced structural transformations and/or strong guest-guest interactions) are advantageous in increasing working capacity or reducing energy consumption [79,80]. The energy consumed/released by structural transformations can also decrease heat transfer demands, being conducive to large-scale applications [81]. Nevertheless, in terms of adsorption selectivity, there are substantial differences between rigid and flexible systems.

Structural transformations are always involved in adsorption/separation processes. But in many cases, they are so small and play negligible roles. In such instances, the structure-property relationships can be simply explained by host-guest interactions and guest-guest interactions from the thermodynamic point of view, and the former plays the predominant role [82]. For specific separation targets/guests, host-guest interaction is controlled by the structure of the pore-surface adsorption site, and MOFs can be facilely functionalized by various types of adsorption sites [83].

In principle, OMSs can coordinate with specific types of functional groups, leading to strong adsorption and high selectivity [84]. For example, hard Lewis acid Mg(II) prefers to bind hard Lewis bases such as CO₂, H₂O, and NH₃ [85]. Conversely, soft Lewis acid Cu(I) prefers to bind soft Lewis bases such as CO and unsaturated hydrocarbons [86]. There are also some more chemically specific coordination interactions, such as the selective charge transfer between Fe(II) and O₂ [87]. Note that hard Lewis acids usually exhibit high charge density, giving strong dipole-dipole interactions similar to hydrogen bonding.

Aliphatic amines and CO₂ can form reversible covalent bonds (carbamate), which is the primary strategy for CO₂ separation [88]. Similarly, monodentate hydroxide can reversibly react with CO₂ (bicarbonate), resembling the action of carbonic anhydrase [89]. While OMS, aliphatic amine, and monodentate hydroxide all show coordination abilities, they have very different synthesis difficulties. Typically, OMS can be conveniently obtained through the removal of

the terminal coordinating small molecules [84]. In contrast, aliphatic amine and monodentate hydroxide are generally introduced by coordinative PSM [90].

The π -conjugated amine groups are more commonly encountered nitrogen-containing functional groups, which can be facilely designed and constructed but their electron lone pairs exhibit low basicity/activity [91]. In contrast, for aromatic *N*-heterocycles, the electron lone pairs of the nitrogen atoms are not conjugated with the aromatic rings and they occupy fewer spaces (compared with amine groups) [92]. Although the high-activity aromatic nitrogen atoms can also coordinate with metal ions, they can be rationally introduced into MOFs through rational ligand design [93].

Each guest molecule may simultaneously interact with multiple adsorption sites to achieve strong host-guest binding [90]. Based on ultramicropores and proper arrangements of weak adsorption sites, MOFs have achieved extraordinary adsorptive separation performances, such as high C₂H₆/C₂H₄ [94,95], CO₂/N₂ [91,96,97], CO₂/C₂H₂ [98–101], C₃H₆/C₃H₈ [102], and CH₄/N₂ selectivities [103]. Pore size/shape engineering is fundamental for porous materials [104]. For small pores, multiple adsorption sites (may be weak) are put at suitable positions to bind the target guest simultaneously. For large pores, multiple target guest molecules are put at suitable positions to promote strong guest-guest interactions.

According to the thermodynamic principle, crystal-tocrystal structural transformation of a porous host occurs above a certain threshold guest-dependent pressure/concentration (Figure 3a, b) [105–108]. Therefore, around the threshold pressures of different guests, flexible adsorbents can show much larger isotherm differences than rigid adsorbents. For example, between the pore-opening pressures of two types of guests, the single-component isotherms are similar to those of molecular sieves [106]. However, periodic (crystal-to-crystal) pore-opening actions will theoretically show co-adsorption of small non-target guests under mixture conditions, and the inability of adsorption below the poreopening pressure will give rise to the leakage problem (Figure 3c). Note that in reality, structural transformations may involve more or less aperiodicity. Theoretically, a completely aperiodic structural transformation can avoid the aforementioned issues because each pore is independently opened by one target guest (Figure 3b, d) [109].

In conventional theories, size comparison between the pore aperture and the guest molecule is the key to explaining kinetic separation (including molecular sieving) [110]. In other words, both aperture and guest are treated as rigid entities. However, many MOFs with apertures significantly smaller than the guest molecules can still quickly adsorb guests or exhibit kinetic and even molecular sieving separation [111–113]. In fact, pore/aperture sizes of porous materials (including MOFs) and molecular sizes of guests (including kinetic diameters) are arbitrarily defined based on

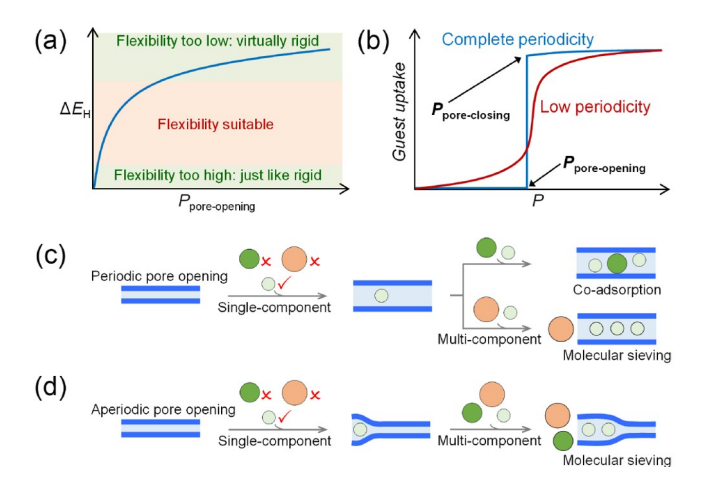


Figure 3 (Color online) Controlling adsorption/separation behavior of pore-opening adsorbents. (a) Relationship between host flexibility and pore-opening pressure. (b) Relationship between isotherm shape and periodicity of pore-opening behavior. Reproduced with permission from Ref. [105]. Copyright@2023, Springer Nature. (c) Adsorption/separation behaviors of ideally periodic pore-opening behavior. (d) Adsorption/separation behaviors of ideally aperiodic pore-opening behavior. Reproduced with permission from Ref. [106]. Copyright@2022, American Chemical Society.

equilibrium structures, which are just suitable for studying thermodynamic properties. For kinetic processes, transient structural changes of the host and guest are critical when the guest molecules are larger than the apertures (in the equilibrium state). In the concept of gating adsorption, diffusion/ gating barrier not only depends on the equilibrium-state sizes and host-guest interactions but also takes into account the energy barrier arising from the transient structural changes, as well as temperature (kT vs. E_a) (Figure 4a) [106]. Ultramicroporous MOFs usually exhibit negligible adsorption at 77 K and obvious adsorption at 195 K and higher temperatures, which can be attributed to the gating mechanism [106,114]. Because changing temperature can simultaneously increase or decrease the diffusion rates of all guests, achieving high kinetic selectivity or molecular sieving effect requires not only a large difference in gating barriers but also suitable temperature (Figure 4b). So far, most examples of molecular sieving have been observed at low temperatures rather than room temperature [115,116]. In addition to various structural types of pore apertures, gating adsorption can also occur at crystal surface defects, which have been demonstrated by some MOFs with pore apertures obviously larger than the guest molecules (Figure 5) [117].

Besides the host, guest molecules also exhibit flexibility, and guest molecules can show flexibility not only during the transient gating process but also in the equilibrium state [118]. Unlike crystalline hosts, thermodynamic structural transformations of guest molecules should occur independently, so that they can be hardly judged from isotherm shapes. Similar to the host, the structural transformation of guest molecules increases the system energy, which can be

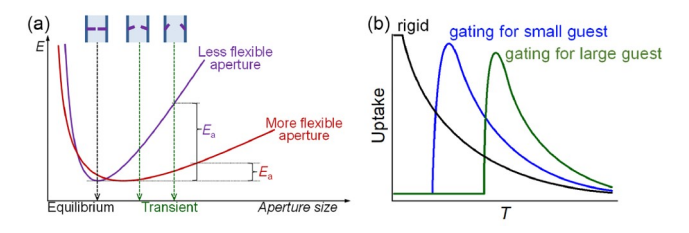


Figure 4 (Color online) Principle of gating adsorption for separation. (a) The dependence of host gating barrier and guest size. Reproduced with permission from Ref. [111]. Copyright@2021, Elsevier. (b) Characteristic adsorption isobars of conventional adsorbents and gating adsorbents for guests with different sizes. Reproduced with permission from Ref. [114]. Copyright@2008, American Chemical Society.

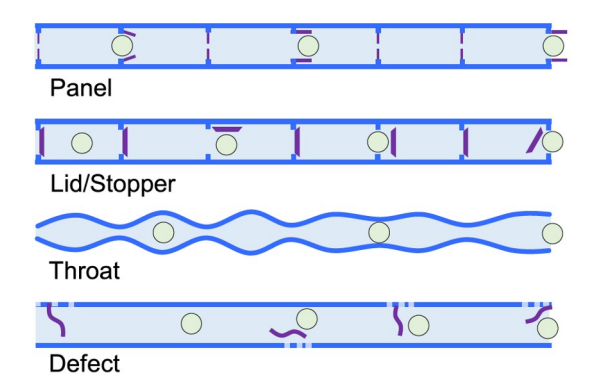


Figure 5 (Color online) Typical types of gating pores (note that each gate opens/closes independently). Reproduced with permission from Ref. [106]. Copyright@2022, American Chemical Society.

utilized to weaken adsorption. To facilitate the adsorption of guest molecules in a thermodynamically unfavorable configuration, all pores must possess highly suitable sizes and shapes. When the unstable guest configuration has a larger cross-sectional size (compared with the stable configuration), gating channels are required to allow guest molecules to diffuse (Figure 6) [118].

Unlike adsorptive storage, adsorptive separation works under multi-component conditions. Under mixed-component conditions, particularly for gases, quantitative measurements of adsorption amount under multi-component conditions are much more difficult than for single-component conditions. Therefore, single-component adsorption data have been widely used to predict the adsorption/separation behavior under mixture conditions. However, available calculation/ prediction methods have rather limited applicability. For instance, the Ideal Adsorbed Solution Theory (IAST), assumes that the adsorbent is homogeneous, the surface provides equal access for all guests, and the adsorbed phase is an ideal solution, is inapplicable to adsorbents with variable and/or heterogeneous structures (including flexible adsorbents and molecular sieves) and adsorbates with significantly different adsorbing abilities [119]. Considering that many MOFs have demonstrated interesting and pro-

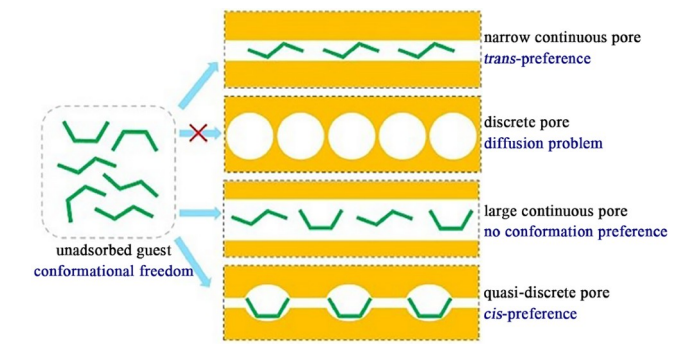


Figure 6 (Color online) Principle of controlling guest conformations to lower adsorption enthalpy by using gating pores. Reproduced with permission from Ref. [118]. Copyright@2017, AAAS.

mising separation behaviors, quantitative/accurate measurements of mixture adsorption/separation performances are emerging as a fundamental research protocol, which is not only necessary for studying adsorptive separation mechanisms especially those involving molecular sieving, co-adsorption, and leakage, but also useful for fair comparison with reliable benchmarks.

3.2 Small molecule separation through membranes

As a highly favored green renewable energy source, H₂ is mainly produced through coal gasification and steam reforming of hydrocarbon fuels followed by gas shift reaction, with CO₂ being the main by-product that needs to be separated. The good hydrothermal stability of membranes is a prerequisite for their application in the purification of H₂ since the accompanying high temperature and water vapor. Efficient H₂/CO₂ separation is mainly realized based on the difference in molecular sizes of H₂ and CO₂. Therefore, most of the high-performance H₂/CO₂ separation membranes also have high selectivity for H₂/N₂ and H₂/CH₄ separations corresponding to the recovery of H₂ from the off-gases of synthetic ammonia and the enrichment of H2 from natural gas. Among the reported works, we would like to discuss in particular the application of molecular sieving 2D MOF nanosheets in building high-performance ultrathin membranes. Yang and co-workers [120] developed an ultrathin MOF film through thermal-assisted deposition of disorderly stacked Zn₂(bim)₄ nanosheets on the surface of the α-Al₂O₃ disk. The membrane exhibits excellent H₂ permeance (up to several thousand GPU) and H₂/CO₂ selectivity (over 200) due to the molecular sieving effect of Zn₂(bim)₄ towards H₂ and CO₂ (Figure 7a). This progress inspires a lot of extended work on utilizing MOF nanosheets as building blocks of ultrathin membranes [121-123]. As to MOF-based mixedmatrix membranes (MMMs), the polyimide-based membrane containing penetrating ZIF-7 sheets developed by Huang and co-workers [124] provides a good example of the

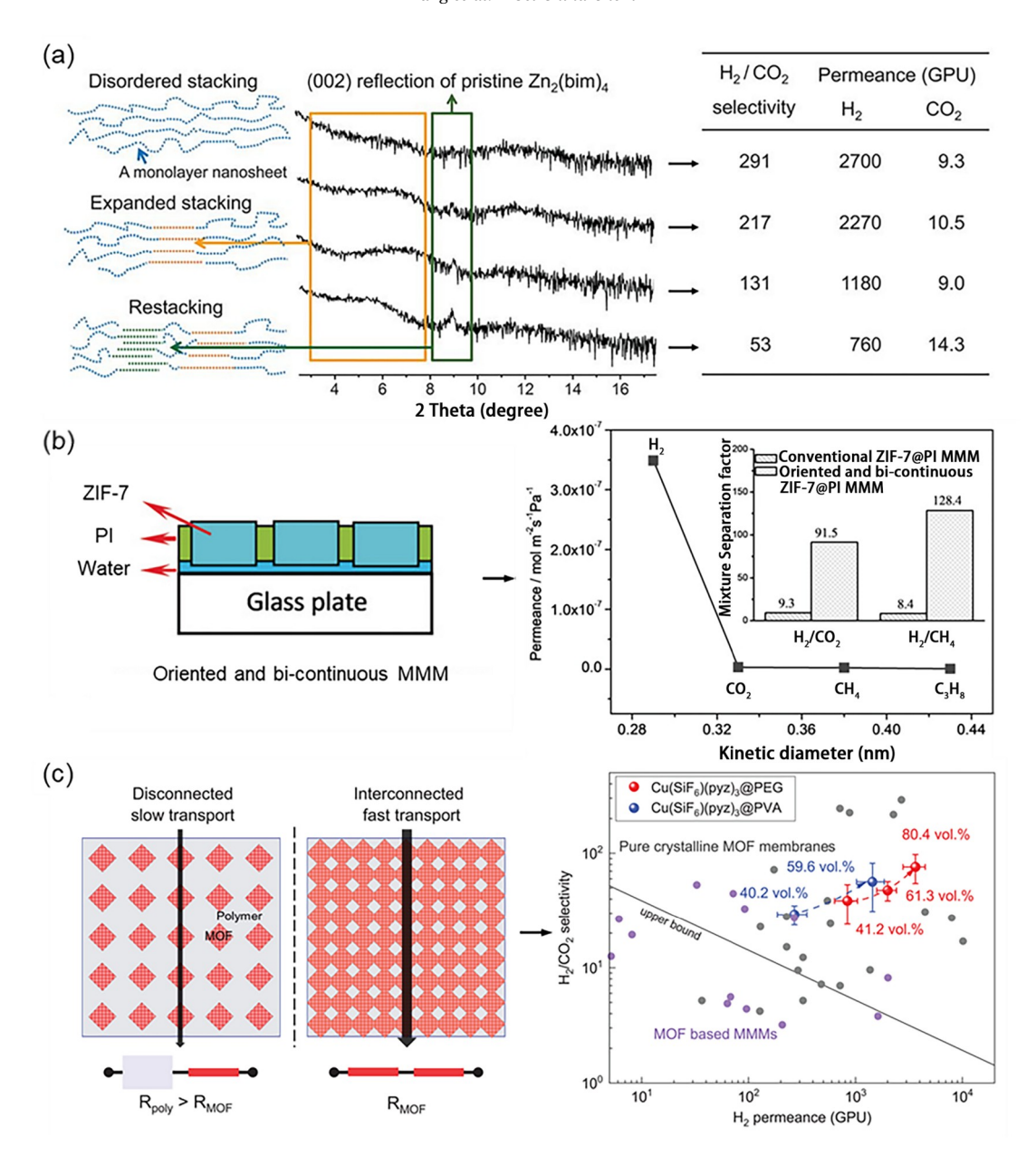


Figure 7 (Color online) (a) H₂/CO₂ separation performance of the disorderedly stacked Zn₂(bim)₄ nanosheet membrane. Reproduced with permission from Ref. [120]. Copyright@2014, AAAS. (b) H₂/CO₂ separation performance of the ZIF-7 sheet penetrating MMM. Reproduced with permission from Ref. [124]. Copyright@2019, Wiley-VCH GmbH. (c) H₂/CO₂ separation performance of the Cu(SiF₆)(pyz)₃ nanofiller interconnected MMM. Reproduced with permission from Ref. [125]. Copyright@2023, AAAS.

full utilization of the separation ability of the MOF fillers (Figure 7b). Very recently, Jin and co-workers [125] reported the fabrication of $\text{Cu}(\text{SiF}_6)(\text{pyz})_3$ -based MMMs using the solid-solvent strategy. The novel MMMs have both high filler loading without agglomeration and penetrating screening channels, as well as good potential in large-scale preparation, showing great prospects in practical H_2/CO_2 separation (Figure 7c).

The exploration of natural gas as a clean energy source needs the purification of CH_4 , and CO_2 is the major impurity. The emission of CO_2 into the atmosphere is a major cause of

global warming and climate change, making the post-combustion capture of CO_2 from flue gases increasingly important. Therefore, the development of high-performance CO_2/CH_4 and CO_2/N_2 separation membranes is also an important research direction in the membrane field. The physical properties of CO_2 are quite different from those of CH_4 and N_2 , leading to their distinct adsorption and dissolution behavior in porous MOFs and polymers. Therefore, the design of CO_2/CH_4 and CO_2/N_2 separation membranes mainly relies on the differentiation interaction resulting in dissolution and diffusion difference. For example, various CO_2 -

philic functional groups (–NH₂, –F, etc.) have been introduced into the structure of MOFs to improve the CO₂ dissolution and diffusion coefficients and selectivity in membranes (Figure 8a) [126]. As to the size screening of CO₂/CH₄ and CO₂/N₂, the mixed-linker ZIF-7_x-8 pure membrane with stiffened structure induced by *in situ* electric field during current-driven synthesis developed by Wang and co-workers (Figure 8b) [127], and the MMMs based on ZIF-8 with pore aperture adjusted by ionic liquid encapsulation [128] and molecular inducer (CF₃COO⁻) electrostatic-anchoring [129] can provide useful guidance in membrane designment.

Considering the rich reserves, shale gas containing lower CH_4 concentration than regular natural gas can be a great supplement to fossil energy. The key point is the removal of accompanying impurities, mainly the high-content N_2 , making the CH_4/N_2 separation increasingly important. In this aspect, strengthening the interactions with CH_4 having larger polarizability than N_2 is a possible way to improve the se-

paration efficient, considering the very close kinetic molecular size, polarity, and boiling point. For example, Zhong and co-workers [130] created a self-supported ZIF-62 glass foam membrane with developed pore channels and abundant OMSs through a polymer-thermal-decomposition-assisted melting strategy. The membrane exhibits exciting CH₄ permeance (30,000–50,000 GPU) and top-notch CH₄/N₂ selectivity (4–6) (Figure 9a). They also developed a series of well-performing MOF-based MMMs through tuning the OMSs of the MOF fillers [131–133]. For the accurate screening of CH₄ and N₂, Eddaoudi and co-workers [134] made a great demonstration by inducing shape irregularity to the pore window through the participation of an asymmetric linker.

Light olefins (C_2H_4 and C_3H_6) are importance raw materials in the chemical industry, while the generation of corresponding paraffins (C_2H_6 and C_3H_8) is inevitable during their production through hydrocarbon cracking and catalytic dehydrogenation. The similar low boiling point and mole-

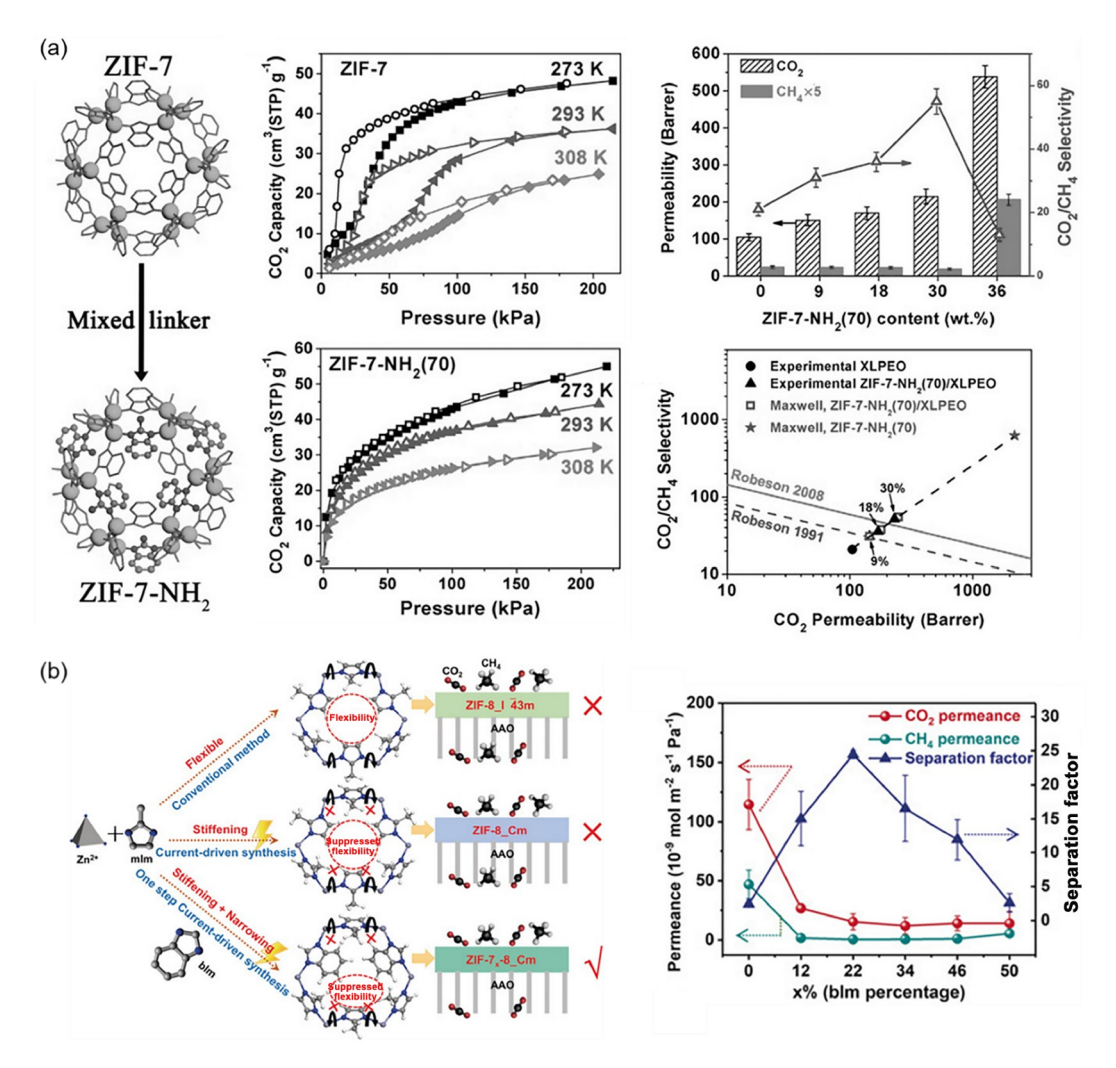


Figure 8 (Color online) (a) Representative examples for tuning CO₂ separation performance through interaction enhancement. Reproduced with permission from Ref. [126]. Copyright@2017, Wiley-VCH GmbH. (b) Representative examples for tuning CO₂ separation performance through pore size regulation. Reproduced with permission from Ref. [127]. Copyright@2019, Wiley-VCH GmbH.

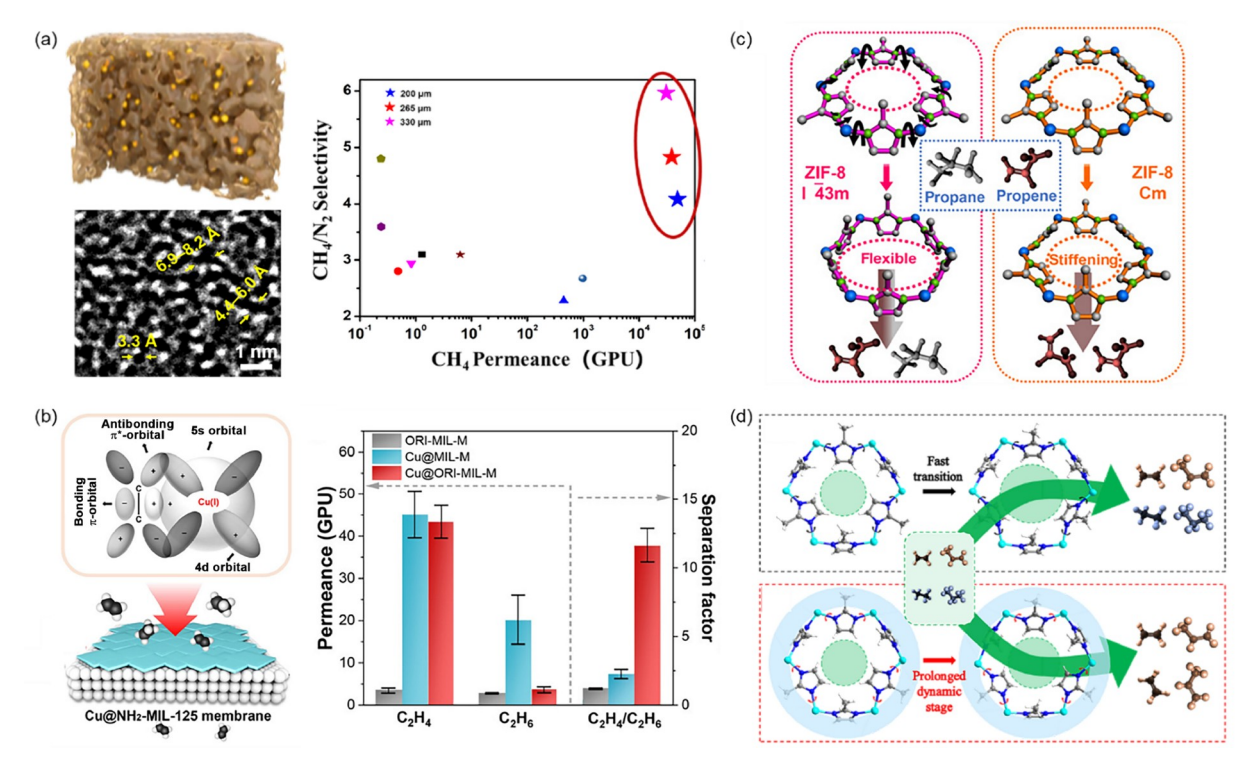


Figure 9 (Color online) Representative examples for light hydrocarbon separations. (a) The ZIF-62 glass foam membrane for CH_4/N_2 separation. Reproduced with permission from Ref. [130]. Copyright@2023, Springer Nature. (b) The $Cu(I)@NH_2$ -MIL-125 membrane for C_2H_4/C_2H_6 separation. Reproduced with permission from Ref. [136]. Copyright@2023, Wiley-VCH GmbH. (c) The paralyzed ZIF-8 membrane for C_3H_6/C_3H_8 separation. Reproduced with permission from Ref. [137]. Copyright@2018, AAAS. (d) The ZIF-8@XLPEO MMMs with the non-equilibrium stage for C_2H_4/C_2H_6 and C_3H_6/C_3H_8 separation. Reproduced with permission from Ref. [138]. Copyright@2021, Royal Society of Chemistry.

cular size make the separation of C₂H₄/C₂H₆ and C₃H₆/C₃H₈ difficult and energy-consuming. For C₂H₄/C₂H₆ separation, Liu and co-workers [135] developed a Co-gallate MOF membrane through a new freezing contra-diffusion protocol. The frozen CoCl₂ solution in the inner tube allows better control of the release and diffusion rate of Co²⁺ to the substrate-solution interface to react with the ligand, thus offering a well-intergrown membrane without cracks and pinholes. The membrane shows a good C_2H_4 permeance (72.6 GPU) and a high C_2H_4/C_2H_6 selectivity (8.3). They also prepared a Cu(I) complexed c-oriented NH₂-MIL-125 membrane (Figure 9b) [136]. The favorable π -complexation between the Cu(I) and C₂H₄ molecules leads to a high C₂H₄/C₂H₆ selectivity of 13.6. As to C_3H_6/C_3H_8 separation, ZIF-8 is the most studied MOF for membrane preparation. The 2-methylimidazole in ZIF-8 can rotate upon the approaching of C_3H_6 and C_3H_8 molecules, opening up the pore window to a value between the kinetic size of C₃H₆ and C₃H₈ molecules, thus showing a sharp molecular sieving effect. Among the reported works, we would like to introduce the membrane developed by Wang and co-workers [137] in particular. The current-driven synthesized ZIF-8 membrane has an inborn distorted polymorph of ZIF-8_Cm with suppressed linker mobility, thus showing a more sharpened molecular sieving effect for C₃H₆/C₃H₈ separation (with the best separation factor above 300) (Figure 9c). Finally, we would like to introduce a novel MMMs developed by Zhong and co-workers [138]. They found that the flexibility of the ZIF-8 framework can be gradually released with the increasing in the mobility of molecular chains chelated to the framework, caused by the progressive plasticization of the XLPEO polymer matrix (XLPEO = cross-linked poly(ethylene oxide)) upon the gradual dissolution of C₃H₆ and C₃H₈ molecules (Figure 9d). This leads to the continuous expansion of the aperture of ZIF-8, thus the appearance of an unprecedented non-equilibrium stage with high C₃H₆/C₃H₈ and C₂H₄/C₂H₆ separation factors (over 200 and 20) that far exceed those of the existing MMMs. This work not only provides a new opportunity for realizing efficient C₃H₆/C₃H₈ separation by exploiting the non-equilibrium stage, but also opens a new door for designing high-performance MMMs.

Pervaporation has been well recognized as a promising technology for liquid separations, for example, organic solvent dehydration, organic mixture separation, and reversible reaction facilitation, in chemical and pharmaceutical industries. During the pervaporation separation, the membrane surface on the feed side contact with vaporizable solvent mixtures, while the permeate side is vacuumed or swept to generate the driving force. The separation of components relies on the difference in their adsorption and diffusion in

the membrane. Both pure MOF membranes and MOF-based MMMs have been explored in pervaporation separations. For example, Jin and co-workers [139] developed a continuous ZIF-71 membrane on ceramic hollow fiber, which shows excellent ethanol recovery performance. Li and co-workers [140] prepared a CAU-10-H membrane for ethanol dehydration. The membrane shows a total flux of 493 g m⁻² h⁻¹ and a separation factor of 148 for the 90 wt% ethanol agueous solution. Yang and co-workers [141] developed a robust hetero-lattice intergrown MOF membrane from the complementary growth of MIL-53(Al) and NH₂-MIL-101(Cr). The membrane has an ultrahigh separation factor (13,000) for the 90/10 ethanediol/water solution, which can largely reduce the energy consumption for their separation (Figure 10a). As to the MOF-based MMMs, Yang and co-workers [142] incorporated ZIF-8 nanoparticles in the PMPS (polymethylphenylsiloxane) matrix and obtained a membrane with high selectivity (40.1) and productivity (6.4 kg m^{$^{-2}$} h^{$^{-1}$}) for the recovery of 1.0 wt% isobutanol from water, showing good potential in facilitating the production of butanol through biological fermentation. Zhong and co-workers [143] prepared interfacial compatibility optimized MMMs based on PDA-modified MIL-101(Cr)-SO₃H for water/ ethylene glycol separation. The membrane has a greatly enhanced water permeability and separation factor compared with the pure poly(vinyl alcohol) membrane. In particular, Zhao and co-workers [144] prepared a ZIF-8 nanosheet/PDMS membrane through pre-embedded seed-induced confined growth of honeycomb-arranged ZIF-8 nanosheets followed by PDMS titration coating. This kind of novel membrane has continuous transport channels across the membrane and selective adsorption towards ethanol molecules, thus showing great potential in the practical application of alcohol/water separations (Figure 10b).

Traditional nanofiltration membranes are mainly based on polyamide interfacial polymerized from amine and acyl chloride monomers. The lack of ordered pore channels in the separation layer affects the permeance of membranes greatly. Introducing porous nanofillers, such as MOFs can be a good solution to this problem. For example, Zhong and co-workers [145] applied long alkyl chain modified UiO-66-NH₂ nanoparticles as filler in polyamide-based thin film nanocomposite (TFN) membrane to eliminate the generation of aggregation of MOF particles and interfacial micro voids (Figure 11a). The MOF-based TFN membrane shows largely improved methanol permeance without sacrificing the high rejection rate to tetracycline. Wang and co-workers [146] tuned the pore of MOF fillers to be the primary permeation channels in MIL-101(Cr) based TFN membrane by adjusting the density of the polyamide structure. The membrane exhibits significantly improved performance in the removal of endocrine-disrupting compounds from water. Jin and co-

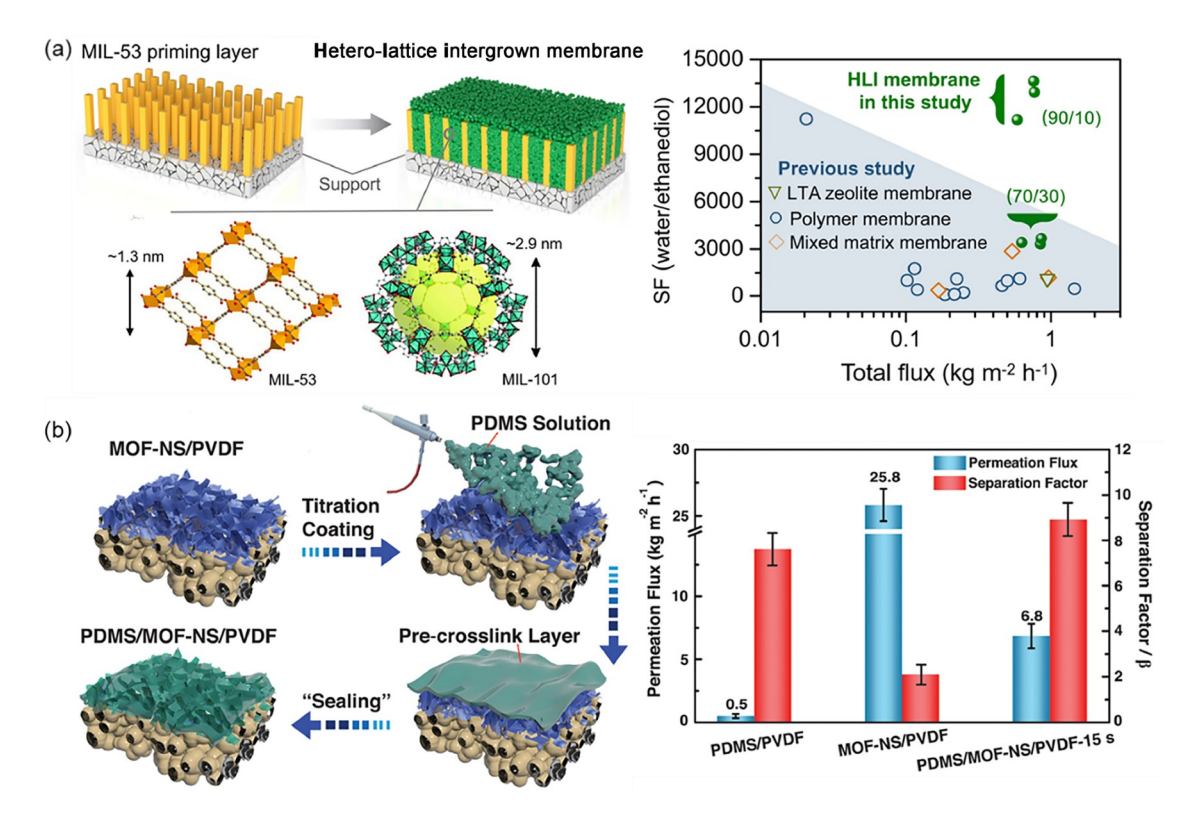


Figure 10 (Color online) Representative MOF-based pervaporation membranes. (a) MIL-53@MIL-101 hetero-lattice intergrown membrane for water/ethanediol separation. Reproduced with permission from Ref. [141]. Copyright@2022, Wiley-VCH GmbH. (b) ZIF-8 nanosheet@PDMS membrane for ethanol/water separation. Reproduced with permission from Ref. [144]. Copyright@2022, AAAS.

workers [147] reported a novel strategy for the preparation of polyamide membranes with crumpled structures. This strategy involves the deposition of ZIF-8 nanoparticles on the substrate and the etching removal of ZIF-8 before and after interfacial polymerization. The membrane shows high water permeance because of the increase in the effective permeation area. Besides using polyamide as the polymer matrix, Li and co-workers [148] developed a ZIF-8/Poly(sodium 4styrene-sulfonate) nanofiltration membrane through a coordination-driven in situ self-assembly strategy. The membrane has an excellent performance in the nanofiltration separation of methyl blue from water. They also developed a high-flux nanofiltration membrane with BUT-8(A) as the filler and PEI as the matrix [149]. Pure MOF membranes have also been explored in nanofiltration. For example, Liu and co-workers [150] successfully prepared a continuous MOF-303 membrane on the α -Al₂O₃ substrate. The membrane has high rejection rates to divalent ions (e.g., 93.5% for MgCl₂ and 96.0% for Na₂SO₄) because of the synergistic effect of size-sieving and electrostatic repulsion (Figure 11b). Lin and co-workers [151] prepared a ZIF-8/(TA-Zn²⁺)₂ nanofiltration membrane on poly(ether sulfone) (PES) substrate using the TA-Zn²⁺ based network as the precursor. The membrane has a pure water permeance reached 5.1 L m⁻² h⁻¹ bar⁻¹, and the NaCl and Na₂SO₄ rejections of 55.2% and 93.6%, respectively. Wang and co-workers [152] assembled 2D Cu-TCPP nanosheets into nanofiltration membranes. The membranes were found to be highly water permeable while having high rejection rates to dyes.

Compared with membranes based on traditional materials, research on MOFs-based membranes is still in its infancy, while significant advantages have been demonstrated. Taking CO₂/N₂ and H₂/CO₂ separation systems as examples, the separation performance of different membrane materials was compared (Tables 3 and 4) [121,136,153–195]. The results

showed that MOFs-based membranes exhibited superior separation performance in terms of size sieving effect, thanks to the precise and controllable pore size of MOFs. At the same time, the modifiability of the MOF pore environment also demonstrated extraordinary application potential for MOF membranes in CO_2 -exclusive recognition.

3.3 Enantioseparation

Enantioseparation of racemates mediated by chiral porous materials represents a state-of-art technique to achieve enantiopure compounds [196]. The enantioselective process can be extremely difficult due to the very similar properties of enantiomers. Typically, to achieve efficient enantioseparation, there usually needs to be a minimum of three simultaneous interactions between the selector and analyte ("three-point rule"), with at least one of these interactions being stererochemically dependent. For a MOF to act as a chiral selector, it therefore should contain multiple chiral recognition sites that can work synergistically to induce selective recognition and binding of analytes and to exert enantiocontrol. In this section, we will showcase recent research progress in the field of employing chiral MOFs (CMOFs) as host materials to recognize and separate challenging racemates in an enantioselective manner.

Crystallization, along with adsorption, is one of the most important methods for the recovery of pure enantiomers. It is generally difficult to perform optical resolution of small chiral organic molecules such as secondary alkyl alcohols and amines, due to the subtle structural difference between the enantiomers as methyl groups and hydrogen atoms attached to the chiral carbon have to be discriminated. In this regard, chiral MOFs have shown great potential for applications as adsorbents in the optical resolution of racemic small molecules. In 2011, Chen and co-workers [197] de-

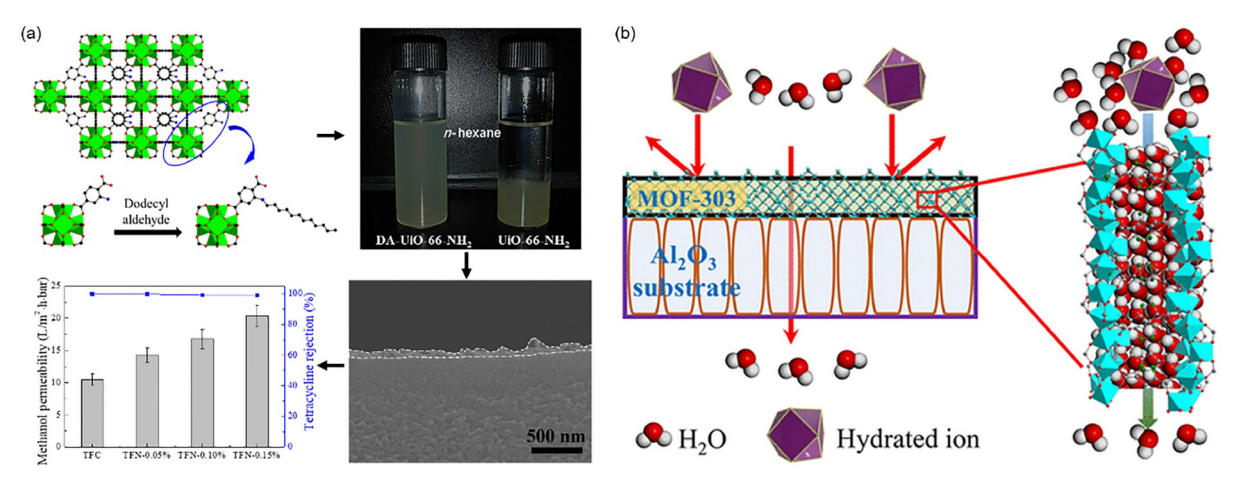


Figure 11 (Color online) Representative progress in the development of MOF-based MMMs and pure MOF membranes for nanofiltration separation. (a) The UiO-66-NH₂@PA TFN membrane for organic solvent nanofiltration. Reproduced with permission from Ref. [145]. Copyright@2016, Wiley-VCH GmbH. (b) The MOF-303 crystalline membrane for nanofiltration desalination. Reproduced with permission from Ref. [150]. Copyright@2021, American Chemical Society.

Table 3 Comparison of H₂/CO₂ separation performance of related membranes

Membrane type	Membranes	P(H ₂)/Barrer	$\alpha(H_2/CO_2)$	Operating conditions	Ref.
	$Zn_2(bim)_4$	3,789	62	125 °C, 1 bar	[153]
	N_{10} - $Zn_2(bim)_4$	2.8	1,158	20 °C, 1 bar	[121]
	ZIF-L	403.3	321	room temperature, 1 bar	[154]
MOF-based membrane	Ni-LAP-NH ₂	460	41.7	120 °C, 1 bar	[155]
	KAUST-7	6,600	17.7	25 °C, 1 bar	[156]
	ZJU-74a	16.32	100	25 °C, 1 bar	[157]
	ZrPP	482.7	101.2	200 °C, 1 bar	[158]
	NH ₂ -UiO-66	49.2	41.3	25 °C, 1 bar	[159]
	BIALP	2.26-5.22	121	150 °C, 1 bar	[160]
	BILP-5	362	16	room temperature, 1 bar	[161]
Polymer-based membrane	sPPSU-PBI-PEI	2.49	59.3	35 °C, 3.5 bar	[162]
	BILP	6.35	56.3	200 °C, 1 bar	[163]
	PMDA-MA PI	69.5	18.7	350 °C, 2 bar	[164]
	Lamellar stacked MXene membrane	>2,200	>160	25 °C, 1 bar	[165]
	ECNU-28 membrane	901.5	41	25 °C, 1 bar	[166]
	MXene hollow fiber membrane	1.41	30.3	25 °C, 1 bar	[167]
	Tubular 2D MXene membrane	297	55	25 °C, 1.01 bar	[168]
	Pd-MXene membrane	619.3	242	25 °C, –	[169]
Zeolite-based membrane	sMMM900	37	130	70 °C, 5.05 bar	[170]
	ZN_CMS_06	1,606	20.77	25 °C, 2 bar	[171]
	PBI-PPA/CMS	140	58	150 °C, 6.6 bar	[172]
	Nano-wrinkled reduced GO	1.46	529.9	120 °C, 1 bar	[173]
	Cellulose-based asymmetric carbon	444.6	83.9	130 °C, 15.2 bar	[174]
	Asymmetric CMS membrane	2,775	36.9	110 °C, 10 bar	[175]

veloped a mixed-MOF approach to construct chiral MOFs with tunable micropores for enantioselective recognition. The chiral salen-based MOF with narrow chiral channels was proved to be capable of selectively adsorbing one enantiomer of 1-phenylethyl alcohol from the racemic solution with 64% ee.

Later in 2013, Cui and co-workers [198] reported the construction of a chiral biphenol-based MOF for enantioselective separation. The porous 3D framework decorated with chiral dihydroxy groups was demonstrated to be crucial for achieving efficient enantioseparation as exemplified in the cases of methyl mandelate, ethyl mandelate, *i*-propyl mandelate, and benzyl mandelate, giving ee values in the range of 64.3%–93.1%. Interestingly, the control experiments using only organic ligands showed no selectivity toward those substrates, highlighting the unique role of framework confinement in facilitating specific host-guest interactions. Further, Cui *et al.* [199] prepared another chiral Mn-MOF based on the same chiral ligand (Figure 12). The resulting chiral MOF exhibited remarkable porosity with

BET surface area of 2,145 m² g⁻¹, which is beneficial for achieving fast substrate diffusion kinetics. Impressively, the MOF can separate racemic aromatic and aliphatic amines with very high enantioselectivity of up to 98.3%. To demonstrate the utility and practicability of the separation process, a large-scale resolution of 1-phenylethylamine was performed, yielding 116 mg of the product with 92.5% ee. Moreover, the adsorbent could be reused for at least the following three runs without any loss of enantioselectivity.

Chromatography is one of the most commonly used and efficient laboratory techniques for enantioseparation of racemates. Owing to the large surface area and rich and tunable recognition sites, chiral MOFs have recently been explored as chiral stationary phases (CSPs) for use in gas chromatography (GC) and high-performance liquid chromatography (HPLC), aiming to develop a new generation of chiral materials and techniques for enantioseparation [200]. In 2011, Yuan and co-workers [201] reported the first example of utilizing chiral MOF as stationary phases in GC. The MOF-coated fused-silica open tubular column was prepared by a

Table 4 Comparison of CO₂/N₂ separation performance of related membranes

Membrane type	Membranes	P(CO ₂)/Barrer	$\alpha(\text{CO}_2/\text{N}_2)$	Operating conditions	Ref.
	ZIF-8@CA	96	168.8	-, 4 bar	[176]
	ZIF-62	2,602	23	25 °C, 1 bar	[177]
	CAU-1	9,850	26.3	25 °C, 1 bar	[178]
MOF-based membrane	Cu@NH ₂ -MIL-125	626	43.2	room temperature, 1 bar	[136]
MOF-based membrane	UiO-66-CH ₃	283,500	2.20	31 °C, 1 bar	[179]
	ZIF-8	2100	10.8	25 °C, 2 bar	[180]
	UiO-66	394.8	31.3	room temperature, 1 bar	[181]
	PDA/UiO-66	892	51.6	25 °C, 1 bar	[182]
	PI-2-TFSI	90.1	21.9	35 °C, 1 bar	[183]
	6FDA-FDA-BisAHPF	654	43.2	30 °C, 0.5 bar	[184]
Polymer-based membrane	6FDA-FDBDA	412	23.8	25 °C, 1 bar	[185]
	PIM-1/Am-PAFEK	752	26.7	30 °C, 2 bar	[186]
	PVAc/c-PIL semi-IPN	59.6	36.1	30 °C, 1.2 bar	[187]
	F8TM-1	383	35	25 °C, 1 bar	[188]
	ZCMS-600-15	8,902	42.2	30 °C, 0.1 bar	[189]
	Fe ₃ O ₄ @ZIF-8	5,130	29	25 °C, 1 bar	[190]
	F8TM-1-500	2,140	36	25 °C, 0.3 bar	[188]
Zeolite-based membrane	SAPO-34	1,126	19.3	35 °C, 1 bar	[191]
	HSBI-3-CF3	453	44	−20 °C, 2 bar	[192]
	CMS-650-1	2,176	48.2	30 °C, 0.1 bar	[193]
	PIM-1/MXene	12,475.3	32.7	25 °C, 3 bar	[194]
	Co@NC@ZIF-8	27,050	10.4	25 °C, 1 bar	[195]

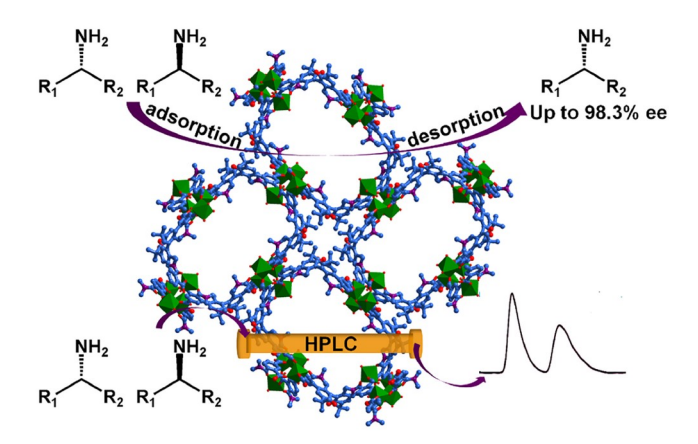


Figure 12 (Color online) Schematic illustration of the adsorption separation and HPLC separation of amines with chiral Mn-MOF. Reproduced with permission from Ref. [199]. Copyright@2014, Springer Nature.

dynamic coating method. The performance of the CSP was evaluated by a variety of racemates, including aldehyde (citronellal), ketone (camphor), amino acid (alanine, leucine, valine and isoleucine), alcohol (1-phenyl-1,2-ethandiol and 1-phenyl-ethanol), and organic acid (phenylsuccinic acid). All the enantiomer pairs could be baseline or at least 85% valley separated on the CSP except for camphor and 2-me-

thyl-1-butanol (Figure 13).

Compared with GC separation, HPLC separation with chiral MOFs as stationary phases has proven to be a more robust and general technique for enantiomers separation because of their broad analyte scope. In addition, HPLC uses a pressure pump instead of the heat-driven gas mobile phase in GC; as a result, the entire separation process can be per-

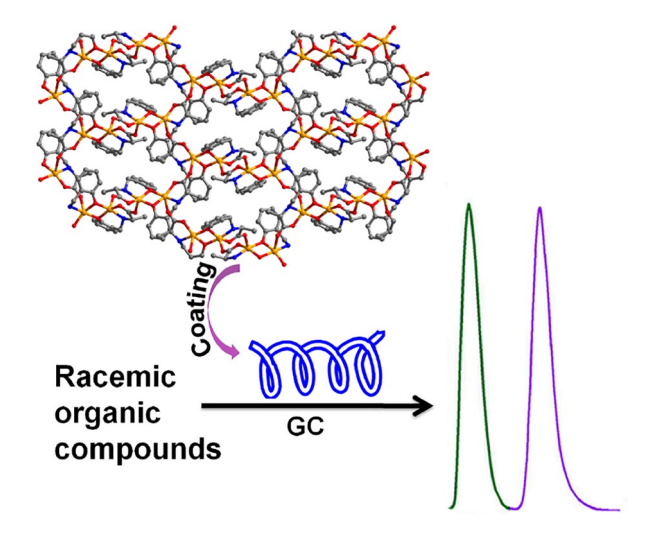


Figure 13 (Color online) Schematic illustration of the GC separation by the chiral MOF packed column. Reproduced with permission from Ref. [201]. Copyright@2011, American Chemical Society.

formed at any time and finished quickly, typically within tens of minutes. In this field, Cui *et al.* [202] reported the reticular synthesis of a serial of highly stable Zr-based chiral MOFs built from crown ether functionalized biphenol backbone. These robust chiral MOFs showed, for the first time, exceptionally great performance in the RP-HPLC separation for a broad of amino acids and *N*-containing drugs under acidic aqueous eluent conditions. Moreover, the chiral MOF stationary phase can be repeatedly used for over 4,000 injections within one year without significantly deteriorating the column efficiency.

In comparison with HPLC separation, membrane-based separation techniques stand out for their low cost, continuous operation and easy scale-up. To date, only limited MOFs are used as chiral membrane materials for enantioseparation because the structural integrity of the MOF membrane is easily compromised by mechanical stress [203]. In 2012, Jin and co-workers [204] reported the first example of chiral

MOF membranes by using ZnO support as a seeding source. The membrane surface is homogeneous and covered by truncated cubic grains, and the membrane is well bonded with the support with a thickness of about 25 μ m. The chiral separation potential of the as-synthesized membrane was evaluated by the resolution of R/S-methyl phenyl sulfoxide. A maximum of 33% ee was obtained for a feed concentration of 2% after 48 h (Figure 14).

Another effective route to fabricate chiral MOF membranes is to incorporate them into polymers homogeneously to obtain MMMs. Recently, Zhang and co-workers [205] reported the development of CMOF-based enantioselective membrane separation. PSM of amino-functionalized achiral MIL-53 with enantiopure *L*-histidine or *L*-glutamic acid generated two homochiral MOFs. The nanocrystals of the resultant chiral MOFs were integrated into PES matrix to form homochiral self-standing MMMs and exhibited excellent enantioselectivity for racemic 1-phenyl-ethanol with the highest ee value of 100% during the initial stage of permeation (Figure 15).

Enantioseparation using chiral MOF materials is still at the embryonic stage, although significant progress has been made in the separation of small alcohols, amines, phenyl sulfoxides, amino acids and so on, the resolution of racemic molecules is only evaluated of a relatively small number of components with similar properties. Besides improving the structure quality of these porous materials, a relevant future trend in MOF-based chiral recognition and separation will be the synthesis of chiral frameworks capable of furnishing wider separation ability.

3.4 Extraction of radioactive substances

The growing energy demand has driven the exploration of clean energy alternatives to fossil fuels. Nuclear power, known for its efficient and economical implementation, has been extensively developed and widely utilized in recent

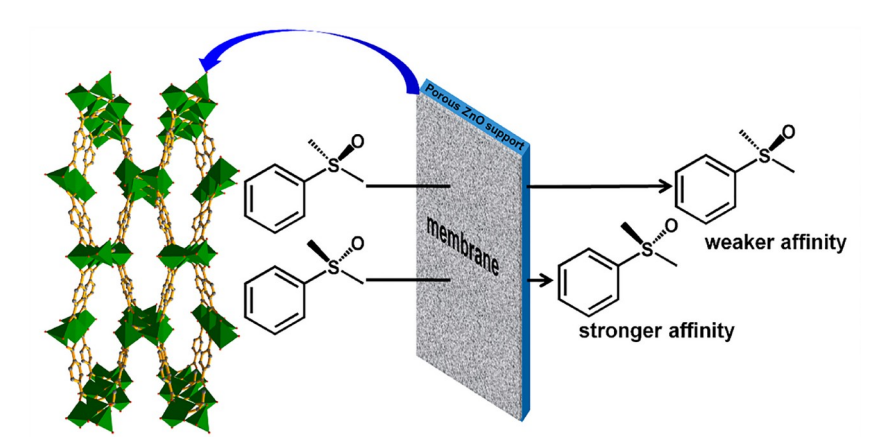


Figure 14 (Color online) Schematic representation of the chiral resolution of sulfoxides by CMOF-based membrane. Reproduced with permission from Ref. [204]. Copyright@2012, Royal Society of Chemistry.

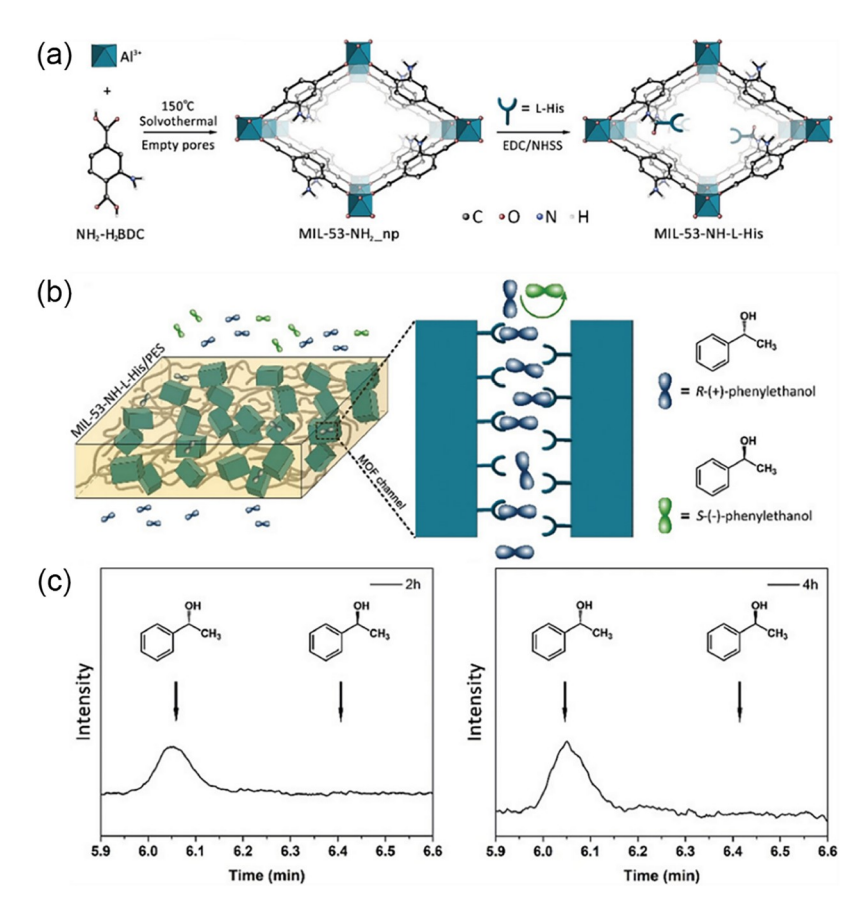


Figure 15 (Color online) (a) Synthesis procedure of MIL-53-NH-*L*-His. (b) Enantiorecognition behavior in the self-standing MMM. (c) Separation results through HPLC analysis. Reproduced with permission from Ref. [205]. Copyright@2019, Wiley-VCH GmbH.

times [206]. However, the rapid expansion of nuclear power is accompanied by substantial challenges. One of the main obstacles is the surging demand for uranium fuel in reactors, which is projected to exceed double the current amount by 2040 [207]. The exploration of unconventional uranium resources, such as extracting uranium from seawater, is crucial for the sustainable development of nuclear energy. However, the process faces enormous challenges due to the extremely low concentration of uranium in seawater (only 3.3 µg L⁻¹), the presence of abundant competing ions, and the effects of biological erosion [208].

Another challenge arises during the reprocessing of spent fuel from nuclear power plants, where a substantial amount of radioactive wastewater containing various long half-life radioactive ions, such as $^{90}\mathrm{Sr}^{2+}$, $^{137}\mathrm{Cs}^{+}$, $^{129}\mathrm{I}$, $^{107}\mathrm{Pd}^{2+}$, and $^{99}\mathrm{TcO_4}^{-}$, is generated. These radioactive substances can be introduced into the environment via nuclear testing, nuclear accidents, medical waste, and industrial activities. Radiation may lead to genetic mutations, impacting the health of future generations and increasing the risk of genetic disorders; even low doses of radioactive materials may elevate the risk of cancer. Especially, Japan's irresponsible discharge of nuclear wastewater has greatly augmented the contamination of water bodies with radioactive materials. Effectively remov-

ing these radioactive ions is an essential prerequisite for the further treatment of radioactive waste liquid [209]. Spent fuel also contains abundant less-radioactive precious metals such as palladium, ruthenium, and rhodium, making the recovery of these precious metals from spent fuel crucial for resource utilization and hazard control [210].

Furthermore, the effluent gases from nuclear fuel and reprocessing plants containing radioactive xenon and krypton are a major problem that causes air pollution and health risks [211]. Xenon and krypton are considered the "gold gases" with crucial industrial and medical applications, these gases should be captured and reused in an efficient manner [212,213]. In the extraction process of these radioactive substances, adsorption based on physical interactions is considered as one of the most effective methods, due to its advantages of energy efficiency and simplicity of operation. The key issue to developing this method lies in the development of advanced adsorption materials, which should have excellent chemical and radiation stability, as well as specific recognition sites for the targeted radioactive substances. With diverse structures, large surface area, and tunable porosity, MOFs hold significant potential for applications in the extraction of radioactive substances. In fact, numerous MOFs have already been applied in related fields and have

shown excellent performance. This chapter aims to provide a comprehensive overview of the research conducted on the ability of MOFs to selectively capture radionuclides.

Ionic MOFs (iMOFs) are a crucial subset of MOFs that play a vital role in various applications [214]. These MOFs possess pores that can accommodate guests with charges opposite to that of the host framework. This unique characteristic makes iMOFs highly promising for the extraction of radioactive ions, as the counter ions present in the pores can be replaced by radioactive ions through an ion exchange process. In addition, the leaching probability of the trapped radioactive ions is also avoided as the entrapped guest is an integral part of the framework as a charge-balancing ion. Currently, researchers have achieved efficient adsorption and separation of radioactive ions such as Cs⁺, Sr²⁺, TcO₄⁻, SeO_3^{2-} , and SeO_4^{2-} based on this ion exchange method [215– 218]. For example, the highly efficient uptake of Cs⁺ has been realized by two robust layered cationic MOFs. The strong interactions between COO⁻ functional groups and Cs⁺ ions, easily exchangeable [(CH₃)₂NH₂]⁺, and anionic layer frameworks with open windows acting as "pockets" contribute to the high efficiency of Cs⁺ uptake [219]. Zhang et al. [220] developed a cationic-layered MOF that demonstrated remarkable efficiency in removing 90Sr2+ from both acidic solution and seawater. This exceptional performance was attributed to a unique two-step ion exchange mechanism between Sr^{2+} ions and the counter $[(CH_3)_2NH_2]^+$ within the MOF's pores. For the remediation of ⁹⁹TcO₄⁻, Wang et al. [221–223] and Shen et al. [224] pioneered the synthesis and application of hydrolytically-stable and radiation-resistant SCU-series MOFs to efficiently capture this oxyanion from the simulated waste liquid, which exhibits superior selectivity, fast kinetics, and high capacity. The single crystal of TcO₄ @SCU-101 has been disclosed that the excellent selectivity derives from the relatively hydrophobic cavity and the dense hydrogen bonding networks besides the electrostatic attraction [223]. In another case of nonradioactive analog ReO₄ @SCU-100, the combination of Ag-O-Re bonds from open Ag⁺ sites and multiple hydrogen bonds contributes to the high adsorption performance [222]. The presence of competing ions can have a significant impact on the performance of MOFs in the ion exchange adsorption of radioactive substances. Therefore, it is essential to enhance the selectivity of sorbents for radioactive substances by constructing MOFs tailored to the properties of the nuclides.

The structure of MOFs can be easily customized, allowing for the incorporation of specific recognition sites for radioactive substances in their pores. This can be done through pre-designed ligands or metal nodes, as well as PSM. By utilizing this approach, researchers have achieved effective adsorption and separation of a wide range of radioactive substances. One promising functional group for seawater uranium extraction is the amidoxime (AO) group, which can specifically bind to uranyl ions. Through PSM, AO can be introduced into the pores of MOFs to enhance their selective adsorption capacity for uranyl ions [225]. Other functional groups, such as amino, acylamino, hydroxy, carboxyl, and phosphorylurea groups, have also been shown to greatly improve the adsorption property of materials for uranyl ions [226–230]. Additionally, the introduction of groups that can coordinate with metal ions, such as carboxyl, sulfonic acid, and -NH- groups, can enhance the adsorption ability of materials for Th⁴⁺ ions [231–233]. In addition, -SO₃H functional MOFs are often used to adsorb Sr²⁺ and Cs⁺ from radioactive wastewater, and they exhibit excellent performance [234,235]. Crown ethers, which are supramolecular host compounds with cavities that can encapsulate guest molecules, can form stable complexes with different alkali metal ions. This makes them potential candidates for the adsorption of alkali substances. Introducing crown ethers into the pores of MOFs has been found to greatly enhance their selective adsorption capacity for Sr²⁺ and Cs⁺ ions [236]. Wang and co-workers [221] developed a stable 3D cationic MOF, SCU-102, capable of quantitatively removing TcO⁴⁻, even with an excess of nitrate and sulfate ions present. First-principles simulations indicate that the selective adsorption of TcO⁴⁻ by this material stems from the recognition function of the hydrophobic pockets of the struc-

According to the HSAB theory, Pd²⁺ belongs to the soft acid category. Therefore, functional groups with soft base sites (such as S, N atoms, *etc.*) often exhibit higher affinity towards Pd²⁺. By introducing such functional groups into the



Figure 16 (Color online) The adsorption of SCU-102 for TcO_4^- ions. Reproduced with permission from Ref. [221]. Copyright@2019, Wiley-VCH.

pores of stable MOFs through pre-ligand designedly synthesis or PSM, the adsorption performance of MOFs towards Pd²⁺ can be improved. UiO-66-NH₂ is an excellent choice for introducing such functional groups due to its exceptional stability and rich reactivity at the -NH₂ site. Functional groups like *o*-phenylenediamine, dithizone, allylsulfanyl, pyridyltriazole, and 2,6-diaminopyridine have been successfully incorporated into the pore channels of UiO-66-NH₂ through reactions with amino groups, resulting in excellent adsorption performance for Pd²⁺ ions [237–240].

As radioactive inert gases, ⁸⁵Kr, ¹³³Xe and ²²²Rn, have no dipole and quadrupole moments, it remains a huge challenge, therefore, to efficiently capture and selectively separate these spherical gas molecules with ultra-low concentrations from complex air components [241,242]. The features of precise regulation of pore size/shape and the pore polarization environment at the molecular level endow some MOFs to accurately identify Kr. Xe and Rn through strong affinity from confinement effect, achieving by effectively discriminating Xe/Kr based on their difference in the kinetic diameters (3.66 and 4.05 Å for Kr and Xe, respectively) and polarizability $(24.8 \times 10^{25} \text{ and } 40.4 \times 10^{25} \text{ cm}^{-3} \text{ for Kr and Xe, respec-}$ tively) [69]. A robust squarate-based MOF featuring matched pore size toward Xe and pore surface rich in polar hydroxyl groups affords a record-high affinity and selectivity for Xe over Kr [243]. Remarkably, data-driven design and computational screening methods have greatly accelerated the discovery and development of advanced MOFs for efficient adsorption and separation of radioactive inert gases [244,245]. According to the thermodynamic and kinetic equilibrium principle, a quasi-open apertured MOF material (ZIF-7-Im) was discovered and synthesized under the guidance of computational screening and modeling, which exhibited in-depth Rn removal behavior under ambient conditions, exceeding that of commercialized activated car-

bon [246].

In summary, the inherent adaptability and facile tunability of framework charges, coordination groups, pore size and polarizability, endow functionalized MOFs with unprecedented efficiency in adsorbing radioactive anions, cations, and inert gases (Figure 17). However, the pursuit of more efficient and practicable MOFs under specific conditions also remains a formidable challenge. From a fundamental research standpoint, artificial intelligence emerges as a transformative tool for high-throughput screening of MOFs with desired pore structures and removal properties. Concurrently, the crystalline nature intrinsic to MOFs provides an avenue to disclose the adsorption mechanism on the atomic level. The attainment of highly crystalline MOFs housing radioactive substances is still a tough nut to crack. In view of practical applications, molding, stability, and cost are the paramount concerns within MOFs. The diminutive crystal or powder morphology visible to the naked eve proves incongruous with real scenarios. Addressing this, the development of a universal molding approach for the transformation of powdery MOFs to bead-like or membranous structures emerges as an effective strategy. Subsequently, the long-term availability and recyclability of MOFs depend on stability enhancements achievable through bolstered coordination strengths and the formulation of composite materials. Moreover, the economic viability of MOFs as adsorbents is contingent upon mitigating the expense associated with complex organic ligands and time-consuming synthesis procedures. Consequently, the imperative lies in the development of eco-friendly, fast, and efficient synthesis methodologies, alongside the judicious selection of economically feasible ligands. Through a concerted effort to surmount these challenges, we posit that MOFs will find practical applications in the remediation of radioactive substances in the near future.

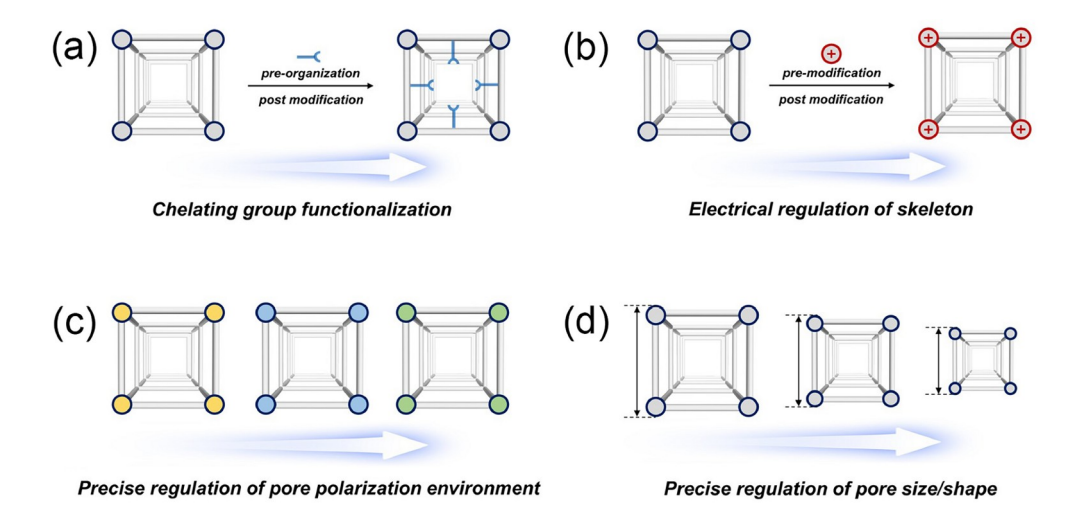


Figure 17 (Color online) Extraction of radioactive substances with MOFs via various strategies: (a) functionalization of chelating groups; (b) precise regulation of skeleton charges; (c) fine-tuning polarization within the pores; (d) meticulous control of pore sizes or shapes.

3.5 Capture and separation of environmental pollutants

Atmospheric pollutants refer to substances that pollute the atmospheric environment and have negative impacts on human health, ecosystems, and climate. Primarily includes inorganic gases such as sulfur dioxide, nitrogen oxides, carbon monoxide, and ammonia, along with volatile organic pollutants like benzene, freons, hydrocarbons, and solid particulates. MOFs, with their distinctive porous structures and extensive surface area, show great promise in pollutant adsorption and elimination. These characteristics make MOFs an ideal choice for dealing with pollutants in air and water [247,248]. MOF materials have been reported in the adsorption and separation of these atmospheric pollutants, and examples will be pro-vided below.

The majority of sulfur dioxide and nitrogen oxide emissions come from the combustion of fossil fuels, such as in automobiles, airplanes, and industrial furnaces, as well as the production and use of products like nitric acid and nitrogen fertilizers [249,250]. Nitrogen oxides and sulfur dioxide are seriously harmful to the human respiratory system and are also a significant cause of acid rain. Su and co-workers [251] used a versatile and manageable synthetic strategy to scale up the production of the MOF material DUT-67 from milligram scale to kilogram scale. The simple HCl post-treatment of DUT-67-HCl significantly enhanced its SO₂ capture capacity (Figure 18). Liu and co-workers [252] successfully synthesized NU-1000-PhTz using the solvent-assisted ligand incorporation (SALI) post-synthetic strategy. The incorporation of the thiazolium pillar into the structure significantly enhanced the material's adsorption capabilities, demonstrating exceptional adsorption performance for atmospheric pollutant N₂O.

Particulate matter consists of various chemical substances such as nitrates, sulfates, silicates, carbon, and ammonium, typically originating from industrial pollution, vehicle emissions, soil dust, coal combustion, and biomass burning. Zhang and co-workers [253] utilized the characteristic of ZIF materials that can be synthesized at room temperature, and through electrospinning technology, synthesized a nanofiber filter based on MOF materials in one step. The filter can effectively remove solid particulate matter from 15 to 100 nm, and has a high filtration efficiency of 99.1% for ultrafine particles (Figure 19).

Volatile organic compounds (VOCs) are organic compounds that easily evaporate into the atmosphere at normal temperature and pressure. These pollutants are diverse in type and broad in source, potentially causing serious impacts on the environment and human health. VOCs mainly include hydrocarbons (alkanes, alkenes, as well as aromatic hydrocarbons like benzene and toluene), oxygen-containing organic compounds (aldehydes such as formaldehyde and

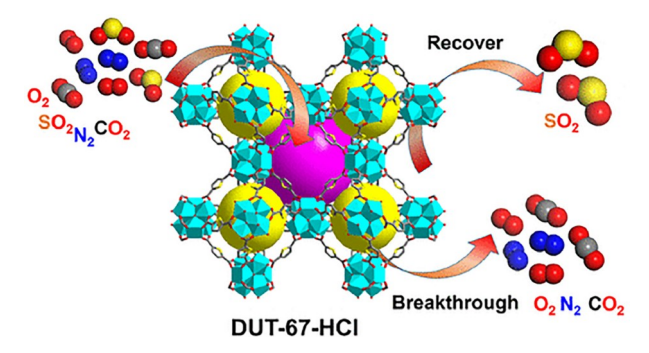


Figure 18 (Color online) The adsorption and separation of SO_2 by DUT-67-HCl. Reproduced with permission from Ref. [251]. Copyright@2023, American Chemical Society.

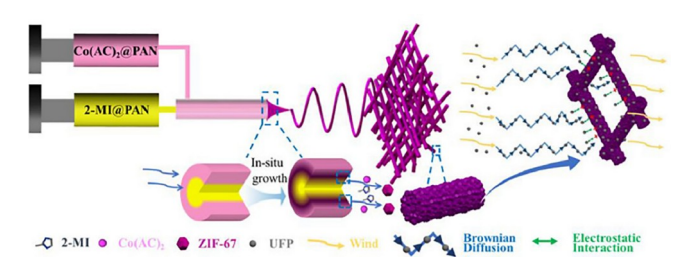


Figure 19 (Color online) MOF composite filter for the removal of particulate matter. Reproduced with permission from Ref. [253]. Copyright@2020, Elsevier.

acetaldehyde, ketones like acetone, alcohols, esters, ethers, etc.), nitrogen-containing organic compounds (such as pyridine), and halogenated organic compounds (such as trichloromethane, freons). For different types of VOCs, it is necessary to design and construct corresponding MOF materials based on the molecular structural characteristics of the VOCs, enhancing their interaction with the target VOCs and thus achieving improved adsorption and separation performance. The adsorption of hydrocarbon VOCs is typically exemplified by the recovery of dry gas in refineries. The recovery of light hydrocarbons from dry gas is very important for improving economic benefits and reducing environmental emissions. The process of dry gas recovery also involves the separation of light hydrocarbons, a subject that has been extensively reported and will not be elaborated here. For the adsorption of aromatic hydrocarbon VOCs, the design of adsorbents often focuses on enhancing the π - π interactions and $C-H\cdots\pi$ interactions between the adsorbent and aromatic hydrocarbon molecules.

Li and co-workers [254] successfully synthesized a series of double-walled metal-dipyrazolate frameworks (BUT-53 to BUT-58), demonstrating excellent capture capabilities for trace benzene. At 298 K and under pressures less than 10 Pa, the adsorption capacity for benzene reached $2.47-3.28 \text{ mmol g}^{-1}$. The crystal structure of the benzene-loaded phase $C_6H_6@BUT-55$ and DFT calculations indicate that the $C-H\cdots X$ interactions between the framework and

the benzene molecules are responsible for the effective adsorption performance towards benzene (Figure 20).

Water pollutants primarily include inorganic substances such as heavy metal ions, ammonia, and phosphorus, along with organic pollutants like synthetic dyes, antibiotics, pesticides, solvents, and surfactants, as well as radioactive substances and pathogens. These contaminants not only exert toxic effects on aquatic organisms and disturb the natural balance of ecosystems but also impact human health via the food chain. Heavy metal ions in water originate from a variety of sources, mainly from industrial activities such as mining, electroplating, and metal processing, and from agricultural products like pesticides and fertilizers, along with domestic wastewater. Heavy metal ions significantly threaten human health and ecosystems; certain ions can harm the nervous system and reduce cognitive functions, cause kidney dysfunction, and increase the risk of cancer. The adsorption of pollutants in water systems demands higher stability of MOF materials compared to adsorption of atmospheric pollutants, due to water's strong coordinating capability which has a strong destructive effect on MOF materials. Beyond the stability of MOF materials, the recyclability of adsorbents is a crucial aspect to consider for adsorbing pollutants in water systems. For example, integrating MOF adsorbents with magnetic materials can enhance the recovery and reusability of these materials.

Wang and co-workers [255] successfully prepared thiol-functionalized SH-MiL-68(In) using a PSM strategy. The incorporation of thiol groups allows SH-MiL-68(In) to effectively eliminate Hg(II) ions from water and exhibit robust cyclic stability. Mechanistic research shows that effective adsorption primarily results from the coordination interaction between the thiol groups in the framework and Hg(II) ions (Figure 21).

To facilitate the effective separation of adsorbents after adsorbing pollutants in water, Fu and co-workers [256] prepared a magnetic responsive composite material with a core-shell structure, Fe₃O₄@ZIF-8. This material has good water stability and a high specific surface area (1,133 m² g⁻¹), effectively removing As(III) from aqueous solutions. Utilizing the magnetic response of Fe₃O₄, this composite material can be easily separated and recovered by magnetic means after water treatment (Figure 22).

In addition, there are numerous organic pollutants in water bodies, such as pesticides, herbicides, polycyclic aromatic hydrocarbons, synthetic dyes, and PPCPs (pharmaceuticals and personal care products). Clenbuterol (CLE) and ractopamine (RAC) are typical β_2 -adrenergic agonists that pose serious threats to human health. Lv and co-workers [257] synthesized an ethyl-rich aluminum-based MOF (BUT-19), which exhibited excellent performance in removing CLE and RAC from water. The maximum adsorption capacities of BUT-19 for CLE and RAC are 294.1 and 366.3 mg g⁻¹, re-

spectively. The appropriate pore sizes and weak hydrogen bonding interactions between the framework and CLE/RAC molecules are the main reasons for the excellent adsorptive performance of BUT-19.

MOF materials are increasingly recognized for their high

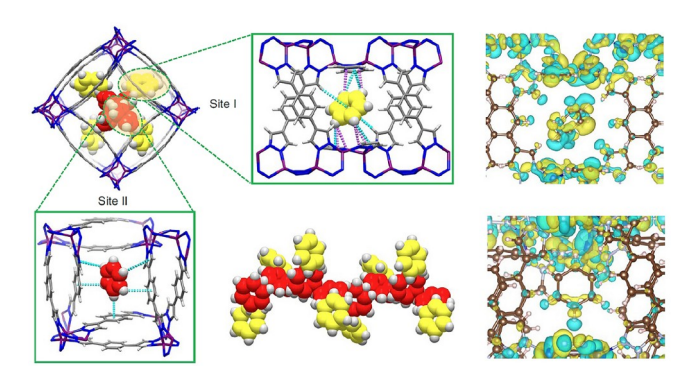


Figure 20 (Color online) The interactions between BUT-55 and benzene molecule. Reproduced with permission from Ref. [254]. Copyright@2022, Springer Nature.

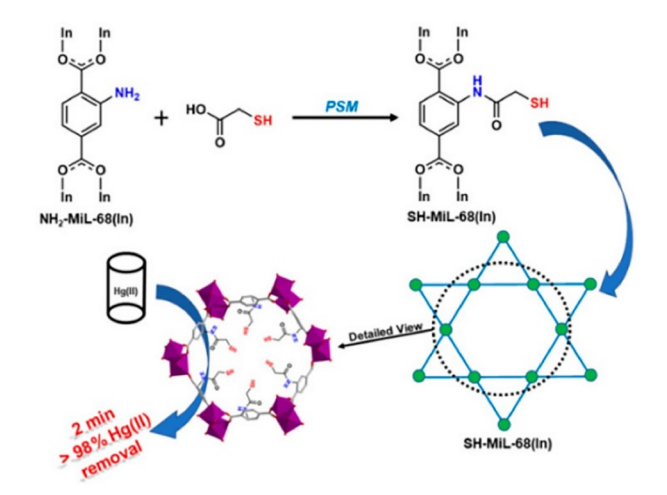


Figure 21 (Color online) The adsorption of SH-MiL-68(In) for Hg(II) ions. Reproduced with permission from Ref. [255]. Copyright@2019, American Chemical Society.

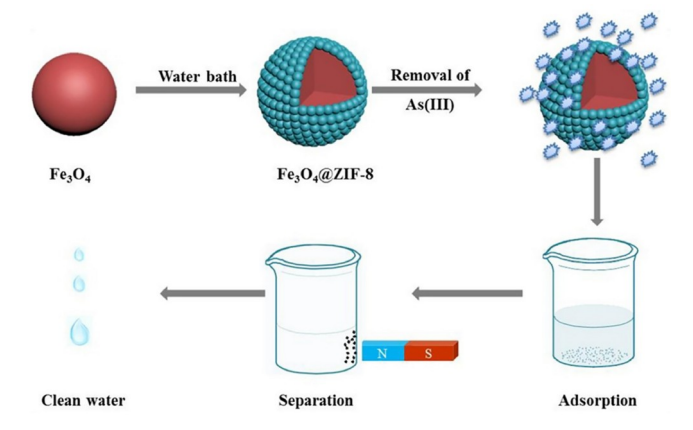


Figure 22 (Color online) Magnetic responsive composite material Fe₃ O₄@ZIF-8. Reproduced with permission from Ref. [256]. Copyright@2018, Elsevier.

adsorption capacity and selectivity in removing environmental pollutants. Furthermore, composite multifunctional materials made with magnetic, catalytic, and sensing materials are increasingly used in environmental management.

4 Optical performance

4.1 Luminescence mechanism

MOFs have unparalleled advantages in the field of photonics [258–264]. Firstly, there is a wide variety of alternative metal and organic ligands for arrangement and combination, resulting in designable MOFs with different luminescent properties; Secondly, while retaining the inherent characteristics of each photonic center, MOFs can also rely on the synergistic effect between different photonic units to generate more excellent photonic performance; Thirdly, the coordination mode and pore confinement of MOFs lead to the orientation of organic ligands and guest molecules along specific directions, resulting in new aggregation forms that are completely different from those in solid powders and solutions. This provides infinite possibilities for the application of MOFs in complex photonic functional fields [265].

Metal ions and organic ligands in MOFs can serve as photonic centers, and luminescent MOFs can also be constructed by introducing luminescent guest molecules. The luminescence mechanism of MOFs includes the following four types: (1) metal ion luminescence; (2) organic ligand luminescence; (3) charge transfer luminescence, including metal to ligand charge transfer luminescence (MLCT) and ligand to metal charge transfer luminescence (LMCT); (4) guest molecules luminescence.

The luminescence of metal ions in MOFs mainly comes from the f-f level transition of lanthanide ions (Ln³⁺). However, due to the fact that the f-f transition of Ln³⁺ is usually forbidden, the absorption ability of Ln³⁺ for excitation luminescence is weak, and the photoluminescence quantum efficiency (PLQY) of directly exciting Ln³⁺ is very low. Organic ligands have strong absorption ability in the UV-visible light range. Therefore, when organic ligands combine with Ln³⁺ to form MOFs, the light absorbed by the ligands can transfer to Ln³⁺ through the "antenna effect", thereby sensitizing the luminescence of Ln³⁺ [266].

The ligand-based luminescence of MOFs is usually based on the photoluminescence process of organic molecules. After the organic ligand absorbs a certain amount of photon energy, the electrons transition from the ground state to the excited state and then fall back to the ground state through a radiative transition, emitting fluorescence or phosphorescence. Due to the non-radiative transitions caused by the vibration of ligand molecules and the presence of aggregation-induced quenching (ACQ) in the solid state, most ligands exhibit weak fluorescence in the solid state. When

ligands coordinate with metal ions or metal clusters to form MOFs, the 3D network structure of MOFs can fix the ligands, improve the rigidity and stability of the ligands, and greatly reduce the possibility of non-radiative transitions [267]. The ordered arrangement of ligands in MOFs can also provide effective separation between ligands, reducing fluorescence quenching induced by molecular aggregation. If the ligands in MOFs do not undergo energy transfer (EnT), they will exhibit a spectral shape similar to the ligands, but the fluorescence intensity and PLQY will be greatly improved [268].

Charge transfer luminescence is generated by the radiative transition of electrons from the excited state of charge transfer to the ground state. According to the different ways of charge transfer, it can be divided into LMCT and MLCT [269]. LMCT represents an electronic transition from an organic ligand orbit to a metal central orbit, while MLCT represents an electronic transition from a metal central orbit to an organic ligand orbit. Usually, charge transfer luminescence can be observed in MOFs constructed by metal ions with d¹⁰ electron arrangement.

In addition to the inherent metal ion luminescence and organic ligand luminescence of MOFs, their porous properties are also very conducive to the design of host-guest materials. MOFs have a large specific surface area and high porosity, making them suitable as host materials. By introducing luminescent units such as Ln³⁺ ions, organic dyes, and quantum dots (QDs) as guest molecules, host-guest MOFs with unique photonic properties can be constructed [270,271].

4.2 White emission

The distinct pore structure of MOFs makes them an excellent host matrix for confining and isolating luminescent guest species (such as organic dyes), leading to multiple emissions and tunable colors and an optimized white light emitting (WLE) phosphor. In 2015, Qian et al. [272] presented a creative strategy to achieve WLE via dye-encapsulated MOFs, the PLQY of this dye/MOF phosphor is much higher than that of mixed-lanthanide MOF phosphor, providing a new perspective for the development of high-performance WLE diode (WLED). It is worth noting that the confinement and isolation of dye molecules in MOF channels greatly restrict the intramolecular torsional motion and thus diminish the ACQ, resulting in enhanced PLQY in dye/MOF materials. Subsequently, different research groups reported a large number of new dye/MOF host-guest materials used as WLE phosphors [273,274].

Following this route, Qian *et al.* [275] constructed a novel yellow phosphor by simultaneously incorporating three dyes, Coumarin 6 (Cou-6), Rhodamine 6G (R6G), and Rhodamine 101 (R101), into ZJU-28. Effective EnT processes between

these dyes within MOFs enable the ZJU-28⊃Cou-6/R6G/R101 phosphor to emit warm white light with a high PLQY of 82.9% (Figure 23). Bright and warm WLE with color-rendering index (CRI) value of 88, correlated color temperature (CCT) of 4,446 K and luminous efficiency of 126 lm W⁻¹ was obtained. In 2020, Qian *et al.* [276] designed and synthesized the polyurethane-coated highly-stable MOF phosphor ZIF-8⊃pm546/pm605/SRh101 (pm546, pyrromethene 546; pm605, pyrromethene 605; SRh101, sulforhodamine 101) via an *in situ* self-assembly process.

Following the dye@MOF host-guest route, Xie et al. [275] fabricated a series of Rh@bio-MOF-1 (Rh = rhodamine) with a high internal PLQY (79%) through a solvothermal reaction followed by cation exchanges. In 2019, Gong et al. [277] fabricated a WLE core-shell crystal, CD-MOF>7-HCm@FL@RhB (shell@core, CD-MOF stands for cyclodextrin MOF, 7-HCm stands for 7-hydroxycoumarin, FL stands for fluorescein). With three sequentially formed and adjustable layers of different dyes, bright white light with a CIE coordinate of (0.35, 0.32) can be achieved from the coreshell crystal. In 2019, Su et al. [278] fabricated a Zn-based MOF LIFM-WZ-6 using a TPE-based ligand H₄TATZTPE. Then a series of dye@MOF materials were obtained using the host-guest strategy. Besides the traditional one-photon absorption (OPA) pathway when excited by 365 nm UV light, WLE can also be achieved from the NIR-excited (800, 790, and 730 nm) two-photon absorption (TPA) pathway (Figure 24). It is worth noting that the TPA pathway has more potential applications due to its low excitation energy and deep penetrability.

Apart from the MOF>dyes phosphor, PQDs/MOF (PQDs, organic-inorganic halide perovskite quantum dots), have attracted particularly tremendous interest in recent years due to their potential applications in WLEDs. For instance, Wang and co-workers [279] developed a two-step synthetic strat-

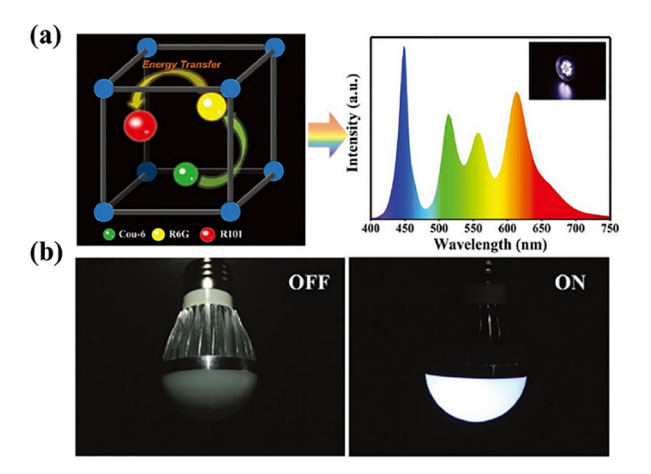


Figure 23 (Color online) (a, b) Schematic illustration of the EnT processes and used for WLED in ZJU-28⊃Cou-6/R6G/R101. Reproduced with permission from Ref. [275]. Copyright@2018, Wiley-VCH GmbH.

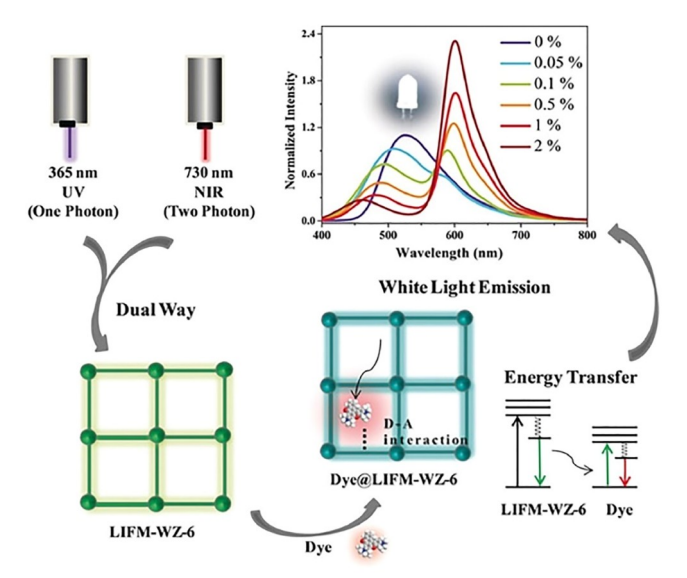


Figure 24 (Color online) Schematic Illustration of OPA and TPA dual-way excited WLE in dye@LIFM-WZ-6 systems. Reproduced with permission from Ref. [278]. Copyright@2019, Wiley-VCH GmbH.

egy to obtain the CsPbX₃@ZJU-28 (X = Cl, Br, and I) composites by introducing PQDs into ZJU-28. WLEDs with diverse emission colors were achieved by adjusting the halide components of CsPbX₃ in ZJU-28, with CIE of (0.3812, 0.3527), CCT of 3,748 K and CRI up to 84.2. Apart from the PQDs@MOF host-guest strategy, Fei *et al.* [280] constructed a series of WLE MOFs TMOF-5(X) when 1,4-benzenedicarboxylate (bdc) as ligand and the deformable lead halide units, [Pb₂X₃]⁺ (X=Cl, Br, or I) 1D chains served as SBUs. The Eu³⁺@TMOF-5(Br) host-guest shows the transition from a CCT of 4258 K for bright white-light to a CCT of 7993 K for "cold" white-light.

5 Sensing and detection

5.1 Temperature

Luminescent thermometers have obtained fruitful progress due to their unique benefits, such as noninvasive operation, high sensitivity and fast response. Usually, the luminescent properties (such as intensity, wavelength, lifetime, *etc.*) of the material can be applied to luminescent thermometers. In 2012, Qian *et al.* [281] first proposed and constructed mixed lanthanide MOFs (usually Tb³⁺ and Eu³⁺) as ratiometric luminescent thermometers. Compared with traditional temperature detection based on a single fluorescence emission intensity, ratiometric luminescent thermometer-MOFs can establish internal standards by utilizing the intensity ratios of different emission peaks, thereby eliminating external interference and achieving highly sensitive and selective self-calibration fluorescence temperature detection.

In 2019, Zhao et al. [282] proposed a new luminescent

Ln-MOF thermometer strategy by selecting ligands 6-(4-carboxyphenyl) nicotinic acid and 2,2'-bipyridine-5,5'-dicarboxylic acid (bpydc) with different energy levels to prepare $Tb_{0.95}Eu_{0.05}cpna$ and $Tb_{0.95}Eu_{0.05}bpydc$. Especially in this system, without changing the MOF structure and coordination mode of Ln^{3+} ions, the triplet energy level (T_1) of the ligand can effectively regulate the EnT process within the mixed-Ln-MOF, thereby adjusting the temperature sensing performance. Similarly, in 2021, Zhao *et al.* [283] continued to synthesize three completely isomorphic Eu^{3+}/Tb^{3+} mixed MOFs with different T_1 : $Eu_{0.01}Tb_{0.99}BDC$ -OH, $Eu_{0.01}Tb_{0.99}BDC$ -OH, $Eu_{0.01}Tb_{0.99}BDC$ -NH₂, and $Eu_{0.01}Tb_{0.99}NDC$, and used them for temperature detection.

Although the above methods are very attractive for the development of ratiometric luminescent thermometers, the available emission is limited to the Ln-MOFs, namely Ln³⁺ ions and ligands. In 2015, Qian et al. [271,284] first proposed that the encapsulation of organic dves into the pores of MOFs to form MOF⊃dye composites is a promising method for developing novel ratiometric luminescent thermometers, as it can expand the emission range. Very recently, Qian et al. [285] constructed a dual-emitting ZIF-8>4-Mu+Flu composites by simultaneously incorporating two types of luminescent dyes (blue emitting 4-Mu (4-methylumbelliferone) and green emitting Flu (fluorescein)) in the pores of a nanoscale ZIF-8 through an *in-situ* strategy. The ZIF-8⊃4-Mu +Flu composites achieved multimode temperature sensing (luminescent intensity ratio and maximum emission wavelength) with high spatial resolution (Figure 25). Following this route, two types of NbO-type MOF guest composites, DSM@ZnPZDDI and Eu³⁺@ZnPZDDI (H₄PZDDI = 5,5'-(pyrazine-2,5-diyl)diisophthalic acid) were obtained and evaluated for use as potential ratiometric temperature probes by Zhao et al. [286]. Similarly, in 2019, Li et al. [287] also reported MOF Zn₃(benzene-1,3,5-tricarboxyl)₂(adenine)-(H₂O) (ZnBTCA), as a host and thermosensitive fluorescent dves as guests, a series of dve@ZnBTCA (Acf, acriflavine; RB, Rhodamine B) is synthesized and studied as luminescent ratiometric thermometers. These reported cases indicate that constructing novel MOF>guest materials with multiple emission centers through the host-guest strategy is a very effective method, which will undoubtedly promote the rapid development of MOF luminescent thermometers in the field of biological temperature self-calibration ratio sensing applications.

Recently, MOF-film thermometers have drawn much attention due to their potential for mapping the temperature distribution and thermal gradient over a large surface. To overcome the limitations of poor stability of MOFs materials, Wang *et al.* [288] prepared Tb_{0.98}Eu_{0.02}-BTC thin films using *in-situ* growth method and achieved proportional temperature sensing in the temperature range of 298–383 K, with a $S_{\rm m}$ of 16.14% K⁻¹ at 359 K. They further studied the

effect of this thin film on temperature imaging. In 2020, Li *et al.* [289] prepared a flexible mixed Ln-MOF Eu_{0.0025}Tb_{0.9975}-BABDC-PBMA polymer hybrid film using 2,5-bis(allyloxy) via photoinduced copolymerization (Figure 26). Eu_{0.0025} Tb_{0.9975} BABDC PBMA thin film retains the flexible form of mixed Ln-MOF while exhibiting good structural integrity and excellent linear luminescence response behavior to temperature. Sensitive detection can be achieved within the range of 90–240 K, with a $S_{\rm m}$ of 3.61% K⁻¹ at 240 K. Similarly, in 2021, Chen *et al.* [290] prepared a Cdots&RB@ZIF-8²-MMM for dual-luminescence ratiometric ($I_{\rm C}/I_{\rm RB}$) temperature sensing at 20 °C–80 °C.

5.2 Pressure

A significant development for environmental monitoring is

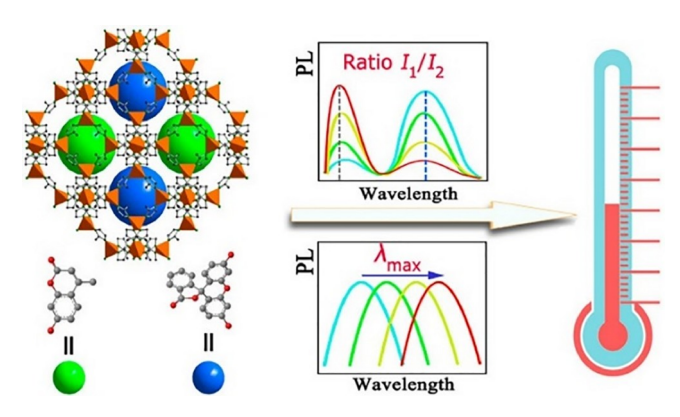


Figure 25 (Color online) Schematic illustration of multimode temperature detection in ZIF-8⊃4-MU&Flu composite based on the luminescent intensity ratio and maximum emission wavelength. Reproduced with permission from Ref. [285]. Copyright@2021, American Chemical Society.

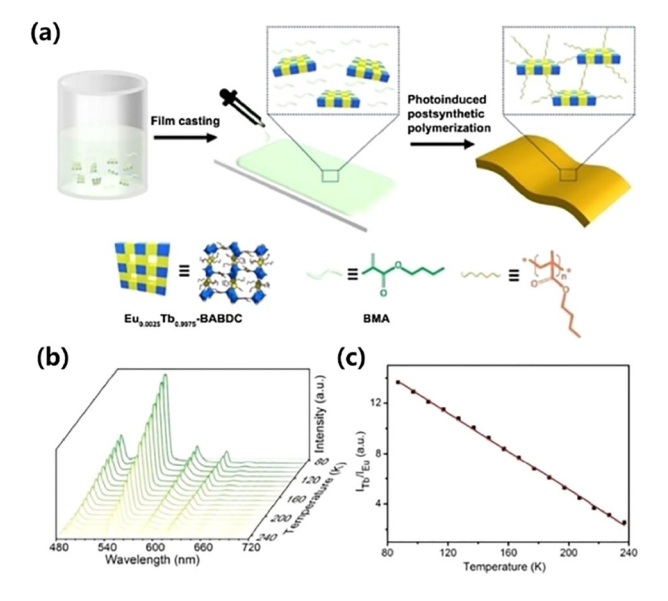


Figure 26 (Color online) (a) Fabrication and (b, c) temperature sensing of Eu_{0.0025}Tb_{0.9975}-BABDC-PBMA films. Reproduced with permission from Ref. [289]. Copyright@2020, Wiley-VCH GmbH.

the realization of sensitive and quick response detection of sulfur dioxide (SO₂), oxygen (O₂), hydrogen sulfide (H₂S), ammonia (NH₃), and VOCs in the environment [291–293]. Although pure MOFs have made significant progress in the field of luminescent gas pressure sensors, considering the insufficient variety of materials and the slow development of MOF gas sensors, this field remains one of the most challenging topics. In recent years, the application of luminescent MOF thin film materials for gas pressure sensing has attracted widespread attention from researchers.

In 2022, Hong et al. [294] achieved an AIEgen-based MOF, FJI-H31 [Ln(TPDB)·2DMF·2H₂O]·NO₃ (Ln = Gd^{3+} , Eu³⁺) as luminescent pressure sensors. Under ambient conditions (101.3 kPa), the FJI-H31 shows bright luminescence; however, in a vacuum, no emission was observed, and it can back to its initial state upon the recovery of the gas pressure. In 2022, Bu et al. [295] also reported an AIEgen-based luminescent Ln-MOF, NKU-200-Eu that was capable of realizing sensitive real-time in situ visual detection of THF vapor (vacuum to 21.62 kPa). In particular, luminescent pressure sensors also allow convenient and ultra-efficient detection of VOCs. In 2023, Mo et al. [296] report a new flexible MOF, namely [Sr₂(BINDI)(DMF)(H₂O)]·G (WYU-61. $H_4BINDI = N_1N'-bis(5-isophthalic acid)$ -naphthalenediimide, G = 0.8DMF), which can transform from a discrete zero-dimensional (0D) pore framework to a 1D pore opening one owing to the single-crystal to single-crystal (SCSC) transformation process. Interestingly, the pore-opening phase shows sensitive and significant fluorescence enhancement for benzene vapor and other aromatic hydrocarbon vapors (Figure 27). Lang and co-workers [297] reported a rigid Cu(I)-based MOF $[Cu_4I_4(Py_3P)_2]_n$ (1) for the detection of the chloroalkane molecules (CH₂Cl₂ or CHCl₃).

To address the needs of realistic optoelectronic sensor applications, it is crucial to produce MOF films with various substrate types. These MOF films have several advantages, such as being portable, stable in the face of a gas flux ex-

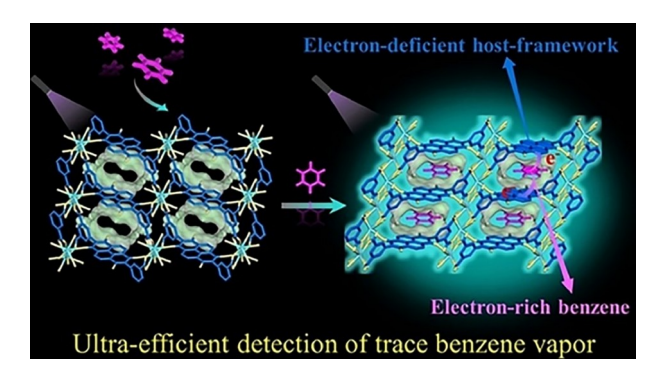


Figure 27 (Color online) Schematic for detection of trace benzene vapor by WYU-61. Reproduced with permission from Ref. [296]. Copyright@2023, Wiley-VCH GmbH.

plosion, and fully contacting analysts [298]. On the basis of preliminary work, Qian et al. [299] prepared a flexible MOF thin film by mixing highly stable nanoscale Al-MIL-53-NO₂ with polyvinylidene fluoride (PVDF). Due to the uniform distribution of Al-MIL-53-NO₂ particles and the permanent porosity of the MOF, the thin film exhibits good water permeability flux, while also allowing for complete contact between the analyte and the material during the detection process (Figure 28). The sensor made from this thin film has excellent selectivity and sensitivity for H₂S, with a detection limit of 92.31 nmol L⁻¹. In another work, Qian et al. [300] prepared MIL-100(In) \(\sum_{\text{e}}\) Eu^3+/Cu^2+ fluorescent film using post modification method, and turn-on fluorescence detection of H₂S was achieved at room temperature with a detection limit of 0.535×10^{-6} . These results demonstrated that luminescent MOF films have great potential application prospects in the field of fluorescence sensing, and are also conducive to the preparation of fluorescence sensor devices.

5.3 Small molecules or ions

Over the past decade, luminescent MOFs have been widely used for the detection of anions and cations, amino acids, thiols, and simple organic small molecules [301–312]. However, the detection of complex molecules that are particularly important for the human body and environment, such as biomarkers [313–317], chiral molecules [318,319], and highly toxic pollutants [320,321], which is still in fancy and requires further research by researchers. In response to this, considering the structural designability, pore structure, and rich open sites of luminescent MOFs, we have selected several representative works for a brief summary, in order to better understand the relationship and sensing mechanism between small molecules and MOFs.

Taking highly toxic pollutants as an example, a large amount of toxic and harmful pollutants has been posing a great threat to human health and the environment. Therefore, achieving sensitive and accurate detection of these pollutants is one of the important topics for researchers. Among them, luminescent MOF sensors are considered to be promising small molecule sensor materials. For instance, Li *et al.* [320] reported a highly stable zirconium-based MOF, BUT-17, Zr₆O₄(OH)₈(HCOO)₂(CPTTA)₂ (H₄CPTTA, 5'-(4-carboxyphenyl)-[1,1':3',1"-terphenyl]-3,4",5-tricarboxylic acid) for the recognition and sensing of two representative persistent and highly toxic organic pollutants polychlorinated dibenzop-dioxins (PCDDs), 2,3-dichlorodibenzo-p-dioxin (BCDD) and 2,3,7,8-tetrachlorodibenzo-p-dioxin (TCDD), based on the fluorescence quenching (Figure 29).

The majority of luminescent sensors rely on the conventional key-and-lock mechanism, which is comparable to antigen-antibody, enzyme, and protein. In contrast, array

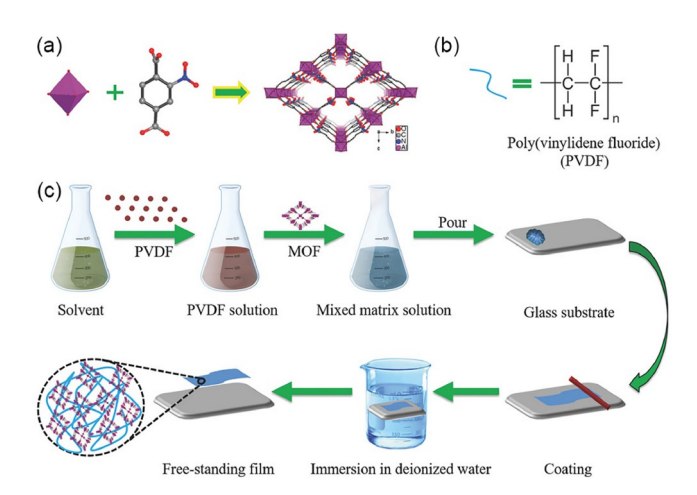


Figure 28 (Color online) (a) 3D framework structure of Al-MIL-53-NO₂. (b) The structure of PVDF. (c) Process for formation of MMMs. Reproduced with permission from Ref. [299]. Copyright@2018, Wiley-VCH GmbH.

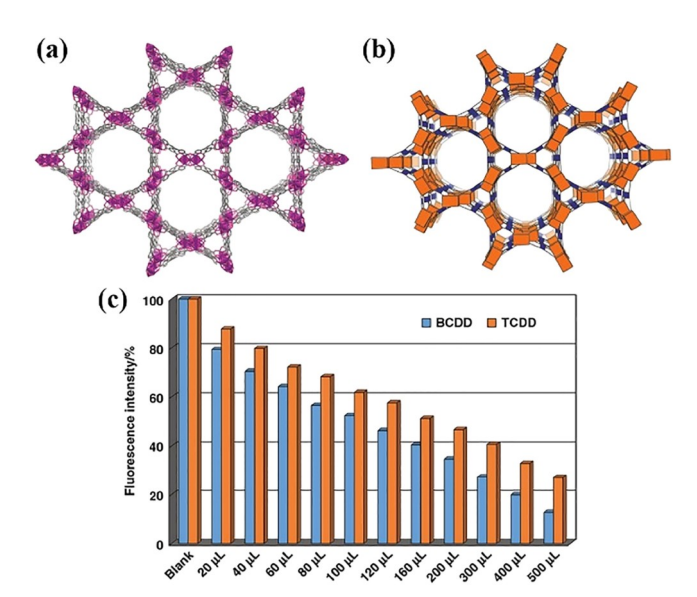


Figure 29 (Color online) (a, b) Crystal structure and topology of BUT-17. (c) Fluorescence-quenching titrations of BUT-17 by TCDD and BCDD. Reproduced with permission from Ref. [320]. Copyright@2019, Springer Nature

sensing uses the combined response of several sensors to identify complicated mixes or several analytical substances. Very recently, Qian *et al.* [322] designed a novel luminescent sensor array MOF-253⊃Eu³⁺+DOC with three emission centers by simultaneously assembling Eu³⁺ and organic dye 3,3'-diethyloxacarbonyl iodide (DOC) into MOF-253 (Figure 30). Within the concentration range of 0–60 μm, five metal ions, including Ag⁺, Cu²⁺, Fe³⁺, Co²⁺, and Ni²⁺, can be distinguished with up to 100% recognition accuracy by employing the differences in quenching responses of these ions to distinct emission centers. Consequently, it is also possible to successfully discriminate between binary and ternary combinations of the three metal ions Fe³⁺, Co²⁺, and

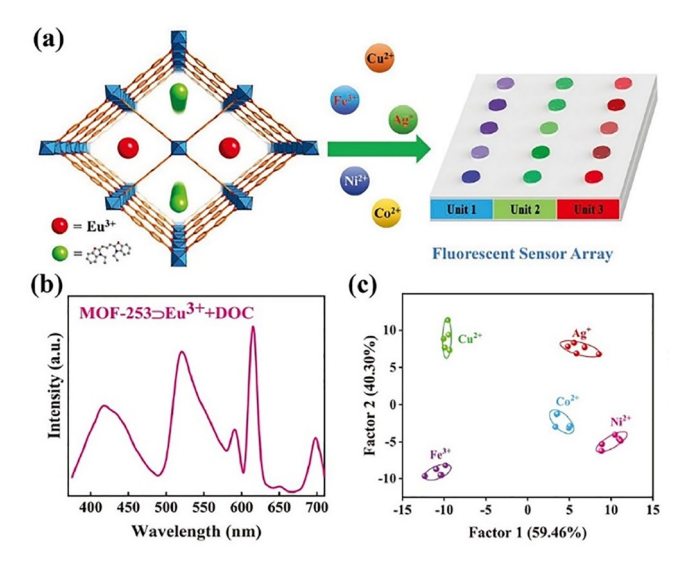


Figure 30 (Color online) (a) Schematic of the construction of MOF-253⊃Eu³⁺+DOC sensor array. (b) PL spectra of MOF-253⊃Eu³⁺+DOC. (c) Canonical score plot of the response patterns obtained from LDA against the binary or ternary metal ions mixtures of Fe³⁺, Co²⁺ and Ni²⁺. Reproduced with permission from Ref. [322]. Copyright@2021, Wiley-VCH GmbH.

Ni²⁺. Similarly, in 2023, Qian *et al.* [323] reported a Eu³⁺/Tb³⁺@UiO-66-(COOH)₂/NDC hydrogel film-based luminescent sensor array that shows good performance in distinguishing three nitrophenol isomers at 40–100 mM concentrations. The development of luminescent sensor assays in the environment and food safety fields will have a new direction thanks to the host-guest approach, which involves encapsulating different luminescent guest species as guests into MOFs to create luminescent sensor arrays with multiple emission centers.

Considering the poor stability of pure luminescent MOFs and the limitations in their application in optical sensor devices, researchers believe that preparing MOF thin film materials can effectively address these shortcomings and expand the application scenarios of luminescent MOFs. In 2021, Liang et al. [324] covalently coupled the molecule of 5-isothiocyanofluorescein (5-FITC) with a MOF [Eu(attpt)_{1.5}- $(phen)(H_2O)$ ₁ $(H_2attpt = 2$ -aminoterephthalic acid; phen = 1,10-phenanthroline) to prepare dual-emitting EuMOF-FITC composite (Figure 31). EuMOF-FITC exhibits turn-on fluorescence detection performance for biogenic amines (BA) in the concentration range of 5–50 mg L^{-1} , accompanied by a significant color change from orange-red to green. In addition, this probe also displays similar turn-on fluorescence and ratiometric detection of other biogenic amines, revealing potential applications based on monitoring the total biogenic amine content in spoiled foods. By integrating with a portable monitoring system based on smartphones, EuMOF-FITC flexible film can monitor the freshness of raw fish samples by sensing biogenic amine vapors.

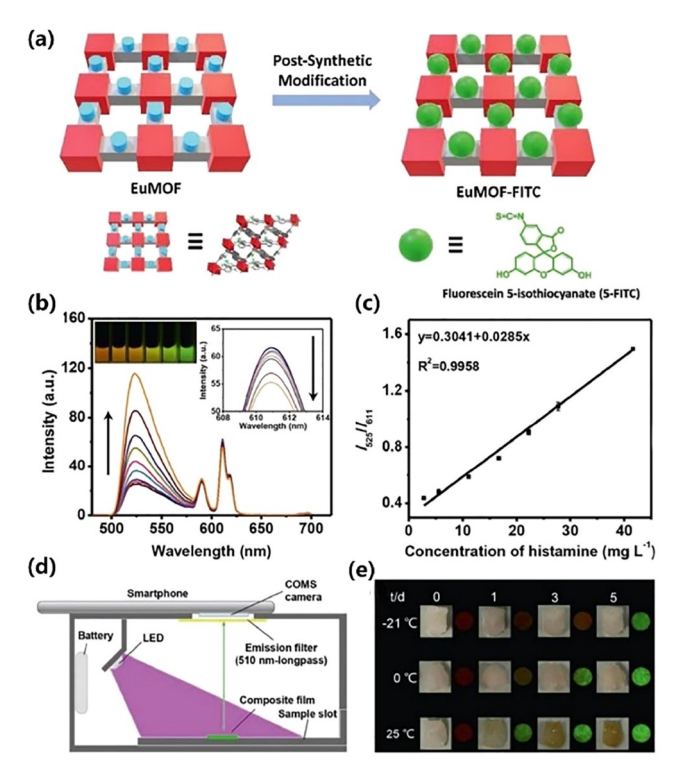


Figure 31 (Color online) (a) Schematic representation of the preparation of EuMOF-FITC PET. (b) Fluorescence sensing and (c) fitting curve of EuMOF-FITC *versus* histamine concentration. (d) Light path diagram of smartphone-based portable devices. (e) Monitoring the freshness of fish stored at different temperatures by EuMOF-FITC composition film. Reproduced with permission from Ref. [324]. Copyright@2021, Wiley-VCH GmbH.

6 Chemocatalysis

6.1 Coupling reactions

MOFs have been intensively studied as heterogeneous catalysts for the production of various fine chemicals via broadscope organic reactions [325–327]. The high modularity of MOFs has enabled the deliberate design of customized catalysts with unambiguous catalytic sites for specific organic transformations. In this regard, coupling reactions, typically C-C and C-heteroatom coupling reactions, have been broadly studied and congruously recognized as one of the most reliable, accurate, and powerful tools in chemists' arsenal [328]. MOFs were employed as efficient solid catalysts for promoting coupling reactions by mainly utilizing either Lewis or Brønsted acidity. In general, metal nodes or organometallic ligands bearing open coordination sites can potentially act as Lewis acidic sites, while metal nodes or organometallic ligands carrying active protons can be employed as Brønsted acidic sites.

Of all the transition metal nodes that can offer Lewis acidic sites, zirconium (Zr) is one of the most investigated species in terms of versatility and efficacy. The very first MOFs (UiO-66, 67, 68) built of Zr nodes were reported by Lillerud *et al.* [329]. Over the years, extensive pre- and post-synthetic

modification methods have been demonstrated to be capable of generating Lewis acidic Zr sites in UiO-MOFs for enhancing their catalytic activity. The high surface area and remarkable thermal and chemical stability of UiO-MOFs have superior advantages over low valent metal ion-based MOFs in heterogeneous catalysis. Cohen and co-workers [330] designed an organic ligand bearing chelating bipyridyl moieties and successfully assembled the ligand with Zr⁴⁺ to generate an isostructural Zr-MOF (UiO-67-bpydc). The metalation of UiO-67-bpydc with PdCl₂ yielded an organometallic ligand, which was employed as a heterogeneous catalyst for Suzuki-Miyaura coupling reactions (Figure 32).

In comparison to Lewis acid sites, Brønsted acid sites, i.e., protons, have played a decisive role in this area, through which, a vast amount of coupling reactions can take place in the absence of metals, thus avoiding metal contamination and allowing easy product purification. In 2003, Clearfield et al. [331] demonstrated an SO₃ sulfonated microporous zirconium-phosphonate framework that showed Brønsted acidity close to that of 100% H₂SO₄. Since then, a lot of research endeavors have been dedicated to the utilization of sulfonated or sulfated MOFs as solid acid catalysts for coupling reactions. A representative example was reported by Yaghi and co-workers [332] in 2014. They demonstrated the introduction of superacidity in the Zr₆ nodes of MOF-808 through simple sulfuric acid submersion, and the resulting superacidic MOF was catalytically active in Friedel-Crafts acylation reactions of anisole and different acylation reagents with up to 100% conversion (Figure 33). With this robust superacidic MOF catalyst, Yaghi et al. [332] further achieved the challenging catalytic dimerization and/or oligomerization of light olefins (C3–C6) with excellent performances at relatively moderate conditions. Subsequently, Doan and co-workers [333] prepared an isostructural Hf-MOF-808-SO₄ and demonstrated its use in heterogeneous coupling reactions of substituted 2-aminophenols and arylaldehydes to afford benzoxazoles under solvent-free conditions with high isolated yields.

In addition to the Zr and Hf-based MOFs, MIL-101 and MIL-53 based on kinetically inert Cr clusters have also been explored as Brønsted acid catalysts for catalyzing various coupling reactions. For example, Luan *et al.* [334] synthesized an aromatic sulfonyl group functionalized MIL-101 by PSM of amino-tagged linkers. The resultant strong Brønsted acidity embedded in the organic ligands was proved to be effective in promoting [4+2] self-coupling reactions of 1,1-diphenylethylenes in a protonation, Hetero-Diels-Alder (HDA) and elimination cascade sequence. Abbasi and coworkers [335] developed a stepwise strategy to graft sulfonate at the metal nodes of MIL-101. First, MIL-101 was thermally activated to generate unsaturated metal sites and then functionalized with cysteamine, oxidated with hydrogen peroxide, and acidificated with diluted sulfuric acid, to afford

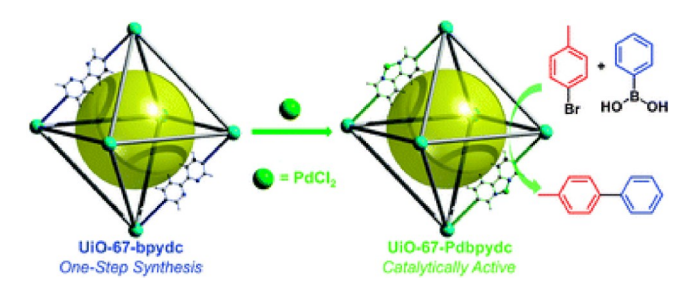


Figure 32 (Color online) Synthesis of the Lewis acidic UiO-67-bpydc catalyst for Suzuki-Miyaura coupling reaction. Reproduced with permission from Ref. [330]. Copyright@2014, Royal Society of Chemistry.

Brønsted acidic MIL-101-SO₃H. The catalyst was elaborately characterized and employed in the acetalization of benzaldehyde derivatives with ethylene glycol, giving an impressive catalytic performance.

In addition to designing and preparing MOFs with single functionality of either Lewis or Brønsted sites, bifunctional MOF catalysts are more intriguing and can potentially promote sequential or tandem catalysis by virtue of synergistic effects. In this case, PSM has provided customed control on the structure and fine-tuning of the functionality toward a particular catalytic activity. Ma and co-workers [336] deliberately designed a MIL-101-based bifunctional system (Al(III)@MIL-101-SO₃H) through the post-synthetical introduction of Lewis acidic Al(III) moieties and Brønsted acidic -SO₃H moieties. The hypothesized coordination environment of Al(III) indicated a very close geometric position between Al(III) and -SO₃H, the prerequisite for the synergistic effect. The catalyst was shown to effectively catalyze the benzylation of aromatic hydrocarbons (benzene, xylene, and mesitylene) with benzyl alcohol on a fixed-bed reactor. In all substrates, the catalytic performance of the bifunctional Al(III)@MIL-101-SO₃H catalyst is comparable to benchmark H-mordenite and H-β. Given the inferior performance of control experiments using Brønsted acidic MIL-101-SO₃H and Lewis acidic AlCl₃ as catalysts, respectively, it is clear that the synergy between the two distinct acidic sites has contributed significantly in enhancing catalytic activity and highlighted the bifunctional approach as a promising new approach toward highly active MOFbased acid catalysts (Figure 34).

6.2 Catalytic asymmetric reactions

Over the past two decades, the research community has witnessed the striking growth of CMOFs at the forefront of chiral solid-state materials and chiral technology. Explicitly, by virtue of the high modularity, the interior pore surfaces of CMOFs can be systemically tailored in hyperfine accuracy for the benefit of suitable host-guest interactions that have not been realized by conventional chiral materials, where chemo-, regio-, and even enantio-selectivity can be created

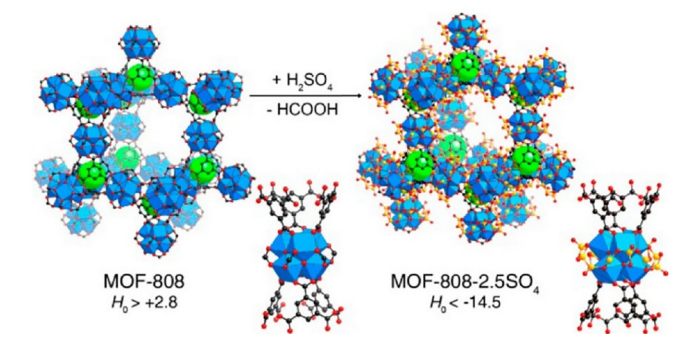


Figure 33 (Color online) Synthesis of the MOF-808-SO₄ with H₂SO₄. Reproduced with permission from Ref. [332]. Copyright@2014, American Chemical Society.

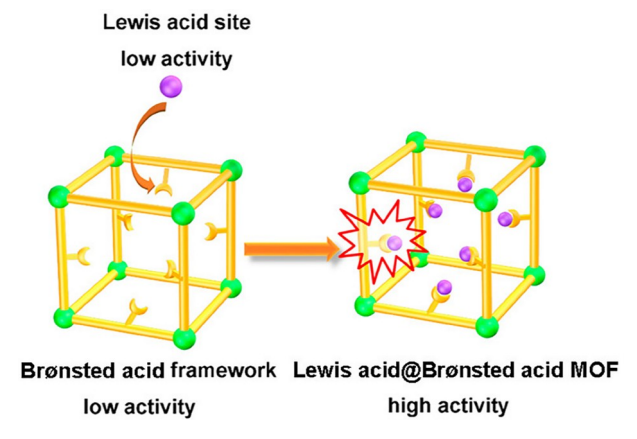


Figure 34 (Color online) Schematic presentation of the synthesis strategy for Lewis acid@Brønsted acid MOF. Reproduced with permission from Ref. [336]. Copyright@2015, American Chemical Society.

and modulated at an atomically level. The first report using CMOF as heterogeneous catalysts can be traced back to 2000, when Kim and co-workers [337] reported the asymmetric transesterification reaction with a chiral MOF termed *POST*-1, albeit with a very lower level of enantioselectivity. Since then, a number of CMOFs with potential catalytic sites have been synthesized and evaluated in diverse asymmetric reactions. In general, CMOF catalysts can be catalogued into two types dependent on the nature of catalytically active sites, *i.e.*, chiral organometallic catalyst and chiral organocatalyst.

Organometallic complexes have been widely employed as homogeneous catalysts for a broad scope of organic transformations attributed to their adjustable Lewis acidity. Dominating this subgroup of catalysts are chiral 1,1'-binapthyl-2,2'-diol (BINOL), 2,2'-diphenylphosphino-1,1'-binaphthyl (BINAP), biphenol, and metallosalen struts, which are well-known as chiral-privileged catalysts [338]. It was demonstrated to be an effective approach by incorporating these organometallic catalysts into the backbones of frameworks, leading to plenty of programmable CMOFs with well-established catalytical sites. In such cases, the CMOFs

can be regarded as highly-ordered 3D arrays of chiral coordination complexes. Compared to other immobilization approaches, the proposed strategy here allows the formation of heterogeneous asymmetric catalysts with precise structures, higher catalyst loading as well as excellent uniformity. Moreover, the robust framework and the isolated pores or channels can help stabilize the catalytically active single-site metal sites by efficiently isolating them in a manner similar to the peptide architecture of enzymes in biological systems.

Chiral BINOL-based metal complexes featuring C_2 symmetric backbones have been broadly employed in many important asymmetric reactions. The high advantage of this approach in heterogeneous asymmetric catalysis was first demonstrated by Lin's group [339] in 2005 when they succeeded in creating a catalytically active porous CMOF with pyridyl-functionalized chiral BINOL linkers. By reacting with CdCl₂ under mild conditions, a highly porous 3D framework with large chiral channels of $\sim 16 \times 18 \text{ Å}^2$ crosssection along the a-axis was obtained. In particular, this framework contains plenty of accessible chiral dihydroxy groups that can further react with Ti-(O'Pr)₄, in a post-synthetic manner, to afford Lewis acidic (BINOLate)Ti(O'Pr)₂ species for catalytic addition of ZnEt₂ to aromatic aldehydes. High enantioselectivity (up to 93% ee) was obtained in the reaction of ZnEt₂ with 1-naphthaldehyde. Additionally, the authors have for the first time, demonstrated that the catalytic reactions mainly take place in the internal cavities of the framework from multiple control experiments with differentsized aldehydes (Figure 35).

In 2014, Lin and co-workers [340] first reported the preparation of a CMOF-based heterogeneous asymmetric catalyst using a dicarboxyl-functionalized chiral BINAP unit as linker and Zr_6 cluster as node. Single-crystal analysis revealed the same cubic framework topology as UiO-66, which contains both octahedral and tetrahedral cages with edges measuring 23 Å. The CMOF was shown to be robust in the subsequent post-metalation with either Rh or Ru species. Remarkably, the metalated CMOF catalysts can give three times higher reactivity as the homogeneous control which

was believed to be the result of site isolation of the active chiral catalyst that can effectively prevent the possible intermolecular catalyst deactivation pathways.

As a gemel scaffold to BINOL, biphenol was also successfully incorporated into CMOFs for asymmetric catalysis. In 2014. Cui and co-workers [341] reported a highly porous CMOF constructed from custom-designed enantiopure biphenol-based tetracarboxylate ligand with Zn₄O clusters by taking advantage of the reticular chemistry principle. The framework consisted of multiple triply stranded cages decorated with pairs of hydroxy groups which are amenable to undergoing post-modification. After exchanging one proton of the dihydroxyl group for Li(I) ions, the resulting CMOF can be an efficient asymmetric catalyst for a variety of cyanohydrins synthesis with almost quantitative yields and up to >99% ee. Compared with the homogeneous analogue, the CMOF catalyst exhibited significantly improved catalytic reactivity and enantioselectivity, especially at a low catalyst/ substrate ratio. It is evident that the direct installation of biphenol units into CMOF may help to stabilize the catalytically active monolithium salt of biphenol, thus avoiding its deactivation to catalytically inactive or less active species of biphenolates/Li in homogeneous reactions (Figure 36).

Following the above work, Cui and co-workers [342] demonstrated that the chemical stability, catalytic reactivity and enantioselectivity of a CMOF catalyst can be systematic engineered by tuning the steric hindrance and electronic effect of chiral ligands. To validate this hypothesis, they rationally designed three chiral biphenol-based ligands with 3,5-bis(trifluoromethyl)-, bisfluoro-, phenyl- and bismethylsubstituents, respectively. After an isoreticular synthetic procedure, three isostructural CMOFs were exclusively prepared as unambiguous indicated by single-crystal and powder X-ray analyses. Their inner pore surfaces are periodically decorated with [Mn₂] units with removable coordinating water molecules, which can act as potential Lewis acid metal sites. Chemical stability evaluation by PXRD and N₂ sorption experiments indicated that the -CF₃ group functionalized CMOF shows improved tolerance to water,

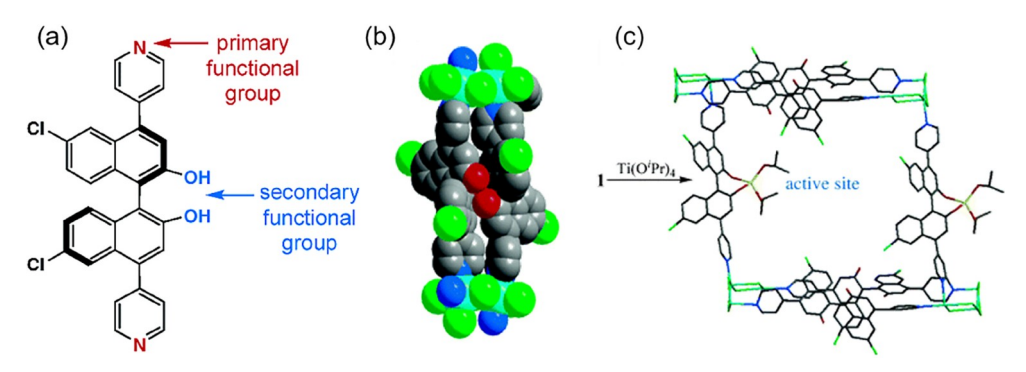


Figure 35 (Color online) (a) The pyridine-functionalized BINOL ligand. (b) Space-filling model of the CMOF structure. (c) Schematic representation of the active (BINOLate)Ti(OⁱPr)₂ catalytic sites in the open channels of CMOF. Reproduced with permission from Ref. [339]. Copyright@2005, American Chemical Society.

Figure 36 (Color online) Schematic demonstration of the assembly and post-modification of CMOF and its application in asymmetric cyanation reaction. Reproduced with permission from Ref. [341]. Copyright@2014, American Chemical Society.

acid and base in comparison with the other two CMOFs. The catalytic activities of the three CMOFs were evaluated for asymmetric F-C alkylations of indoles and pyrrole with a wide range of ketoesters or nitroalkenes under both batch and flow reaction systems. It is clear that the reactivity and enantioselectivity gradually increased in the order CF₃ > F > CH₃, with the highest yield and enantioselectivity of 92% and 99.9%, respectively. Under otherwise identical conditions, the corresponding homogeneous catalyst of metal phosphonate only gave much lower reactivity and enantioselectivity. According to these results, it is reasonable to draw a conclusion that the chiral biphenol unit, metal phosphonate, and the 3,5-bis(trifluoromethyl) functionalized phenyl rings merge to create a chiral microenvironment in the CMOF, which should be responsible for the higher reactivity and enantiodiscrimination ability (Figure 37). This work thus highlights the power of the CMOF platform in the integration of chiral organic scaffold, achiral substituent group, and pore environment in a highly synergistic way.

Chiral metallosalen ligands are naturally excellent organometallic catalysts because of their chelated structure that

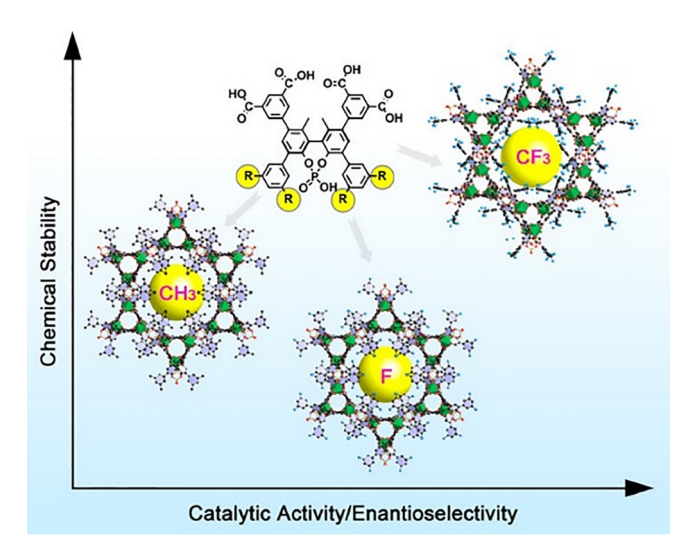


Figure 37 (Color online) Systematic demonstration of the control of chemical stability, catalytic reactivity and enantioselectivity in biphenol-based CMOFs. Reproduced with permission from Ref. [342]. Copyright@2017, American Chemical Society.

can easily bind various metal ions for diverse asymmetric transformations. By adopting the same assembly approach, a series of CMOFs based on chiral metallosalen units have been designed and synthesized mainly by Lin and Cui groups, which led to a new generation of heterogeneous catalysts that are capable of catalyzing more value-added chemical reactions. Cui and co-workers [343] reported the facile synthesis of a CMOF comprised of a Co-salen unit and tetracadmium cluster. With hydrolytic kinetic resolution of epoxides as model reactions, they found that all the catalytic reactions proceeded in good conversions (54%-57%) and good to excellent enantioselectivities (87%-99.5%) regardless of the substituents in benzyloxy epoxide derivatives. X-ray crystal analysis revealed that the framework catalyst may most likely bring Co(salen) units into an appropriate spatial orientation and close proximity to active H₂O and epoxide by two Co(salen) sites separately, thus enhancing the bimetallic cooperative interactions (Figure 38).

Following this strategy, Cui et al. continued their journey in the exploration of other metallosalen-based CMOF catalysts, for example, Ti(salan) [344], Fe(salen) [345], VO(salen) [346], Cr(salen) [347], and Cu(salen) [348]. Thanks to the site-isolation and confinement effect, it was shown that the installation of these chiral metallocatalysts into robust CMOFs would generally boost both the stability and enantioselectivity in a broad of asymmetric reactions. More than that, the diversity of M(salen) building blocks has enabled the development of asymmetric sequential and tandem catalysis that is promoted by a combination of at least two catalysts [349]. In many cases, synergistic effects can be observed between the two catalytic reactions that lead to more highly efficient processes compared to the simple sum of the outcomes of individual reactions. However, the development of catalytic asymmetric sequential reactions is still a big challenge because one must incorporate two individual catalysts into a single system with good compatibility, which turns out to be relatively difficult in homogeneous systems owing to the possible intermolecular catalyst deactivation pathways.

In 2017, Cui *et al.* [350] reported the modular synthesis of an isostructural family of 2-fold interpenetrated multivariate

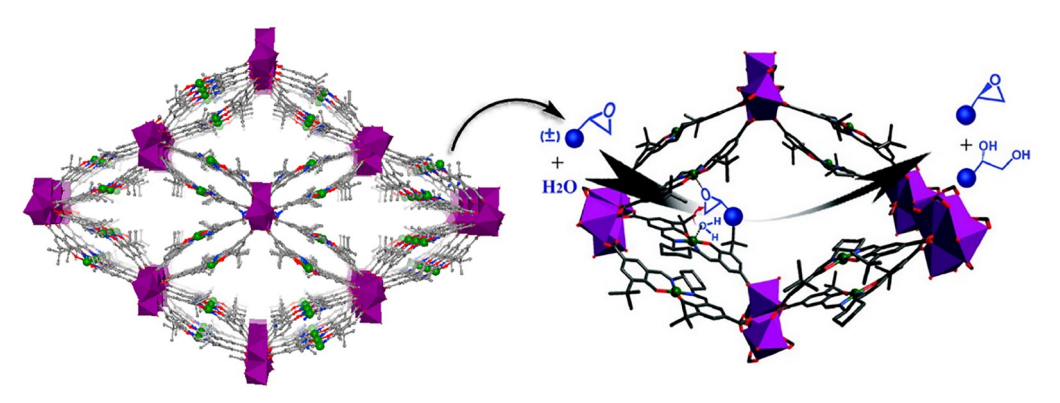


Figure 38 (Color online) 3D structure of Co-salen-based CMOF and the bimetallic cooperative catalysis. Reproduced with permission from Ref. [343]. Copyright@2012, American Chemical Society.

CMOFs with strategically placed multiple and cooperative metallosalen catalysts for a variety of asymmetric sequential alkene epoxidation/epoxide ring-opening reactions. By controlled incorporation of one, two, or three different enantiopure metallosalen derived linkers into one single pcu framework, they realized the controllable syntheses of five binary and two ternary MTV-MOFs. The superior performance of both conversions and enantioselectivities over the homogeneous counterparts as well as the mixtures of binary MTV-MOFs indicated that the ternary framework was not a simple addition of two binary ones. From a structural point of view, the 2-fold interpenetration of the framework rendered the metallosalen units into close proximity that allowed bimetallic cooperative activation, leading to enhanced catalytic efficiency and enantiodiscrimination ability over the sum of the individual parts. This work has provided a brand-new perspective that manipulation of chiral molecular catalysts in MTV-MOFs can create a special cooperative effect and systematically control the reactivity and selectivity of designed sequential reactions (Figure 39).

Readily obtainable metal-free chiral organocatalysts, especially Brønsted acid catalysts, have emerged as a powerful class of catalysts that is complementary to metal- and enzyme-catalyzed transformations. This type of organocatalyst shows prominent catalytic activity towards the formation of C-C and C-X (X = heteroatom) bonds. Systematically tuning the pore size and environment around the catalytically active phosphoric acid sites may generate new heterogeneous Brønsted acid catalysts with high activity and selectivity. In this regard, Liu et al. [351] reported the synthesis of three structurally different chiral porous In-MOFs constructed from three enantiopure biphenol-phosphoric acid-based linkers. The three CMOFs all have large cavities that can be utilized to accommodate reaction substrates. Asymmetric condensation/amine addition and imine reduction were selected as model reactions to systematically evaluate the structure-property relationships. Detailed catalytic results clearly indicated that the enantioselectivities can be effectively tuned by varying the substituents at linkers, demonstrating the important role of the bulky anthracenyl groups in achieving high selectivity.

To gain chemically more robust Brønsted acidic CMOF catalysts for challenging asymmetric transformations, Liu and co-workers [352] designed a rigid spirocyclic carboxylate linker that possesses a geometrically different backbone. They conceptually illustrated a ligand design strategy for directly installing chiral phosphoric acid catalysts into highly robust Zr-MOFs without disturbing the catalytically active sites. Under such guidance, they not only achieved a novel framework topology termed as **sjt**, but also for the first time observed an apparent acidity enhancement of CMOFs than the non-immobilized molecular phosphoric acid. The two CMOFs decorated with strong Brønsted acidic phosphoric acid groups were shown to be excellent catalysts in a broad of asymmetric transformations including three-component tandem reactions (Figure 40).

Enantiocontrol of catalytic products can be one of the hardest problems in the domain of both homo- and heterogeneous catalysis. The increasing demand for enantiopure compounds has propelled the rapid development of CMOFbased asymmetric catalysis by virtue of their enzyme-like confined spaces. CMOF catalyst, as a very promising and rising subclass of heterogeneous solid catalysts, may provide unprecedented opportunities to elucidate the mechanism of asymmetric catalysis by allowing the structural characterization of key intermediates with in-situ crystallography or time-resolved X-ray diffraction techniques. In most cases, CMOFs can lead to ee values and even catalytic rates not only comparable to but also surpassing the homogeneous counterparts because of the confinement effects and spatial hindrances that a homogeneous catalyst could not offer. For instance, MOF platforms could stabilize highly active catalytic centers by network protection and site isolation, and efficiently facilitate bimolecular deactivation pathways through precise spatial arrangement. Moreover, the rational design and precise incorporation of two independent cata-

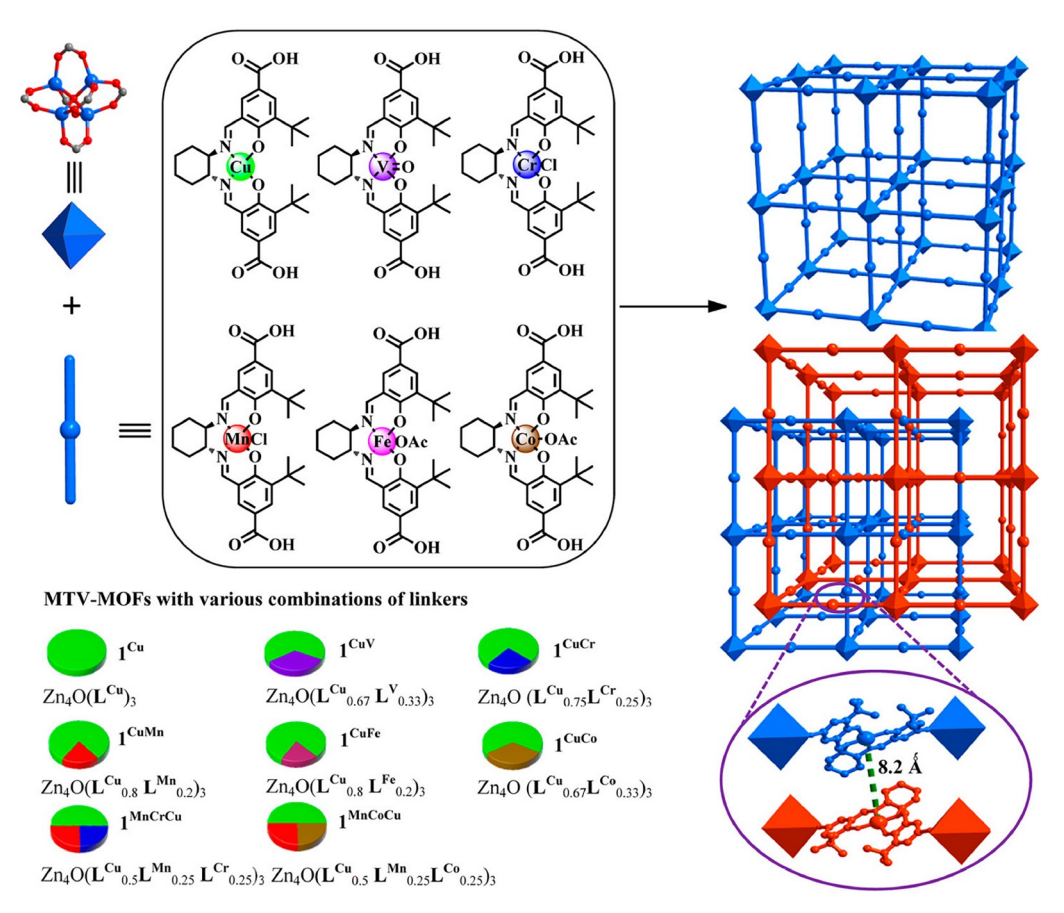


Figure 39 (Color online) Construction of multivariate CMOFs with multiple metallosalen catalysts. Reproduced with permission from Ref. [350]. Copyright@2017, American Chemical Society.

lytic centers to work in a cooperative or sequential manner could lead to cooperative or tandem catalytic systems which are hardly accessible in homogeneous systems. The accessibility of the active sites, which depends on the shape and size of the window and cavity in the CMOFs, is proved to be crucial for the activity and selectivity of the final catalyst. Nano-meter-sized pores are ideal to access the catalytic centres of the framework, and to achieve strong multi-directional interactions between substrates and the chiral environment of the cavities. Future research endeavors should still be concentrated on the sophisticated design and control of the chiral microenvironments as well as inner surfaces of CMOFs, with the aim of targeting task-specific CMOF catalysts for broad-scope organic transformations.

6.3 Catalytic biomass conversion

Biomass is capturing increasing research attention for its great potential as a renewable alternative source of fuels and chemicals to non-renewable fossil feedstocks such as petroleum, coal and natural gas, etc. In recent decades, biomass has become one of the most promising candidates in this respect in which cellulose, hemicellulose and lignin can be converted to platform chemicals and transformed into a large

range of useful compounds through heterogeneous catalytic reactions. In this regard, homogeneous catalysts often suffer from the use of toxic metals, strong corrosivity, severe pollution and poor recyclability, making it in some cases more complicated to meet the increasingly strict environmental regulations. Therefore, developing efficient and durable solid catalysts with active sites that can promote transformation and drive selectivity is highly needed. Additionally, the tunable composition, tailorable particle morphology and porous architecture would further endow heterogeneous catalysts with versatile physicochemical parameters that offer high potential for the design of efficient catalytic processes. With the rapid development of heterogeneous catalysts, a vast range of different types of catalysts with novel topologies and attractive catalytic performances have been designed and fabricated for biomass transformation, including MOFs, carbon-based materials, zeolites and silicates, metal-oxides, layered double hydroxides (LDHs) and polymers. Among these, MOFs are distinctive because of the following traits: (1) uniformly dispersed catalytic sites on the pore surface, which contribute to reactivity and selectivity; (2) large surface area and appropriate hydrophilic and hydrophobic pore nature to facilitate the recognition and transportation of reactant and product molecules; (3) multi-

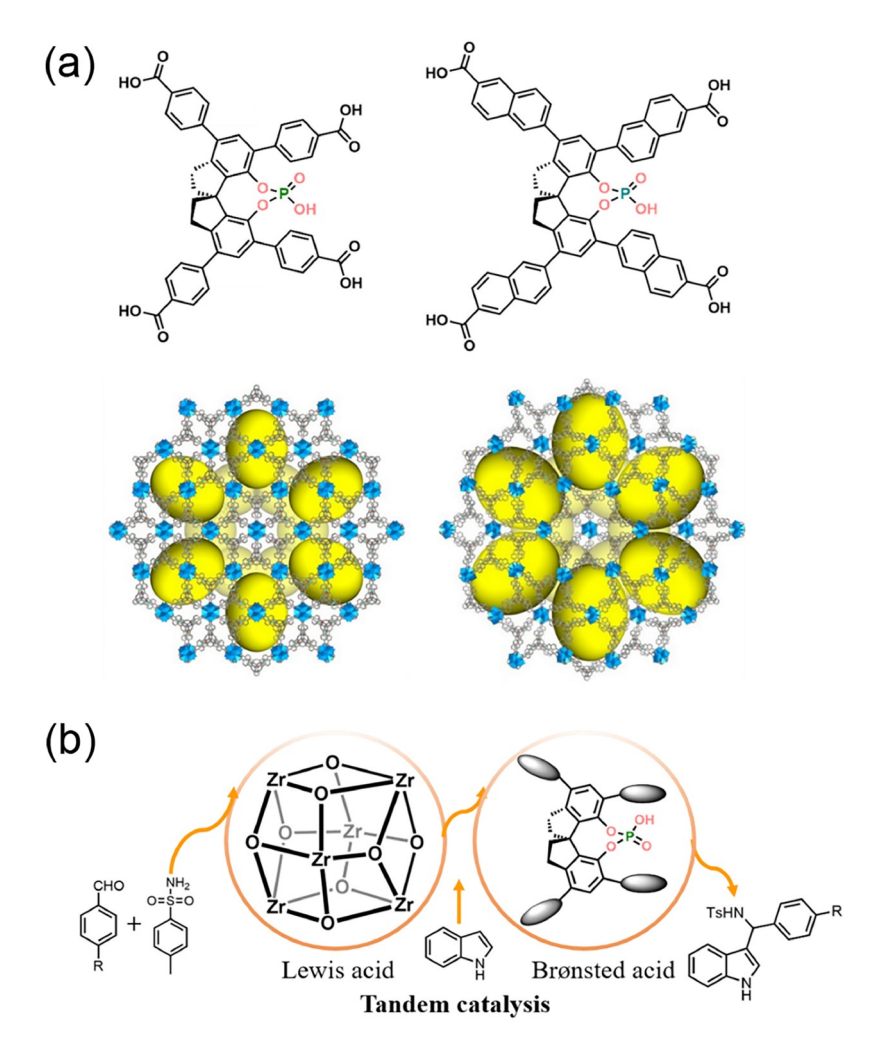


Figure 40 (Color online) (a) Schematic representation of the assembly process and 3D crystal structures CMOFs. (b) Asymmetric tandem catalysis in three-component Friedel-Crafts reactions. Reproduced with permission from Ref. [352]. Copyright@2019, American Chemical Society.

functional and tunable microenvironment to realize synergistic catalysis; and (4) simple separation and recovery for long-term usage. The presence of OMSs or custom-designed protons in MOF frameworks can act as strong Lewis or Brønsted acidic sites to promote a wide range of biomass conversion reactions [353].

MOFs entered the stage of biomass valorization with the first attempt on cellulose hydrolysis over a MOF-based acidic catalyst reported by Kitagawa and co-workers [354]. Afterwards, with the rapid development of synthetic strategies and characterization techniques, a majority of MOF-based catalysts were designed, fabricated and applied in biomass transformations. Hydrolysis of biomass to saccharides or platform chemicals is one of the important industrial reactions requiring acid catalysts. In this context, MIL-53(Al) was reported as a heterogeneous solid catalyst for the direct conversion of carboxymethyl cellulose to 5-hydroxymethyl-furaldehyde (5-HMF) in the aqueous phase, giving 40.3% yield of 5-HMF in water at 200 °C after 4 h [355]. In spite of the lack of coordinatively unsaturated po-

sitions around Al³⁺ in the ideal MIL-53(Al) structure, NH₃ temperature-programmed desorption (NH₃-TPD) analysis showed the presence of Brønsted acidic sites which are responsible for promoting the reaction and are probably associated with structural defects. MIL-53(Al) can be easily recycled and showed similar activity for the subsequent three cycles without much decrease in its activity. PXRD measurements of reused MIL-53(Al) showed almost no changes, indicating its structural robustness. Moreover, the superior activity of MIL-53(Al) compared to MIL-101(Cr) may be due to the presence of Brønsted acid sites in MIL-53(Al) responsible for the hydrolysis, while such active sites are lacking in MIL-101(Cr) (Figure 41). This work illustrates the importance of lattice imperfections in MOF crystals for biomass conversion.

Besides the hydrolysis of cellulosic feedstocks, the conversion of sugars to platform molecules is one of the key processes in biomass transformation. In this context, four isostructural catalytic materials (MOF-74) with different metal centers (Co, Ni, Mg, Zn) clearly showed the strong

Figure 41 (Color online) A possible reaction pathway for the hydrolysis of carboxymethyl cellulose over MIL-53(Al) catalyst. Reproduced with permission from Ref. [355]. Copyright@2015, Elsevier.

impact of the Lewis acidic metal ions in the sugar conversion into methyl lactate [356]. The yields of methyl lactate were 16%, 19% and 20% while using MOF-74(Ni), MOF-74(Zn) and MOF-74(Co), respectively. The MOF-74(Mg) material exhibited the best catalytic activity and a methyl lactate (as the main product) yield of 47% was obtained from sucrose. MOF-74(Mg) was also most active for the retro-aldol reaction of fructose to methyl lactate as a main product with a yield of 37%. Simultaneously, the conversion rate of glucose was higher and a slightly higher yield of side products like methyl glycolate and glycol aldehyde dimethyl acetal were obtained from glucose. As for disaccharides, except sucrose, lower yields of methyl lactate (19% for both lactose and maltose) were achieved. This may be explained by the resistance of these disaccharides to methanolysis under the reaction conditions. The reason for the enhanced catalytic performance of MOF-74(Mg) can be ascribed to the stronger Lewis acid sites of Mg²⁺ in the structure.

Zr-based MOF materials have been proven as efficient catalysts for biomass conversion, due to their exceptionally strong Lewis acidity [357]. A typical example of the design of catalytic MOF materials using Zr⁴⁺ ions as building blocks

with strong Lewis acidity is UiO-66 or NH₂-UiO-66, which are active structures for biomass valorization catalysis [358]. Both matrices show activity in the esterification of levulinic acid with EtOH, *n*-BuOH and long-chain fatty alcohols. This process leads to biomass-derived alkyl levulinates of industrial importance (Figure 42). Their catalytic efficiency is comparable (and in some cases superior) to the heterogeneous acid catalysts previously reported in the literature, such as supported heteropolyacids and zeolites.

UiO-66 is built by a 12-connected Zr₆ node which typically shows relatively weak and inaccessible Lewis acidity, while MOF-808 is based on a 6-connected Zr₆ node with coordinatively unsaturated centers available for catalytic activity [55]. The catalytic performance of MOF-808 was examined in the Meerwein-Ponndorf-Verley (MPV) reduction of furfural [359]. The highest activity under the optimized reaction conditions was achieved with MOF-808 based on Hf and Zr. In particular, Hf-MOF-808 showed two-fold catalytic reactivity enhancement with respect to Zr-MOF-808, clearly demonstrating the key role of Lewis acidity in facilitating catalysis. Later, the activity of Hf-MOF-808 was tested in the MPV reduction of ethyl levuli-

nate to g-valerolactone (GVL), reaching 94% yield of the desired product without the formation of by-products. Hf-MOF-808 was used for five cycles with only a slight decrease in activity.

Compared to the relatively comprehensive works that have been utilizing the Lewis acidity of MOFs, exploring Brønsted acidity of MOF materials is more challenging and remains less explored, mainly because of the weakened framework stability caused by the introduction of Brønsted acidity typically through sulfonic acid groups. One of the pioneering works is the preparation of the mesoporous SO₃ H-MIL-101(Cr) framework containing both Lewis acidic Cr³⁺ ions and Brønsted acid -SO₃H sites. Thanks to these strong Brønsted acid sites, SO₃H-MIL-101(Cr) showed high activity in cellulose hydrolysis into mono- and disaccharides, such as glucose, xylose and cellobiose and demonstrated high durability [360,361]. The bifunctional SO₃H-MIL-101(Cr) was extensively studied in challenging and practically demanding processes- cascade reactions of glucose as a platform chemical to 5-HMF transformation (Figure 43). This process involves isomerization over Lewis acid sites followed by the dehydration to 5-HMF over Brønsted acid sites.

Catalytic biomass valorization is one of the most fasci-

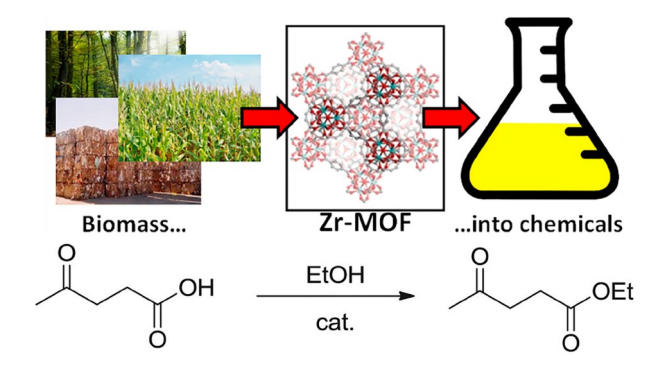


Figure 42 (Color online) Esterification of levulinic acid with ethanol over Zr-containing UiO-66-type MOFs. Reproduced with permission from Ref. [358]. Copyright@2015, Elsevier.



Figure 43 (Color online) Transformations of (a) fructose and (b) glucose into 5-HMF and (c) furfural alcohol into ethyl levulinate over SO₃H-MIL-101. Reproduced with permission from Ref. [360]. Copyright@2016, American Institute of Chemical Engineers.

nating potential applications of MOF materials. This area provides a huge field of research activity relevant to various tuned MOF structures for cascade processes of biomass processes. The morphology, porosity and composition of the MOF catalysts can work synergistically to control mass diffusion, molecule sorption and catalytic cycles, thereby having a significant impact on the catalytic performance. Therefore, MOF materials provide an optimal platform to embed both Lewis and Brønsted acid sites in a single matrix. The ease of modification of the microenvironment has greatly facilitated their catalytic performance optimization and also helped to improve their hydrothermal stability and reusability.

6.4 CO₂ fixation

Humankind is highly dependent on fossil fuels; however, consumption of fossil fuels releases massive amount of greenhouse gas CO₂, which is believed to contribute adversely to climate change. Currently, carbon capture and storage/sequestration (CCS) is one of the most encouraging strategies being implemented to reduce carbon emissions [362]. As an important C1 feedstock, CO₂ holds the potential to be highly economical in both a chemical and a financial sense. In this context, CO2 can react with different substrates to result in fine chemicals through new C-X bond formation, including C-H, C-C, C-N, and C-O bonds [363,364]. In particular, the highly atom-economical catalytic cycloaddition of CO2 with epoxides to afford cyclic organic carbonates, which have been widely used in industrial applications. Therefore, extensive research has been focused on the development of heterogeneous catalysts for such cycloaddition reactions. In this regard, MOFs are promising candidates for promoting catalytic CO₂ fixation reactions as they are a class of highly tunable, crystalline, porous, and functional materials with unique intrinsic properties including large surface area, accessible channels, and permanent porosity. Besides, MOFs can possess large densities of OMSs acting as Lewis acid sites to facilitate catalytic CO₂ fixation reactions [365].

The mechanism for the cycloaddition of CO₂ to epoxides typically involves an acid catalyst (*e.g.*, a metal ion) that coordinates to the epoxide thereby activating it toward nucleophilic attack by the co-catalyst (typically a tetraalkylammonium halide) to form a halo-alkoxide. This halo-alkoxide intermediate can then react with CO₂ through cycloaddition to yield the cyclic carbonate with regeneration of the tetraalkylammonium halide co-catalyst. In this section, we will present the most popular MOFs that show Lewis acidity either at the metal nodes or organic linkers for cycloaddition reactions involving CO₂. In some cases, there are also MOFs in which ligands incorporating a Lewis acid center as well as nodes with OMSs are present, providing

double Lewis acid character to catalyze the cycloaddition reaction.

Guillerm and co-workers [366] reported the highly Lewis acidic Y³⁺-based MOF incorporating a nonanuclear carboxylate cluster in 2014. This cluster served as an 18-connected molecular building block (MBB) for the formation of a unique (3,18)-connected gea net. Further structural analysis clearly revealed its high porosity and accessible Lewis acidic Y³⁺ sites. The gea-MOF-1 was explored as a heterogeneous catalyst for the cycloaddition of CO2 to epoxides. The reactions were performed at 120 °C and 20 bar CO₂ for 6 h in neat epoxide, without extra solvent. The catalyst converted the reaction effectively and smoothly, giving rise to an 88% yield of the propylene oxide product. However, under otherwise similar reaction conditions, another heterogeneous control of Y₂O₃/ⁿBu₄NBr (TBAB) showed apparently lower activity, demonstrating the highly accessible Lewis acid (Y³⁺) sites of gea-MOF-1 are the key to its superior catalytic activity (Figure 44).

In 2016, Zou and co-workers [367] reported a highly porous MOF, termed 1-Zn, featuring a remarkable BET surface area of 2,969 m² g⁻¹ and accessible Lewis acid sites suitable for catalyzing the cycloaddition reactions. Single crystal structural analysis revealed two types of metal clusters, i.e., the dimeric paddlewheel [Zn₂(COO)₄] and tetrameric ($Zn_4(\mu_4-O)$ (COO_2)₆), that are present in the structure. Interestingly, Cu²⁺ and Co²⁺ ions can be introduced into the dimeric paddlewheel [Zn₂(COO)₄] cluster via SCSC transformation metal ion exchange, which can provide a novel platform to study how the metal (Lewis acidity) affects the catalytic performance in CO₂ cycloaddition reactions. In a typical room temperature reaction with 12 bar CO₂, they achieved yields of propylene carbonate at 99%, 32%, and 50% for 1-Zn, 1-Cu, and 1-Co, respectively. The high catalytic efficiency of 1-Zn for this reaction may be due to the lower energy gap between the highest occupied molecular orbitals (HOMO) of epoxy propane and the lowest unoccupied molecular orbitals (LUMO) of CO2 on the OMSs, and the higher binding energy of CO₂ to the metal centers as supported by molecular dynamic simulations.

Almost at the same period, Farha and co-workers [368] reported an Hf-based MOF, Hf-NU-1000, which is an ex-

cellent catalyst for the cycloaddition reaction of CO₂ to epoxides. The MOF was synthesized via the solvothermal reaction of HfOCl₂·8H₂O and 1,3,6,8-tetrakis(pbenzoic acid) pyrene (H₄TBAPy), giving a yellow microcrystalline product. Hf-NU-1000 has triangular and hexagonal open channels with diameters of 1.4 and 2.9 nm, respectively. The node consists of strongly Lewis acidic Hf₆ clusters that are capped by eight bridging carboxylate-containing linkers. Hf-NU-1000 was able to promote the cycloaddition reaction quantitatively at room temperature under 1 bar CO₂.

MOFs based on hard acid centers like Mg²⁺ are expected to exhibit strong Lewis acidity for efficiently facilitating epoxide activation. In 2012, Cho et al. [369] reported the use of $M_2(DHTP)(H_2O)_2 \cdot 8H_2O$ (M-MOF-74 where M = Co^{2+} or Mg²⁺) in the cycloaddition catalysis. Benefiting from the large pore aperture of the MOF, larger substrates can also enter the pores. The metal nodes are coordinated in a square pyramidal fashion with a removable weakly coordinated water molecule. Both Co- and Mg-MOF-74 were studied as catalysts for the reactions and they show high catalytic activities under 20 bar of CO₂ and 100 °C for 4 h. Impressively, the reaction proceeded smoothly without the co-catalyst of ammonium salt. It is proposed, but not confirmed that the oxygen atoms of the carboxylate linkers act as the co-base. Besides, Co- and Mg-MOF-74 featuring different Lewis acidity showed comparative catalytic performances, implying the importance of MOF topology in directing the catalytic cycle. Indeed, both the Co²⁺ and the Mg²⁺ analogs have very high CO2 affinities, which resulted in a higher local concentration of CO₂, thus increasing catalyst performance.

Another efficient approach to construct MOFs for the CO₂ cycloaddition reactions is to incorporate Lewis acidic sites into the organic linkers. This method can, in some cases, produce double Lewis acidic sites that facilitate a dual activation pathway. Ma and co-workers [370] reported a **nbo** MOF (MMCF-2) constructed by azamacrocycle ligand and Cu(NO₃)₂. The resultant paddlewheel Cu₂ nodes and the *in situ* formed metalated azamacrocycle provide double metal sites of high density that can work synergistically to promote the CO₂ cycloaddition reactions. Interestingly, MMCF-2 showed superior catalytic activity than the isostructural MOF-505 without metalated organic linkers, de-

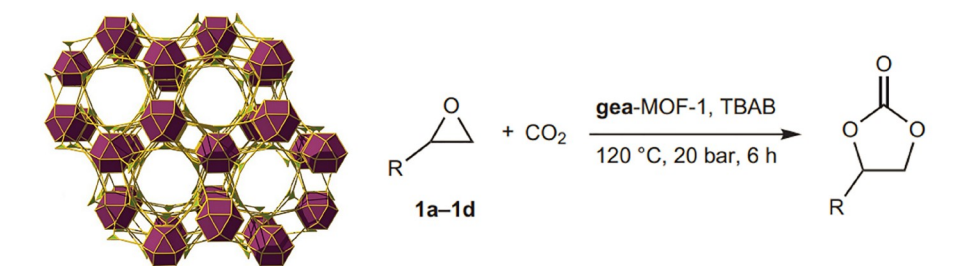


Figure 44 (Color online) 3D topological structure of the gea-MOF-1 and its catalytic synthesis of cyclic carbonates from CO₂ and epoxides. Reproduced with permission from Ref. [366]. Copyright@2014, Springer Nature.

monstrating the critical role of increasing Lewis acid site density (Figure 45).

The catalytic activity enhancement by increasing Lewis acid site density has facilitated a more rational design of metalated organic linkers that could potentially be assembled into MOFs for CO₂ cycloaddition. In this context, metalloporphyrins and metallosalens have also been incorporated into MOF structures and their catalytic activities were also investigated. The metalloporphyrin example was reported in 2013 by Feng et al. [371]. By assembling the metalloporphyrin linker with Zr⁴⁺, they prepared a series of chemically stable Zr-MOFs denoted PCN-224 that carried different transition metal ions, resulting in 3D architectures with a channel size of 19 Å. In particular, PCN-224(Co), which has porphyrin linkers functionalized with Co²⁺ was shown to be highly active for the catalytic cycloaddition reaction of CO₂ with epoxides. Similarly, metallosalen complexes were also used as linkers exemplifying again a double Lewis catalytic effect MOF design (Figure 46). Ren et al. [372], described a Ni(salphen)-based MOF material that features the dicarboxyl-functionalized nickel salphen complex. Single crystal structure analysis revealed two types of Lewis acidic sites of Cd and Ni, which are accessible to epoxide substrates for double Lewis acid activation. The catalytic activity of the MOF was tested under 20 bar CO₂ and 80 °C and the highest yield of 84% was obtained in the presence of ⁿBu₄Br as cocatalyst. In order to explore if the cycloaddition reactions are indeed catalyzed by the synergy between Cd and Ni sites, the control reactions were performed using Ni-H2L and [Cd(bpdc)]_n, respectively. It was found that the yield of the carbonate product was significantly lower compared to the reaction catalyzed by the MOF, which suggested that the Ni²⁺ and Cd²⁺ centers operate synergistically to activate the epoxides.

It is well-established that the co-catalyst of "Bu₄Br provides Lewis basicity for promoting the CO₂ cycloaddition reaction. As a result, various functional groups (*e.g.*, -NH₂ and -NH-) have also been introduced into MOFs acting as Lewis base sites to avoid the use of basic co-catalysts. For example, Lescouet and co-workers [373] illustrated the important role of an amine-functionalized MIL-68(In)-NH₂ for the cycloaddition reaction. The amine-functionalized MIL-68(In)-NH₂ exhibited higher catalytic activity than that of the parent MIL-68(In) in the production of styrene carbonate from styrene oxide and CO₂. The yields were 71% and 39% for MIL-68(In)-NH₂ and MIL-68(In), respectively. The efficiency of the Lewis-acid and Lewis-base pair approach was also validated by that UiO-66-NH₂ showed higher catalytic performance than the UiO-66.

MOF-based catalysts offer an ease of modification that has traditionally been available only for homogeneous catalysts. Taking advantage of this great tunability, one can readily design metal nodes with tunable Lewis acidity and density

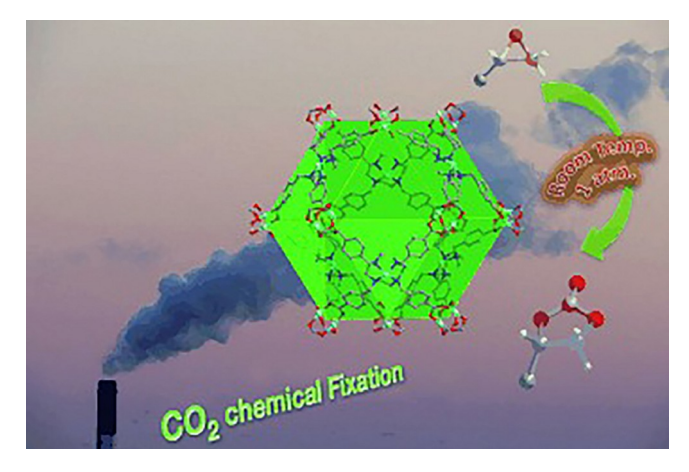


Figure 45 (Color online) The azamacrocycle-based MOF for catalyzing cycloaddition of propylene oxide and CO₂. Reproduced with permission from Ref. [370]. Copyright@2014, Wiley-VCH GmbH.

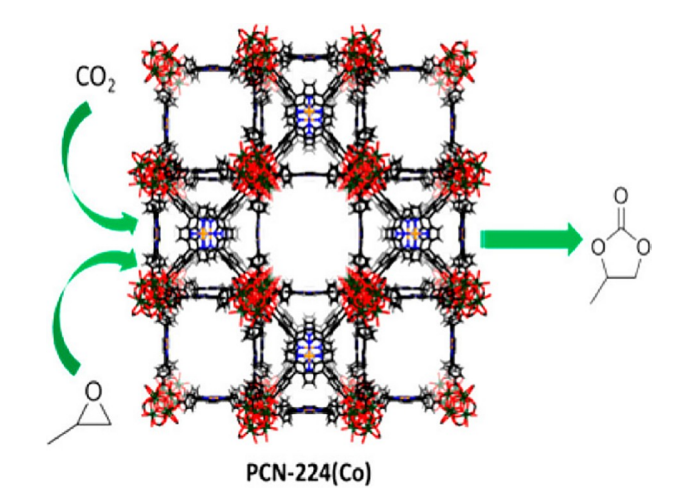


Figure 46 (Color online) The metalloporphyrin-based MOF for catalyzing cycloaddition of propylene oxide and CO₂. Reproduced with permission from Ref. [371]. Copyright@2013, American Chemical Society.

for activating epoxides. Besides, the incorporation of functional groups such as amino groups into the organic linkers may increase the CO₂ affinity and Lewis basicity of a MOF thereby increasing the local concentration of CO₂ near the catalytic sites and facilitating the co-catalyst-free reaction. One of the future CO₂ cycloaddition reactions with epoxides catalyzed by MOFs is expected to focus on the tuning of isosteric heats of adsorption for CO₂, as their CO₂ capture properties can lead to enhanced substrate concentration and enhanced reaction kinetics. On the other hand, optimizing the acid-base properties of the MOF materials by virtue of their confinement effect could have a profound effect on catalyst performance.

7 Photocatalysis

Photocatalysis is an intriguing subject where chemical re-

actions are driven by light [374–377]. MOFs are promising photocatalysts by virtue of their rich structural features and high stability under light irradiation. In MOF-based photocatalysis, pivotal processes such as CO2 reduction reaction (CO₂RR), hydrogen evolution reaction (HER) and various organic transformation reactions are facilitated primarily by photo-induced electrons and holes. The photoexcitation could lead to a transition of electrons from HOMO to LUMO [378]. Upon achieving a charge-separation state, the photogenerated electrons and holes could migrate separately to catalytic centers, engaging with the adsorbed reagents, and thereby initiating the photocatalytic conversions (Figure 47). In general, the HOMO and LUMO of MOF-based photocatalysts are shaped predominantly by the organic linkers and the metal clusters. It is crucial that the LUMO and HOMO energy levels of the MOF should exceed the reduction and oxidation potentials of the intended reduction and oxidation half-reactions, respectively.

7.1 Photocatalytic CO₂ reduction

As mentioned above, converting CO₂ into useful chemicals and fuels is not just regarded as a remedial approach for global warming but also as a transformative opportunity for driving economic growth. Among the myriad of techniques available, photocatalytic CO₂ reduction possesses advantages such as simple catalytic systems, minimal investment, mild reaction conditions, and lower pollution. The carbon atom in CO₂ holds its highest oxidation state of +4, evidenced by the substantial bond energy of its two C=O double bonds (803 kJ mol⁻¹). This high bond energy underscores the elevated energy requisite for cleaving the C=O bond. The large energy gap (13.7 eV) for CO₂ between its HOMO and LUMO underpins its thermodynamic stability. Studies have suggested that the proton-coupled multi-electron transfer pathway can effectively lower the thermodynamic barrier required for the CO₂ reduction reaction [379,380]. Photocatalytic CO₂ reduction is an intricate multielectron transfer process, where different photocatalytic systems can yield a diverse range of reduction products, including C₁ products such as CO, CH₄, HCOOH, and CH₃ OH, as well as C₂ products such as C₂H₆, C₂H₄, and C₂H₅OH (Figure 48) [381,382].

During the construction of MOFs for photocatalysis, organic ligands with conjugated structures or chromophoric groups are typically selected to enhance their visible light absorption capability [383,384]. Porphyrin is a useful ligand by virtue of its innate electronic properties and delocalized π -conjugated systems [385,386]. An exemplary Zr-MOF incorporating porphyrin ligands (PCN-222) exhibited a pronounced capability of photocatalytic CO₂ reduction into formate under visible light irradiation [387]. Compared with porphyrins, metalloporphyrins can offer enhanced light ab-

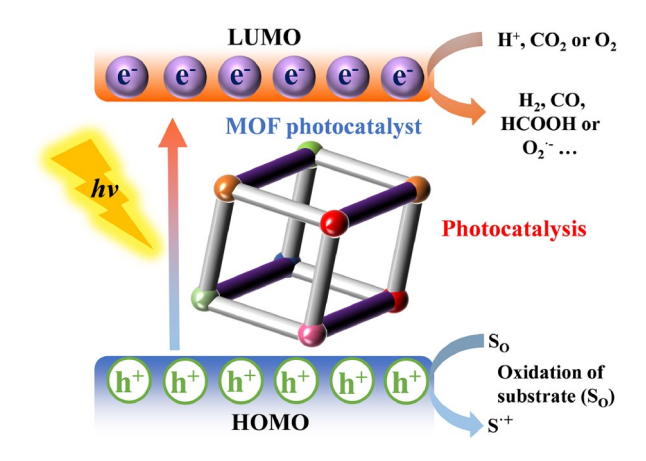


Figure 47 (Color online) Schematic showing the photocatalysis reactions over MOF photocatalysts.

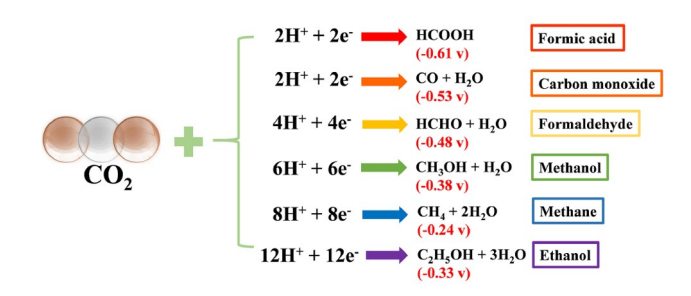


Figure 48 (Color online) Schematic showing the numbers of transferred electrons and protons required for different products of photocatalytic CO₂ reduction.

sorption, efficient electron transfer, and tunable active sites, culminating in improved reaction efficiency and selectivity [388]. Notable examples such as MOF-525-Co [388], NNU-113 [389], and PCN-601 [390] have been identified as efficient photocatalysts. In particular, PCN-601 exhibits a CO₂to-CH₄ conversion rate of 10.1 µmol g⁻¹ h⁻¹ when subjected to visible light and achieves an apparent quantum vield (AQY) of 2.18% under simulated solar irradiation [390]. Apart from porphyrinic structures, MOFs derived from the self-assembly of conjugated ligands such as anthracenyl and perylenyl with metals also exhibit commendable photocatalytic activity. Specifically, an anthracene-based zirconium MOF (NNU-28) has been employed as a photocatalyst for CO₂ reduction. Investigations revealed that NNU-28 not only demonstrates efficient CO2 adsorption capabilities but also has a broad absorption range in the visible light spectrum. NNU-28 could photocatalyze CO2-to-HCOOH conversion with a rate of $52.8 \,\mu\text{mol g}^{-1} \,h^{-1}$ [391]. Both bipyridine ruthenium (bpy-Ru) and phenylpyridine ruthenium are frequently employed as photosensitizers [392]. Zhang et al. [393] integrated bpydc-Cu/-Co sites and bpy-Ru into UiO-67-type MOFs through the coordination strategy. The Eu-bpy-Ru-CuCl₂ exhibited a formate production rate of 3,040 µmol g⁻¹ with 99.7% selectivity within 10 h, 9.8-fold higher than the corresponding homogeneous systems (Figure 49).

Functionalization of organic ligands could enhance the light absorption capabilities, increase the CO2 absorption capacity, and enrich the active sites of MOF-based photocatalysts. Notable examples are biomimetic MOFs (AD-MOF-1 and AD-MOF-2) containing -NH2 groups, which could convert CO2 to HCOOH with rates of 179.0 and 443.2 μmol g⁻¹ h⁻¹, respectively [394]. Lu et al. [395] fabricated a dual-atom Co₂-MOF (Co₂-MOF(-NH₂)) that exhibited a CO production rate of 2.44 mmol $g_{Co}^{-1} h^{-1}$, outperforming its mononuclear counterpart Co-MOF(-NH₂) $(0.23 \text{ mmol g}_{\text{Co}}^{-1} \text{ h}^{-1})$ by 10.5 times, which underscores the exceptional catalytic capabilities of the dual-atom catalyst. Zhong et al. [396] introduced flexible dual-metal-site pairs into MOF-808 by modifying ethylenediaminetetraacetic acid, and the resulting catalyst exhibits a dynamic selfadaptive behavior to fit C1 intermediates, facilitating CO₂to-CH₄ photoreduction. The modified photocatalyst MOF-808-CuNi gives an impressive CH₄ production rate of $158.7 \, \mu \text{mol g}^{-1} \, \text{h}^{-1}$.

For MOFs that inherently lack the capacity for light absorption, the incorporation of photosensitizers becomes crucial for photocatalytic CO₂ reduction. A cobalt-containing zeolitic imidazolate, Co-ZIF-9, has been employed as a robust catalyst to reduce CO₂ to CO by cooperating with a Ru-based photosensitizer. Under mild reaction conditions, the catalytic turnover number of Co-ZIF-9 reached approximately 450 within 2.5 h, and retained its intrinsic reactivity during prolonged operation [397]. Lu et al. [398] crafted bulk Ni-MOF, Ni-MOL-100 and Ni-MOL-010 with crystal engineering technique. Ni-MOL-100 and Ni-MOL-010 exhibit higher surface areas than that of bulk Ni-MOF, thereby exposing more active sites and displaying enhanced catalytic activity for the reduction of CO₂ to CO. Notably, the catalytic activity of Ni-MOL-100 is over 2-times higher than that of Ni-MOL-101. DFT calculation indicates that on the (100) facet, cooperative catalysis can occur between adjacent Ni centers, which can lower the reaction-free energy of the rate-determining step, thereby enhancing its photocatalytic performance. Apart from serving as catalysts, MOFs can also be used independently as photosensitizers. Sun et al. [399] employed ultra-thin Zn-TCPP nanosheets as photosensitizers, with ZIF-67 or [Co₂(OH)L](ClO₄)₃ complex as catalysts, and triethanolamine (TEOA) as the sacrificial electron donor. Under visible light irradiation, this system can reduce CO₂ to CO, with a TON of 68.7.

The scope of MOF-based composite catalysts has expanded through the integration of diverse components, including molecular catalysts [400], semiconductors [401], and enzymes [402]. One such photocatalyst reported by Huang *et al.* [400] involves a copper porphyrinic triazine framework

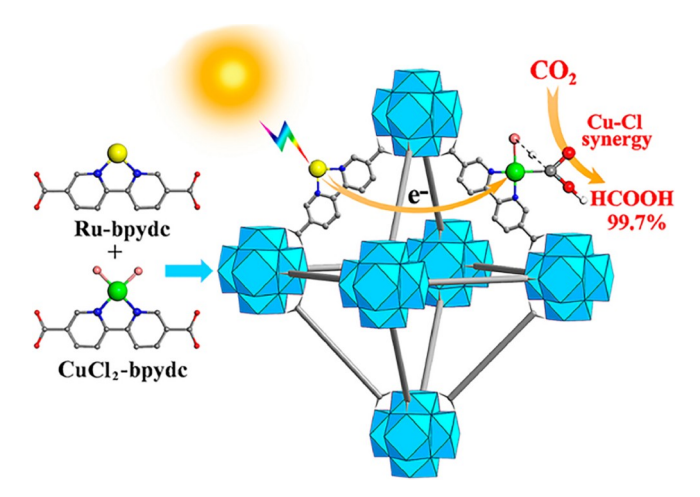


Figure 49 (Color online) Schematic representation of the photocatalytic CO₂ reduction over Eu-bpy-Ru-Cl₂. Reproduced with permission from Ref. [393]. Copyright@2021, American Chemical Society.

[PTF(Cu)], its catalytic performance can be enhanced by incorporating rhenium-(I) bipyridine fac-[Re¹(bpy)(CO)₃Cl] (Re-bpy). Utilizing the tandem catalysis system of Re-bpy/ PTF(Cu), the conversion of CO₂ to ethylene was achieved with a rate of 73.2 µmol g⁻¹ h⁻¹ under visible light irradiation. This efficient process includes the generation of CO intermediate at the Re-bpy sites, which is subsequently adsorbed by the Cu single sites within PTF(Cu) (Figure 50). This proximity facilitates a synergistic C-C coupling reaction, producing ethylene, and thus boosting the photocatalytic efficiency of the MOF. Deng et al. [403] created "molecular compartments" within MOF crystals, specifically, by embedding TiO₂ within the pores of MIL-101 and its derivatives. Remarkably, the composite containing 42% TiO₂ in MIL-101-Cr-NO₂ exhibited an apparent quantum efficiency of 11.3% at 350 nm. This configuration achieved the highest CO₂ conversion efficiency of 12 mmol g⁻¹ h⁻¹. Other notable examples include composite catalysts such as CsPbBr₃@ZIF-67 [404], CsPbBr₃@ZIF-8 [404] and MAPbI₃@PCN-221(Fe_{0.2}) [405]. These composites are not just adept at reducing CO₂ to CH₄ and CO, but also significantly improve the stability of perovskites in water-containing solution.

In addition to the aforementioned composite catalysts, MOF-derived catalysts have also garnered attention for their unique advantages. These catalysts typically exhibit well-dispersed active sites, high stability and increased surface area. In 2021, Lu *et al.* [406] used bulk Co-MOF as a precursor and prepared g-C₃N₄-based Co(II) SAC via a two-step method. Under visible light irradiation, the SAC displayed a CO production rate of 464.1 µmol g⁻¹ h⁻¹, 3 and 222 times higher than those of bulk Co-MOF and CoCl₂, respectively. The exceptional performance of this catalyst is attributed to the uniformly dispersed Co(II) sites, which aid in CO₂ adsorption and activation. They also prepared a 25-

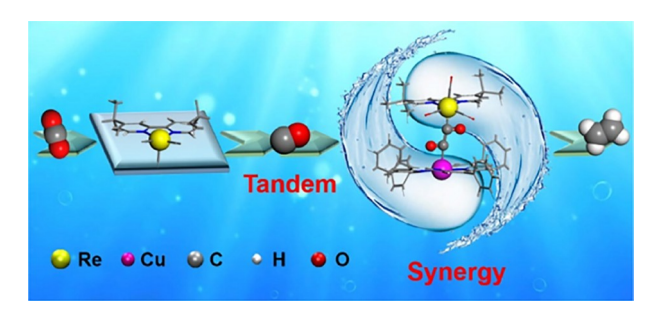


Figure 50 (Color online) Schematic representation of the photocatalytic CO₂ to ethylene by PTF(Cu). Reproduced with permission from Ref. [400]. Copyright@2023, American Chemical Society.

Co- C_3N_4 catalyst using Co-MOF and urea as raw materials. The 25-Co- C_3N_4 achieved a CO production rate of 394.4 µmol g⁻¹ h⁻¹ in CO₂ reduction, 80 times higher than that for g- C_3N_4 [407].

7.2 Photocatalytic hydrogen production

Photocatalytic hydrogen production features the advantages of directly converting solar energy into a clean and renewable fuel, eliminating the need for external input of electricity [408–411]. In the photocatalytic water splitting system for producing hydrogen from pure water, there are generally two recognized reaction pathways: the Volmer-Heyrovsky pathway and the Volmer-Tafel pathway, both commencing with the Volmer step. Initially, a water molecule adsorbs onto the surface of the catalyst, and dissociates into OH and a proton (H⁺) under the oxidation of photo-generated holes (h⁺) (Eq. (1)). Subsequently, H⁺ accepts a photoelectron (e⁻) from the catalyst, forming an adsorbed hydrogen atom (H*) at the active site (Eq. (2)). The subsequent reactions are distinguished as either the Heyrovsky step or the Tafel step. In the Heyrovsky step, the H* interacts with an H⁺ or a water molecule, and upon reduction by an e, forms a hydrogen molecule (Eqs. (3) and (4)). In the Tafel step, two adjacent H* combine upon collision to form an adsorbed hydrogen molecule (Eq. (5)), which then desorbs. The photocatalytic hydrogen production pathway comprises three stages: the initial state $(H^+ + e^-)$, the intermediate (H^*) , and the final product in the desorbed state (H₂).

$$H_2O + h^+ \rightarrow H^+ + \bullet OH$$
 (1)

$$H^{+} + e^{-} + * \rightarrow H^{*}$$
 (2)

$$H^* + e^- + H_2O \rightarrow H_2 + OH^- + *$$
 (3)

$$H^* + e^- + H^+ \rightarrow H_2 \tag{4}$$

$$H^* + H^* \rightarrow H_2 + 2^*$$
 (5)

MOFs have emerged as multifunctional semiconductor photocatalysts, often acting as substrates to stabilize highly dispersed, specialized photocatalysts tailored for H₂ production [412]. Numerous approaches have been explored to enhance the photocatalytic efficiency of MOFs for H₂ generation. A fundamental factor for efficient light utilization in

MOFs is regulating the photosensitizers and nodes of metal. Shi et al. [413] incorporated Eosin Y photosensitizer into UiO-66-NH₂ to photocatalyze HER, and the hydrogen production rate reached 2,760 µmol h⁻¹, benefiting from the facile charge transfer from Eosin Y to MOFs, thereby extending the photo-responsive range of the MOF into the visible light spectrum. The incorporated -SCH₃ group in MOF can improve the visible light absorption ability by donating electrons to the aromatic linking unit. The resulting MIL-125-(SCH₃)₂ derivative displays high activity for photocatalytic H₂ generation, achieving a production rate up to 3,814 mmol g⁻¹ h⁻¹ with TEOA as sacrificial reagent and Pt as co-catalyst (Figure 51) [414]. Another notable contribution came from a Cu(II)-based MOF electrodeposited on nickel foam (NF), achieving an impressive production rate of 24,400 mmol g⁻¹ h⁻¹ in photocatalytic H₂ generation [415].

Incorporating metallized photosensitizers is an innovative approach to promoting the HER over MOFs. For instance, an In-based MOF (STC-8) with TCPP ligands has demonstrated its efficacy in photocatalytic water splitting [416]. USTC-8(In) displays a photocatalytic activity of 341.3 µmol g⁻¹ h⁻¹ using Pt nanoparticles as a co-catalyst under visible-light irradiation, 18-37 times higher than those of other USTC-8(M) (M = Co, Cu, Ni). In another notable endeavor, the photosensitizer RuN₃, when paired with the Co-based ZIF-67 MOF, showcased efficient photocatalytic H₂ production [417]. This synergy culminated in an electron transfer from the activated RuN₃ to ZIF-67 at an impressive efficiency of 86.9%. In addition, a self-sensitized Cu₂I₂-based MOF, featuring a narrow 2 eV bandgap, has been identified for its potential in photocatalytic H₂ production [418]. Remarkably, it registered a H₂ production rate of 7.09 mmol g⁻¹ h⁻ without necessitating an external co-catalyst. Within this MOF, Cu₂I₂ clusters play a dual role: acting as electron donors to expedite the formation of copper(I) hydride and serving as active redox sites. The proposed mechanism demonstrates that Cu₂I₂ clusters of Cu-I-bpy serve as photoelectron generators to accelerate the copper(I) hydride interaction, providing redox reaction sites for hydrogen evolution (Figure 52).

Multi-metal MOFs exhibit advantages over their single-metal counterparts. Their compositions allow for a broader selection of chromophores, on account of the diverse metal ions and organic ligands present. These MOFs also demonstrate superior properties such as a more refined band gap, superior charge separation efficiency, and extended charge carrier lifetime. A prominent example is the Ru-Eu MOF reported for photocatalytic H₂ production. It reached a H₂ generation rate of 4,373 μmol g⁻¹ h⁻¹ [419]. In another pioneering work, the integration of Ce⁴⁺ metal ions into Zr-based UiO-67 was investigated for its potential in photocatalytic H₂ generation. The ligand bpdc was partially substituted by bpydc to form the bpydc-Ce complex. Ce⁴⁺ ion

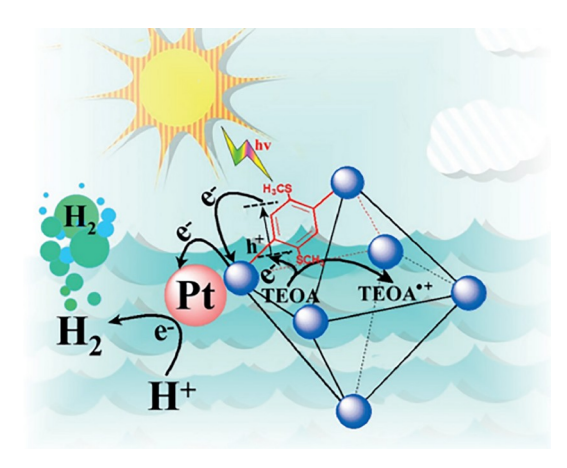


Figure 51 (Color online) Photocatalytic H₂ production mechanism of MIL-125-(SCH₃)₂. Reproduced with permission from Ref. [414]. Copyright@2018, Wiley-VCH GmbH.

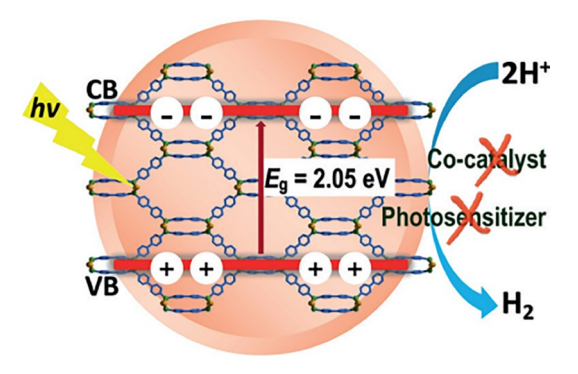


Figure 52 (Color online) Semiconductive Cu(I)-MOF for photocatalytic water splitting into hydrogen without additional photosensitizers and cocatalysts. Reproduced with permission from Ref. [418]. Copyright@2017, Wiley-VCH GmbH.

contains unoccupied low-lying 4f orbitals, which constrains the ligand-metal charge transfer but simultaneously facilitates charge migration from bpdc to bpydc-Ce, leading to improved $\rm H_2$ production photoactivity of MOFs. Moreover, $\rm Ce^{4+}$ ions could also serve as active sites conducive to the reduction reactions essential for $\rm H_2$ generation. Thus, the hydrogen evolution rate observed over UiO-67-Ce was 269.6 μ mol g⁻¹ h⁻¹, more than ten-fold improvement compared with standard UiO-67 under the same experiment conditions [420].

The porous structure and large surface area of MOFs are particularly conducive to the incorporation of photoactive materials [421,422], enhancing the photocatalytic properties of the resulting composites. A seminal study by Wu *et al.* [423] delineated the deposition of uniform noble-metal nanoparticles with small sizes onto MIL-125(Ti). The resulting Pt/MIL-125(Ti) composite exhibited effective photocatalytic activity for H₂ production from water splitting. The total production of H₂ over Pt/MIL-125(Ti) is 38.68 µmol, which is much higher than MIL-125(Ti). Later, Jiang *et al.* [424] innovatively synthesized two other MOFs loaded with Au

and Pt, denoted as Pt@MIL-125/Au and Pt/MIL-125/Au. The constructed Schottky junction, emerging from the integration of Au nanorods (with plasmonic properties) and Pt NPs within the MOFs, promoted a synergistic effect favoring H₂ production. Pt@MIL-125/Au achieved a H₂ generation rate of 1,743.0 µmol g⁻¹ h⁻¹, over 10 times higher than Pt/MIL-125/Au and 170 times than MIL-125/Au. This research team further elucidated a multifaceted MOFs composition as UCNPs-Pt@MOF/Au (UCNPs represent upconversion nanoparticles, denote NaYF₄:Yb, Tm, Er). Intriguingly, UCNPs have the capability of absorbing nearinfrared radiation and subsequently emitting UV or visible photons [425]. At the same time, Au nanoparticles could efficiently harvest visible light, which enables NH₂-UiO-66 to display a propensity to absorb both UV and specific visible light. The integration of these components culminated in UCNPs-Pt@MOF/Au showcased an exceptional catalytic efficiency (280 µmol g⁻¹ h⁻¹) in H₂ evolution from water under UV, visible, and even NIR irradiation, marking a pioneering effort in using MOFs under a trifecta of light irradiation modalities.

Decorating unique semiconductors such as CdS and C₃N₄ onto MOFs for fabricating heterostructured photocatalysts for HER has been proven to be an efficient strategy. CdS NPs have a noteworthy characteristic: their band gap (E_g = 2.4 eV) is sufficiently negative for proton reduction [426]. A pioneering contribution in this domain was made by Yuan et al. [427]. They adeptly orchestrated an in-situ synthesis of CdS nanoparticles on UiO-66 with an octahedral structure. The derived CdS/UiO-66 composite showcased commendable photocatalytic activity for H₂ production. Intriguingly, the H₂ production rate was observed to enhance with an increase in the CdS NPs concentration. This improvement can be attributed to the efficient electron-hole separation realized at the CdS-UiO-66 interface. However, there is a threshold to this enhancement, overloading the system with CdS could curtail the H⁺ production rate—A phenomenon eloquently termed the "coverage effect". Recently, Jiang et al. [428] ventured into synthesizing a CdS-decorated UiO-66 composite for photocatalytic H₂ production from water under visible light irradiation, denoted as a CdS-enhanced UiO-66 composite. The empirical results elucidated that the amount of CdS nanoparticles dispersed on UiO-66 profoundly influences hydrogen production efficiencies. Among the variants, CdS/UiO-66(10) stood out, registering an impressive hydrogen production rate of 1,725 μ mol $g_{CdS}^{-1} h^{-1}$. Furthermore, this catalyst could undergo three recycling rounds without manifesting significant activity loss. Transient absorption spectroscopy revealed that the exemplary H₂ production efficiency originates from the rapid electron transfer from the excited CdS state to UiO-66, facilitating effective charge separation. The g-C₃N₄ has also emerged as a fa-

vorable composite component of MOFs for photocatalytic H₂ evolution. Tang et al. [429] anchored ZIF-8 onto the rodlike g-C₃N₄, yielding a hybrid material ZIF-8/g-C₃N₄ (ZCNx, where x is the mass of $g-C_3N_4$). Designed for the photocatalytic water-splitting under visible light, ZCN400 distinguished itself by manifesting the apex of H2 production rates at 309.5 μ mol L⁻¹ g⁻¹ h⁻¹. This elevated performance is attributed to the harmonized synergy encompassing electronhole separation, efficient charge transfer, and potent redox capability. To further bolster the visible light absorption and electron transfer efficiency of g-C₃N₄, an intriguing approach involves doping sodium (Na). Such doping can modulate the bandgap of g-C₃N₄, enhancing its photocatalytic prowess. For example, a heterojunction composite denoted as Na_{0.02}-C₃N₄/Pt@UiO-66 emerged as a standout, delivering an unphotocatalytic H_2 production 471.4 μ mol g⁻¹ h⁻¹, setting a benchmark that transcends the performance metrics of its contemporaneous counterparts [430].

7.3 Photocatalytic organic transformation

Photocatalysis has been becoming increasingly favored in the field of organic transformations, and this surge in interest can be attributed to several compelling factors [431,432]. First, it allows for unique reactions in the excited state. Second, it generally requires milder reaction conditions, eliminating the need for harmful reagents. Lastly, it promises higher yields while producing fewer byproducts. Among the myriad of applications, photocatalytic oxidation reactions stand out, being pivotal in synthesizing a diverse range of molecules including ketones, aldehydes, sulfoxides, imines, and alcohols (Figure 53). However, a significant challenge lies in the fact that many organic molecules innately absorb visible light weakly. This is where MOFs as photocatalysts come into play. They adeptly capture light, then transfer the photon energy to the organic substrates.

The metal nodes within MOFs can emulate the behavior of catalyst, while the organic linkers function akin to antennas, sensitizing these metal nodes. A case in point is the amine-

functionalized NH₂-MIL-125(Ti) [433], which has been harnessed for the aerobic oxidation of amines, culminating in the formation of imines under visible light. This MOF has shown versatility, effectively transforming a broad range of amines-from benzylamine derivatives to heterocyclic amines-into imines, with yields fluctuating between 41% to 92% upon visible light irradiation. Mechanistic studies revealed that the Ti³⁺ photogenerated in NH₂-MIL125(Ti) operates via an LMCT pathway, reducing O2 to yield the superoxide anion $(\cdot O_2^-)$. This anion subsequently reacts with the carbon-centered radicals derived from the amines to generate the resultant imines. In a similar vein, the Zr-based NH₂-UiO-66 was explored as a visible light photocatalyst for selective aerobic oxidation of various organic compounds [434]. Zhao et al. [435] engineered binuclear Ce-O-Ce MOFs that simulate the function of monooxygenase, achieving a remarkable 97% selectivity for the oxidation of inert C(sp³)-H bonds in alkane. The experimental findings indicate that the Ce-O-Ce units instigate a LMCT, leading to the formation of an oxygen bridge radical. This radical is responsible for abstracting a hydrogen atom from the C(sp³)-H bond, thus creating a carbon-centered radical via a classic hydrogen atom transfer (HAT) mechanism. These carbon-centered radicals then promptly interact with reactive oxygen species (ROS) generated by anthraquinone groups within the framework. This interaction occurs through an EnT process, culminating in the formation of alkyl peroxy radical intermediates. Subsequently, these intermediates are captured by other unsaturated coordinated cerium ions, which promotes their hydrolysis, ultimately leading to the selective generation of carbonyl products (Figure 54).

Wu *et al.* [436] reported a 3D porous MOF utilizing a functional Sn(IV)-porphyrin, which exhibited significant photocatalytic prowess, especially in the oxidation of phenol and sulfides. When Sn^{IV}(OH)₂TPyP was employed as a catalyst under identical conditions, the product yield reached up to 98%. To elevate the efficacy of MOF-based photocatalysis, the implementation of a mix-and-match synthesis strategy is beneficial. Wang *et al.* [437] pioneered this approach, crafting the highly stable Ir(ppy)₂(bpydc)Cl and

Figure 53 Scheme of photocatalytic organic transformation reactions.

Ru(bpy)₂(bpydc)Cl₂ doped UiO-67 (where ppy is 2-phenylpyridine). Both Ru- and Ir-doped MOFs effectively catalyzed the aza-Henry reactions between CH₃NO₂ and phenyl-, pbromophenyl- or p-methoxyphenyl-substituted tetrahydroisoquinoline in 59%–97% conversion yields in reactions carried out with air as the oxidant at 1 mol% catalyst loading under a 26 W fluorescent lamp. Notably, Rucomplex infused MOFs could also initiate the selective aerobic oxidation of thioanisole into methyl phenylsulfoxide, with a 73% yield using methanol as the solvent and O₂ as the oxidant. It was proposed that all the oxidative reactions were mediated by photochemically generated ¹O₂ since all these reactions lack size selectivity.

PSM offers an effective means to enhance the light absorption capacity of ligands in the visible region of MOF photocatalysts, thereby boosting their photocatalytic performance. A notable application of this approach involved modifying NH₂-MIL-125(Ti) with a dye-like moiety, yielding methyl red-MIL-125(Ti) (MR-MIL125(Ti)), which showcased enhanced solar light absorption capabilities [438]. The MR-MIL-125(Ti) displayed a superior photocatalytic efficiency in oxidizing benzyl alcohol to benzaldehyde, with a rate of 87 nmol min⁻¹ g⁻¹, higher than the rate for NH₂-MIL-125(Ti) (78 nmol min⁻¹ g⁻¹). Cao *et al.* [439] introduced a straightforward and broadly applicable method for synthesizing MOFs equipped with covalently bound active metal-N-heterocyclic carbene (M-NHC, where M represents Pd or Ir) single-site catalysts. This innovative technique used a soluble Ag salt AgOC(CF₃)₃ as a precursor, followed by a transmetalation step to incorporate the active metal sites. The Pd-NHC-MIL-101 and Ir-NHC-MIL-101 promote Suzuki coupling reactions and hydrogen transfer reactions effectively (Figure 55).

By synergistically integrating photo organocatalysts with diverse catalyst types such as enantioselective catalysts, MOFs open up a new vista for addressing more complex reactions in photocatalysis. A notable example of this integration is evident in the enantiomeric MOFs, Zn-PYI1 [440]. This MOF is integrated by the stereoselective organocatalyst L-pyrrolidin-2-ylimidazole (PYI) and a triphenylamine photoredox group into a single framework. The Zn-PYI1 showcases a remarkable prowess in the photocatalytic α-alkylation of aliphatic aldehydes, boasting a yield of 74% and an outstanding enantioselectivity of 92% ee. This innovation underscores the potential of tailored MOFs in advancing the realm of photocatalysis.

Encapsulating polyoxometalates within MOFs introduces highly active sites into the MOF structures. An innovative venture by Duan *et al.* [441] involved the encapsulation of the photoredox-active catalyst [SiW₁₁O₃₉Ru-(H₂O)]⁵⁻ within a copper-based MOF (CR-BPY1). This methodological amalgamation harmonizes Cu-catalysis with Ru-photocatalysis within a unified MOF matrix. Pertinently, the direct

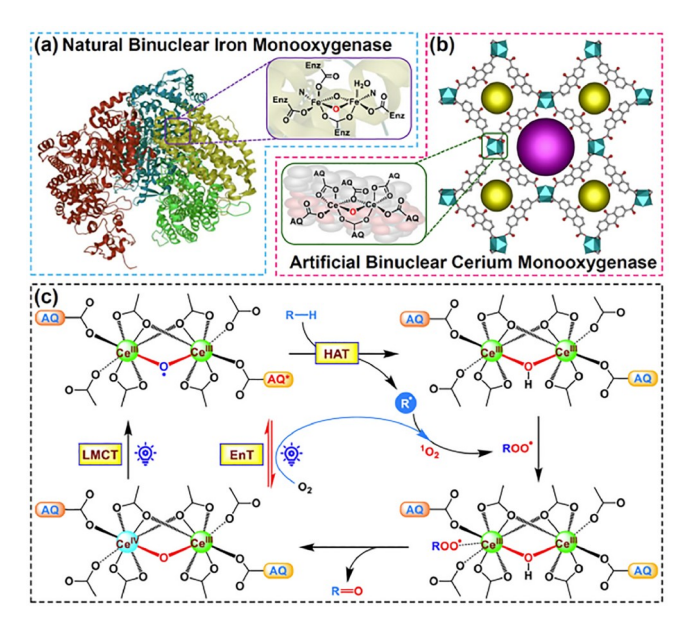


Figure 54 (Color online) (a) Natural binuclear iron monooxygenase. (b) MOF-based artificial binuclear cerium monooxygenase. (c) The photoexcitation of MOF-based artificial monooxygenase triggers the HAT process for the selective oxidation of inert C(sp³)–H bonds, including the EnT and LMCT for the formation of singlet oxygen and oxygen bridge radicals, respectively. Reproduced with permission from Ref. [435]. Copyright@2022, American Chemical Society.

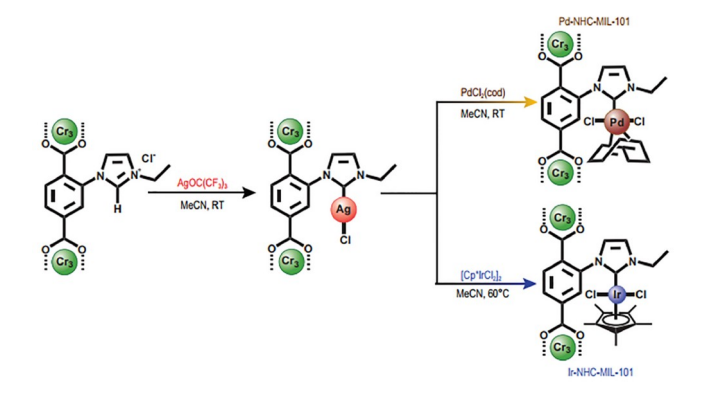


Figure 55 (Color online) The preparation of Pd-NHC-MIL-101 and Ir-NHC-MIL-101 by the reaction of mesoporous imidazolium-functionalized MIL-101 with the soluble AgOC(CF₃)₃ reagent followed by a transmetalation process with PdCl₂(cod) and [Cp*IrCl₂]₂, respectively. Reproduced with permission from Ref. [439]. Copyright@2022, Oxford University Press.

Cu^{II}-O-W(Ru) bridges in this configuration result in a synergistic interplay between the dual metal catalytic paradigms, facilitating the oxidative C–C bond formation between acetophenones and *N*-phenyl-tetrahydroisoquinoline, leading to outstanding conversion efficiencies of 90% coupled with significant size selectivity. The inclusion of metal NPs within MOF matrices has the dual benefit of enhancing charge separation (thereby increasing the efficiency of organic transformations through photocatalysis) and enabling cascade reactions by virtue of the cooperative effects

between the metal NPs and the MOF catalysts [442–444]. For instance, a Pd NCs@ZIF-8 ensemble encompassed ~17 nm Pd nanocubes (NCs), facilitated plasmon-induced photothermal hydrogenation at room temperature, achieving a notable TOF of 675 mol_{1-hexene} mol⁻¹_{Pd} min⁻¹. This signifies a major advancement in the field of photocatalytic organic transformations due to the synergistic effect of the embedded Pd NCs and the ZIF-8 framework [445].

In addition to noble metal NPs, semiconductor composites have also been studied for photocatalytic organic transformation. In one example of combining semiconductor NPs with MOFs, CdS nanorods were deposited on the surface of UiO-66-NH₂ [446,447]. The CdS-UiO-66-NH₂ nanocomposites display a good conversion (31%) and high selectivity (nearly 100%) for photocatalytic oxidation of alcohols to the corresponding aldehydes under mild conditions [447]. While the substrate alcohols contain electrondonating groups as in *p*-methoxy benzyl alcohol, the conversion reaches up to 63.2%. Thus, the fusion of gust material within MOF matrices not only amplifies photocatalytic efficacy but also provides a robust, stable, and selective platform for a myriad of light-driven organic transformations.

The encapsulation of large guest molecules, like metalorganic polyhedra (MOP) [448] and enzymes [449,450], within MOF structures, represents an innovative strategy to enhance the catalytic properties of these guests. The synergy between the MOF and the guest molecule often leads to improved stability and reactivity, which can significantly boost the performance of catalytic transformations. Li *et al.* [448] encapsulated Pd₆-L₆ MOP into the MOFs via a hydrophilicity-directed approach, and thus obtained M₆L₄ \subset MIL-101-4. The hybrid catalyst showed significantly improved activity and selectivity, giving 98% selectivity to benzaldehyde at 95% conversion under identical conditions, showcasing the effectiveness of the encapsulation strategy.

In addition to the aforementioned reactions, the field of photocatalytic ammonia synthesis (PAS) has emerged as a pivotal strategy for alleviating energy crises and advancing toward carbon neutrality [451]. The archetypal photocatalysts for ammonia synthesis share a suite of attributes that are desirable for the construction of an optimal catalyst: (1) physical properties, which include a large specific surface area, an apt band structure, robust absorption of visible light, a cohesive charge transfer pathway, and elevated carrier separation efficiency; (2) chemical properties, characterized by pronounced stability, a structure amenable to tuning, facile modification, and optimal N₂ adsorption energy that ensures selectivity towards N₂ reduction. By virtue of the modularized composition and tractable characteristics, MOFs are ideal platforms for constructing bimetallic clusters and modularized functional regions to implement the nitrogenase-inspired design. For the metal nodes, the bimetallic clusters containing transition metals can be constructed to mimic the MoFe protein [452]. A bimetallic Zr-Hf MOFs photocatalyst exhibits a nitrogen fixation rate up to $116.1 \mu \text{mol g}^{-1} \text{ h}^{-1}$ under visible light. This result is attributed to the ligand-to-metal-to-metal electron transfer pathway and a Zr-based π -back bonding mechanism initiated in the Zr-O-Hf cluster [453].

Moreover, the integration of a molecular active site within a MOF enables nitrogen fixation under ambient conditions. Zuo *et al.* [454] reported a zinc-based MOF {[Zn(L)(N₂)_{0.5}-(TCN-TCNQ)_{0.5}]·(TCNQ)_{0.5}}_n (L is tetra(isoquinolin-6-yl) tetrathiafulvalene), which exhibits an ammonia conversion rate of 140 µmol g⁻¹ h⁻¹. Experimental and theoretical studies revealed that the active [Zn²⁺-(N \equiv N)⁻-Zn²⁺] sites are instrumental in fostering NH₃ formation. The release of the synthesized NH₃ yields unsaturated [Zn²⁺···Zn⁺] intermediates, which are rapidly repleted by atmospheric N₂ capture and swift intermolecular electron transfer. These [Zn²⁺···Zn⁺] intermediates, secured within a structured cagelike donor-acceptor-donor matrix, facilitate a sustainable cycle of catalytic activity.

8 Electrochemistry and electrocatalysis

In recent decades, the realms of electrochemistry and electrocatalysis have witnessed significant advancements, primarily because of the emergence of innovative materials that cater to diverse applications. The integration of MOFs into electrochemical systems elucidates both challenges and unprecedented opportunities [455–457]. The following part delves into the nuanced electrochemical behaviors of MOFs and explores their burgeoning roles at the forefront of electrocatalytic applications.

8.1 Electrochemistry

The synergy between MOFs and electrochemistry is multifaceted. On one hand, the modular nature of MOFs allows for tailoring specific electroactive sites, offering a level of precision rarely attainable with alternative materials. Conversely, the inherent porosity of MOFs ensures fast mass transfer, which stands as a cornerstone for numerous electrochemical procedures. This delicate balance between structural malleability and functional versatility earmarks MOFs as prime contenders for an array of electrochemical endeavors, spanning from energy storage to advanced catalysis.

The redox behaviors of MOFs can be mostly attributed to metal centers, particularly when they are constituted by transition metals, often harboring multiple stable oxidation states. A case in point is the ZIF-8 nanomaterials, synthesized from various zinc sources and employed as electro-

catalysts for the reduction of CO₂ to CO [458]. Intriguingly, ZIF-8 exhibited superior catalytic efficacy for CO₂ electroreduction, achieving a commendable 65% CO yield. It is the discrete Zn nodes that are indispensable for elevated CO selectivity, given that the Co analog or a disintegrated ZIF-8 matrix gives negligible activity for CO₂ reduction.

Bimetallic MOFs have been extensively explored as highly efficient electrocatalysts, predominantly for oxygen reduction reaction (ORR) and oxygen evolution reaction (OER), as the electronic density distribution at the active sites exhibits a profound influence on their performance [459]. Polymetallic MOFs with first-row transition metals, such as Co-Ni [460,461], Co-Fe [462,463], Fe-Ni [464] and Fe-Zn [465], have received notable attention. Many of these bimetallic MOFs have demonstrated superior electrocatalytic vigor and improved stability, occasionally surpassing the performance metrics of standard noble metal electrocatalysts. The prevailing hypothesis for this amplified electrocatalytic proficiency in bimetallic MOFs revolves around the metal-to-metal interaction via an oxygen bridge (M1-O-M2). For example, Tang et al. [459] elucidated that within the NiCo-BDC MOF, electron migration from Co²⁺ to Ni²⁺ occurs via a Co-O-Ni path (with O stemming from the carboxylate ligand). This electronic redistribution at the active centers enhances their interaction with OER intermediates. The subsequent studies on Ni_{0.5}Co_{0.5}-MOF-74 which undergoes in situ transformation to form Ni_{0.5}Co_{0.5}OOH_{0.75} uncovered remarkable OER activity. The mechanism inspired further development, culminating in the synthesis of Ni_{0.9}Fe_{0.1}-MOF, which showcased commendably low overpotentials of 198 and 231 mV at 10 and 20 mA cm⁻², respectively.

Introducing a third metal ion to bimetallic MOFs results in trimetallic MOFs, which intriguingly have manifested even more pronounced OER activities. Lang *et al.* [466] synthesized an assortment of Fe/Ni-based trimetallic MOFs (Fe/Ni/Co(Mn)-MIL-53) displaying a distinctive volcano-type OER activity as a function of compositions. The optimized Fe/Ni_{2.4}/Co_{0.4}-MIL-53 delivered a current density of 20 mA cm⁻² at a low overpotential of 236 mV with a small Tafel slope of 52.2 mV dec⁻¹. This synergy, borne from the amalgamation of metals, refines the electronic milieu of the active metal sites, thereby bolstering the catalytic OER. Therefore, the optimized active Ni sites modulated by the other metals play a dominant role in the enhanced OER activity (Figure 56).

Organic linkers, particularly those boasting conjugated systems or electroactive functionalities, offer a plethora of practical implications [467]. Thus, tuning the electron density of the ligand itself by the presence of electron-donating or electron-withdrawing functional groups in MOFs can usher in distinctive electrocatalytic behavior. As the ZIF-8 performed as a model, it can be found that the electron cloud

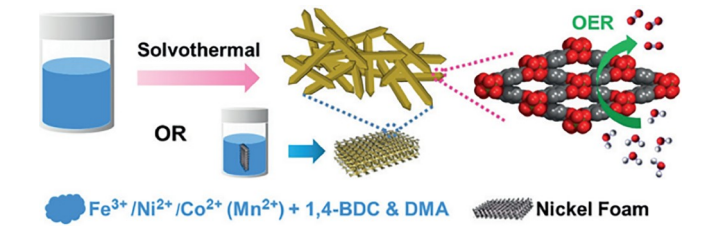


Figure 56 (Color online) Schematic illustration of the preparation of Fe/Ni/Co(Mn)-MIL-53 and Fe/Ni/Co(Mn)-MIL-53/NF, and their direct utilization for OER. Reproduced with permission from Ref. [466]. Copyright@2018, Wiley-VCH GmbH.

density at the Co site was inversely proportional to the electron-withdrawing capabilities of groups such as -CHO and -NO₂ [468]. This was deduced by altering the substituents of the metal with imidazole ligands, ranging from -H to -CH₃, -CHO, and -NO₂. Notably, the electron-withdrawing 2-nitroimidazole group adeptly modulated the electron cloud density at the metal site, thereby unveiling more active sites-leading to the genesis of CoOOH. This proved instrumental in adsorbing and dissociating active species like *OH or *OOH, thus proficiently engendering O₂. Conversely, incorporating an electron-donating group encapsulated the metal active sites, attenuating their OER performance. Empirical data indicated that the zenith of electrocatalytic OER efficiency was attained at an overpotential of 284 mV at 50 mA cm⁻² with a Tafel slope of 151 mV dec⁻¹.

Furthermore, the linkers in MOFs with multitopic orthosubstituted functional groups, such as -NH₂, -OH, -SH, or -SeH are intrinsically involved in electron transfer mechanisms [469]. For instance, by incorporating the nitrogen-rich and electron-deficient tricycloguinazoline (TO) motif into a 2D MOF structure, the resulting Cu₃(HHTQ)₂ showcased an exemplary proficiency in the electrochemical reduction of CO₂ to methanol [470]. While achieving an impressive selectivity of up to 53.6% at -0.4 V vs. RHE, the catalyst exhibited robust durability, maintaining its CO₂RR performance for a minimum of 10 h without significant degradation. Such redox activity has significant implications, especially in energy storage applications, where MOFs can be envisioned as potential electrode materials that enhance charge storage via reversible redox processes. In electrocatalytic contexts, the electron transfer occurring at MOF active sites can accentuate reaction rates and selectivity.

In addition, the architectural design of the ligand has a profound impact on the adsorption configuration of intermediate species, thereby modulating the activity and selectivity of the MOF electrocatalyst. For instance, Mai *et al.* [471] reported a 2-methylimidazole (MI) modulated cobaltiron oxyhydroxide OER catalyst, denoted as (Fe, Co)OOH/MI, characterized by its low crystallinity and nanosheet morphology. This unique structural attribute augments the

exposure of active sites while bolstering mass transfer efficiency. Concurrently, MI modulation refines the electronic configuration of the catalyst. Specifically, the synergy of MI with (Fe, Co)OOH diminishes the orbital overlap between Fe/Co 3d and O 2p orbitals, attenuating the adsorption to oxygen-bearing intermediates and thereby promoting the challenging O₂ desorption step. In alignment with expectations, the (Fe, Co)OOH/MI demonstrates ultralow overpotentials of 230 and 290 mV at 10 and 100 mA cm⁻² in OER, respectively.

Lastly, ligand engineering by replacing the regular linkers with exotic ones provides a strategic avenue for tuning the activity of metal nodes [472-474]. For instance, Li et al. [473] illustrated that by partially substituting the BDC linkers with the carboxyferrocene (Fc) ligands in Co(BDC) MOF, a higher conductivity was attained. This replacement was also found to amplify the binding energy of the Co nodes, signifying alterations in the coordination environment of the active center. The extended X-ray absorption fine structure (EXAFS) further corroborated a lowered coordination number for the Co-active center. Remarkably, this judicious partial linker exchange culminated in an enhanced electrocatalytic OER performance, necessitating an overpotential (η) of 178 mV to achieve 10 mA cm⁻² current density, thus surpassing the performance of the benchmark commercial RuO2 by 57 mV.

MOF-based composites are employed as efficient electrocatalysts, which can be broadly bifurcated into two distinct categories. The first category envisions MOFs as repositories of active sites, with supplementary components buttressing the electrical conductivity and robustness of the MOFs. A salient strategy within this paradigm entails the amalgamation of carbon-based materials with MOFs. Mao et al. [475] crafted a suite of Co-MOF-carbon nanocomposites by integrating either multi-walled carbon nanotubes (CNTs) or graphene oxide (GO). Notably, in comparison to the unaltered Co-MOF, the peak potentials of the ORR over Co-MOF@CNT-2 and Co-MOF@rGO-3 exhibited positive shifts by 0.21 and 0.28 V, respectively, and with corresponding surges in peak currents by 1.8 folds and 2.6 folds, respectively. Intriguingly, the electrocatalytic ORR mechanism underwent a metamorphosis: transitioning from the two-electron reduction pathway characteristic of the pristine Co-MOF to the four-electron reduction pathway characteristic of the graphene-supported Co-MOF.

In the second category of MOF composites, the incorporated components function as active sites, while MOFs modulate the local cavity environment, significantly amplifying activity and selectivity. In one such study, electron-rich PdCu NPs were encapsulated within a sulfonate-functionalized MOF, UiO-66-SO₃H (referred to as UiO-S). Its microenvironment was further tailored with a hydrophobic PDMS layer, culminating in the PdCu@UiO-S@PDMS

composite [476]. This modified catalyst showcases superior performance in the electrochemical nitrogen reduction reaction (NRR), boasting a Faraday efficiency of 13.16% and a yield of 20.24 μ g h⁻¹ mg_{cat}⁻¹. Experimental and theoretical results jointly demonstrate that the protonated and hydrophobic microenvironment supplies protons for the NRR and suppresses the competitive HER. The electron-rich PdCu sites in PdCu@UiO-S@PDMS promote the formation of the N₂H* intermediates, lowering the NRR energy barrier, and elucidating its commendable performance (Figure 57).

8.2 Electrocatalytic reactions

Electrocatalytic reactions serve as the linchpin for a myriad of energy conversion and storage technologies. Given the pressing demand for advanced electrocatalysts tailored for these important technologies, exploration of MOF-based catalysts becomes essential, particularly emphasizing pivotal reactions such as CO₂RR, HER, OER, and ORR [477–485].

The electrocatalytic reduction of $\rm CO_2$ is a process wherein inert $\rm CO_2$ molecules are converted to carbon-based chemicals via cathode-catalyzed electron and proton transfer reactions (Figure 58). Metalloporphyrins are well-known $\rm CO_2$ reduction catalysts that exhibit high selectivity for the reduction of $\rm CO_2$ to $\rm CO$. An ultra-thin 2D MOF nanosheet [TCPP(Co)/Zr-BTB] with rich $\rm Co-N_4$ active centers, these active centers play a crucial role in enhancing the $\rm CO_2$ adsorption capability and maintaining a moderate binding strength of reaction intermediates, thereby improving the overall efficiency of the catalytic process. The catalyst presented a $\rm FE_{\rm CO}$ of 85.1%, a TOF of 5,315 and $j_{\rm total}$ of

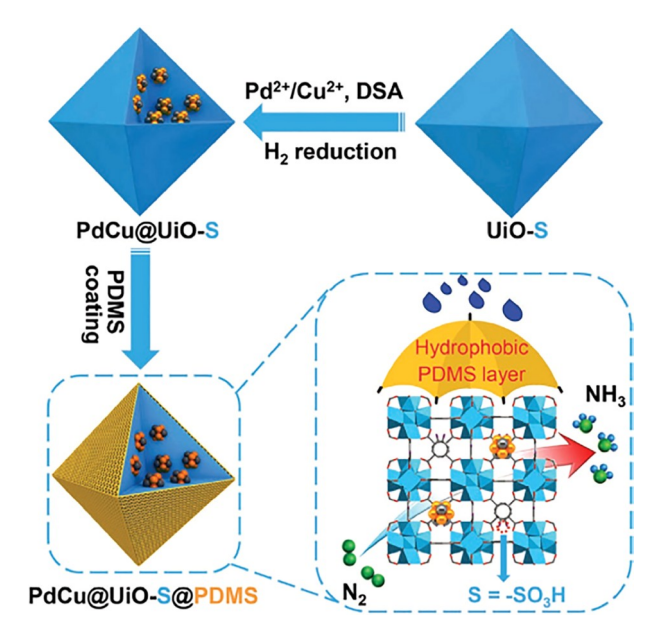


Figure 57 (Color online) Schematic illustration for the stepwise synthesis of PdCu@UiO-S@PDMS with significant functional components/units for improving NRR being highlighted. Reproduced with permission from Ref. [476]. Copyright@2023, Wiley-VCH GmbH.

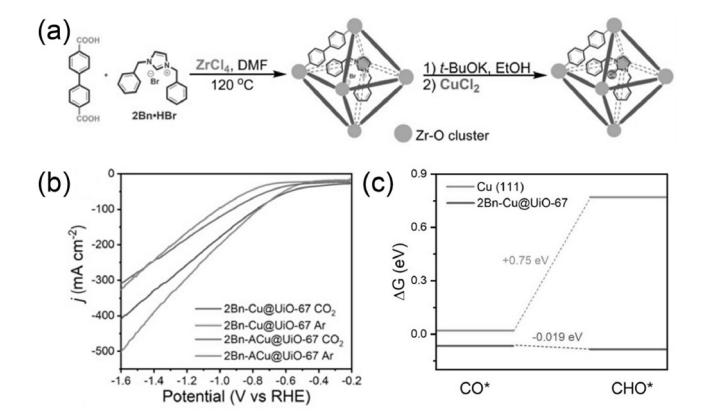


Figure 58 (a) Representation of the synthesis of 2Bn-Cu@UiO-67. (b) Linear sweep voltammetry (LSV) scans of 2BnCu@UiO-67 and 2Bn-ACu@UiO-67 under 1.0 M KOH purged with CO₂ or Ar. The scan rate is 10 mV s⁻¹. (c) Calculated free-energy diagrams for the CO₂RR over 2Bn-Cu@UiO-67. Reproduced with permission from Ref. [487]. Copyright@2022, Wiley-VCH GmbH.

 6 mA cm^{-2} at -0.769 V vs. RHE [486]. Copper is distinguished for its ability to yield highly reduced hydrocarbon products from CO₂, and has been incorporated into MOFs for enhanced electrocatalytic utility [487,488]. For instance, Wang et al. [487] embedded the N-heterocyclic carbene (NHC)-ligated copper single atom sites (2Bn-Cu) into UiO-67 (denote as 2Bn-Cu@UiO-67), achieving a CO2-to-CH4 conversion with an FE of 81% at -1.5 V vs. RHE and a striking TOF of 16.3 s⁻¹ (Figure 58). The σ donation of NHC enriches the surface electron density of Cu single atom sites and promotes the preferential adsorption of CHO* intermediates. Meanwhile, the porosity of the catalyst facilitates the diffusion of CO₂ to 2Bn-Cu, significantly increasing the accessibility of each catalytic center. Furthermore, copperphthalocyanine (CuPc) exhibits electrochemical CO₂ reduction activity for yielding C₂H₄ [489–491]. Liao et al. [491] have elucidated the capabilities of a novel PcCu-Cu-O MOF, which demonstrates superior performance in the electrocatalytic reduction of CO₂ to C₂H₄. This material achieves a FE of 50(±1)% and a current density of 7.3 mA cm^{$^{-2}$} at the potential of -1.2 V vs. RHE in 0.1 M KHCO₃ solution. Insights gleaned from in-situ infrared spectroscopy and control experiments suggest that the enhanced electrochemical performance may be ascribed to the synergistic effect between the CuPc units and the CuO₄ units. This synergy enables an efficient migration of CO from the site of CO generation (the CuO₄ site) to dimerize with the *CO intermediate situated on the site responsible for C₂H₄ production (the CuPc unit), resulting in a lower energy barrier for C-C dimerization. In pursuit of high selectivity for multi-carbon products, Cu-based nanoclusters can be synthe sized through the pre-activation of MOFs [488,492,493]. Yang et al. [493] used sulfur-doped HKUST-1 as the precatalyst, this catalyst exhibits a high ethylene selectivity in an H-type cell with a maximum FE of 60.0%, and a current density of 400 mA cm⁻² with an ethylene FE up to 57.2% in a flow cell. Operando X-ray absorption spectroscopy revealed that Cu^{δ^+} species stabilized by the Cu–S motif exist in S-HKUST-1 during CO_2RR . DFT calculations indicate the partially oxidized Cu^{δ^+} are instrumental for the coupling of the *CO intermediates.

Focusing first on the cathodic half-reaction of water splitting, the HER (Eq. (6)) is a two-electron transfer reaction.

$$2H^{+} + 2e^{-} \rightarrow H_{2} \tag{6}$$

In acidic electrolytes, three reaction steps are possible for the HER:

the Volmer (discharge) step (Eq. (7)):

$$H_3O^+ + e^- \rightarrow H_{ads} + H_2O \tag{7}$$

the Heyrovsky (ion+atom) step (Eq. (8)):

$$H_3O^+ + e^- + \text{cat-H} \rightarrow \text{cat} + H_2 + H_2O$$
 (8)

$$cat-H + cat-H \rightarrow 2cat + H_2 \tag{9}$$

Electrocatalysts characterized by low Tafel slopes and high exchange current densities display high electrocatalytic activity for HER. In this context, a palladium-based MOF (Pd/ MOF) demonstrated commendable HER activity under acidic conditions [494]. Electrochemical assessments revealed its superior performance over bulk MOF, manifested by a Tafel slope of 85 mV dec⁻¹ and an onset overpotential of 105 mV coupled with impressive stability. Indeed, pristine MOF materials, with their inherent unsaturated activation sites, often require coordination with oxygen species, which in turn diminishes their HER activity. Crafting a hybrid catalyst can effectively circumvent these limitations and optimize the performance. A case in point is the hybrid catalyst CoP/Co-MOF [495], combining transition metal phosphides (TMPs) and Co-MOF, which has a large electrochemical active surface area (ECSA) and high electrolyte/ mass diffusion rate (Figure 59). In particular, the electronic structure of CoP could be further effectively modulated through N–P/N–Co bonds, resulting in the optimized binding strengths of water and hydrogen. The CoP/Co-MOF hybrid exhibits an extraordinary pH-universal Pt-like activity and high stability, extraordinary pH-universal Pt-like activity and high stability, with overpotentials of 27, 34, and 49 mV at the current density of 10 mA cm⁻² in 0.5 M H₂SO₄, 1 M KOH, and 1 M phosphate buffer solution (PBS, pH = 7.0), respectively. DFT calculations further substantiate the $\Delta G_{\text{H}_2\text{O}^*}$ and ΔG_{H^*} of the CoP/Co-MOF hybrid compared with its separate constituents, emphasizing its synergistic potential in electrocatalysis.

OER involves the O_2 generation through the electrochemical oxidation of water. In neutral and acidic electrolytes, two H_2O molecules are oxidized into four protons and one O_2 molecule (Eq. (10)), whereas in alkaline electrolytes the hydroxyl groups are oxidized, giving rise to H_2O and O_2

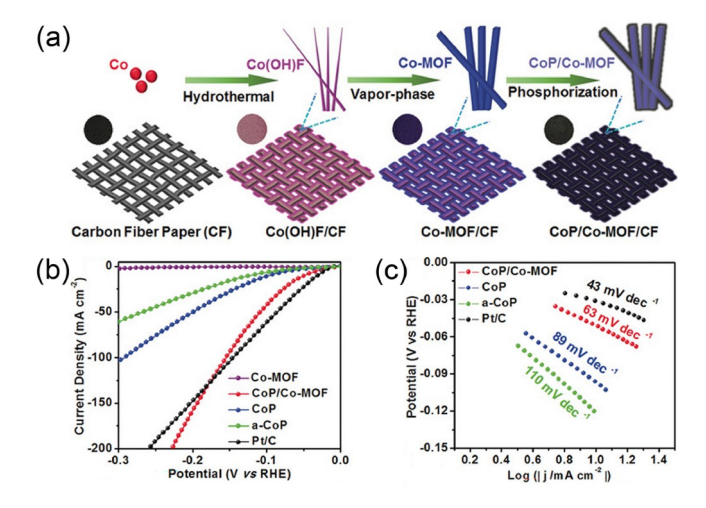


Figure 59 (Color online) (a) Schematic of the fabrication process of CoP/Co-MOF. (b) LSV curves of Co-MOF, CoP/Co-MOF, CoP, a-CoP and Pt/C. (c) Tafel slope of CoP/Co-MOF, CoP, a-CoP, and Pt/C. Reproduced with permission from Ref. [495]. Copyright@2019, Wiley-VCH GmbH.

(Eq. (11)).

$$2H_2O(1) \rightarrow 4H^+ + O_2(g) + 4e^-$$
 (10)
 $4OH^- \rightarrow 2H_2O(1) + O_2(g) + 4e^-$ (11)

The exploration of mixed iron/nickel BTC-MOFs for electrocatalytic OER in 0.1 M KOH unveiled a commendably low onset overpotential of 170 mV (1.4 V vs. RHE) [496]. However, the subpar conductivity of the electrodes greatly constrained the achievement of the current density of 10 mA cm⁻² for practical application. To improve the conductivity, Fe/Ni-BTC MOF thin films were electrochemically deposited on NF electrodes. Particularly, the Fe/Ni-BTC@NF with a Fe/Ni ratio of 1:12 exhibited an overpotential of 270 mV to reach 10 mA cm⁻² and a Tafel slope of 47 mV dec⁻¹. To enhance the number of active sites accessible on the catalyst surface for OER, many 2D nanostructured MOF-based electrocatalysts have been constructed. Zhao et al. [497] engineered an ultrathin nanosheet array of NiFe-MOFs on NF, which demonstrated an overpotential of 240 mV to reach 10 mA cm⁻² in OER, which is much lower than the commercial benchmark catalyst IrO2 (320 mV). Remarkably, while the commercial IrO₂ generates a catalytic current density of 80 mA cm⁻² at 1.7 V vs. RHE, the NiFe-MOF impressively delivers a much higher value of 300 mA cm⁻². Furthermore, the NiFe-MOF nanosheets register a TOF of 3.8 s⁻¹ at an overpotential of 400 mV, which is superior to the 0.14 s⁻¹ of IrO₂. The rotating ring-disk electrode (RRDE) analyses affirmed an electron transfer number of 3.95, in line with the four-electron reduction process of H_2O to O_2 (Eq. (10)).

The ORR is a key process in fuel cells and metal-air batteries, and Pt has been regarded as the benchmark electrocatalyst for this process. The ORR proceeds through four proton-electron transfers to convert O_2 into water in an acidic solution or OH^- ions in an alkaline solution (Eqs. (12) and (13)):

$$O_2 + 4H^+ + 4e^- \rightarrow 2H_2O$$
 (12)

$$O_2 + 2H_2O + 4e^- \rightarrow 4 OH^-$$
 (13)

The four proton-electron transfer process is desirable for fuel cell applications; however, a less-efficient two protonelectron pathway, producing H_2O_2 , is also viable (Eqs. (14) and (15)):

$$O_2 + 2H^+ + 2e^- \rightarrow H_2O_2$$
 (14)

$$O_2 + 2H_2O + 2e^- \rightarrow H_2O_2 + 2OH^-$$
 (15)

MOFs anchored with transition metal centers have demonstrated efficient catalytic activity for ORR. Preliminary studies highlighted the inherent ORR activity in MOFs. revealing a water-stable Cu-bipy-BTC MOF, in which the "Cu-N" moieties are postulated to function as the electroactive sites within 0.1 M PBS (pH 6.0) [498]. Subsequently, advancements were made with the introduction of conductive or semiconducting pristine MOFs tailored for ORR applications. For instance, Liu et al. [499] optimized a Cu-MOF configuration using Cu-HHTP covalent centers, achieving commendable H₂O₂ selectivity of 95%, an impressive FE of 85.4% and a superior H₂O₂ yield rate of 792.7 mmol g_{cat}⁻¹ h⁻¹ during ORR. As revealed via correlative in situ synchrotron radiation spectroscopy, a distinctive energetic moiety of (HO*-Cu)-O-C was in-situ formed during ORR for Cu-HHTP, followed by the shrinking of the first Cu-O coordination sphere around the central Cu sites. This was accompanied by a contraction of the primary Cu–O coordination sphere surrounding the central Cu sites. This dynamic rearrangement in the Cu-O coordination sphere incites electronic polarization at the M-L centers via pronounced π -conjugated covalent interactions, leading to an advantageous adsorption profile for *OOH intermediates on the C sites of (HO*-Cu)-O-C, which favors a 2e ORR pathway.

To achieve enhanced ORR performance, MOF derivatives have been shown to manifest remarkable performance metrics encompassing activity, durability, and methanol tolerance. Notably, certain cutting-edge MOF derivatives have showcased activity surpassing, or at least paralleling, that of benchmark Pt catalysts under identical experimental conditions. For example, Yi et al. [500] prepared the Fe/N/P-triexpanded carbon nanotube (P-Fe-N-CNTs) electrocatalyst characterized by a significant surface area and profuse porous architecture, leveraging a streamlined onestep MOF calcination protocol. This expanded P-Fe-N-CNTs exhibited better metrics such as $E_{\rm onset}$ (1.04 V), $E_{1/2}$ (0.8843 V) than Fe_u-N-CNTs sample and commercial Pt/C catalyst. This enhancement can be attributed to the synergistic interplay of the Fe-N_x/P_x active center and N-, Pco-doping within the carbon nanotube, facilitating rapid oxygen molecule activation. Furthermore, the pronounced surface area and porous nature of the expanded P-Fe-N-CNTs bolster electron transfer, augmenting ORR efficiency. The DFT computations suggest that the introduction of P

dopants promoted the adsorption affinity for OOH* and OH* intermediates. This observation underscores the pivotal role of P doping in modulating the electronic landscape of the active catalytic sites, thereby influencing the overall ORR efficacy of the catalysts.

It should be noted that the true catalytic activity components may not be the original MOFs in some electrocatalytic reaction processes with pristine MOFs as electrocatalysts, especially for OER. Therefore, the stability of MOFs should be considered in electrocatalysis, as MOFs may decompose under operating conditions. *In-situ* characterization techniques should be developed, combined with theoretical calculations, to reveal the real catalytic active sites.

As we look into the future of MOFs in photocatalysis and electrochemistry, our focus must pivot toward overcoming current limitations while leveraging their transformative potential. Addressing the challenge of MOF stability is of great practical urgency; innovations in material engineering are needed to create MOFs that are more resilient to reductive and oxidative stresses, potentially through the development of sturdier metal nodes, functional ligands, or encapsulation within protective barriers. Scaling up the production while ensuring cost-effectiveness will be essential for widespread application. Moreover, integrating computational modeling with experimental research could significantly accelerate the discovery and optimization of MOFs, propelling them into the forefront of energy-related applications. Bridging the gap between laboratory research and industrial application would require real-world testing and industry collaborations to tailor MOF-based systems to commercial needs.

9 Energy storage

Batteries and supercapacitors are the most potential electrical energy storage technologies because they are portable, small in size and can be used on demand. Despite these advantages, physical and chemical limitations of existing materials impede the improvement of performance. MOF-based materials are promising candidates to satisfy the requirements of next-generation energy storage devices (Figure 60). Through innovative synthesis design, characteristics such as particle shape, porosity, stability, and conductivity can be customized for specific applications [501–504]. Due to the different requirements of each energy storage equipment, the versatility of MOFs offers an approach to optimize the properties of materials to overcome electrochemical restrictions.

9.1 Cathode materials

In the process of finding high-performance cathode materials for batteries, the advantages of MOFs such as designability of composition, structural diversity and high porosity supply many opportunities. Currently, Li-based batteries using MOFs as cathode materials are becoming more and more popular. Among Li-based batteries, lithium-ion batteries (LIBs) have been widely utilized in portable electronic products. However, the development of cathode materials in LIBs is limited by low specific capacity, which can directly influence the energy density of the battery [505]. Jiang and co-workers [506] synthesized a 2D copper-benzoquinoid (CuTHQ) MOF with rich porosity and intrinsic redox feature, which prompted this MOF with good electrochemical

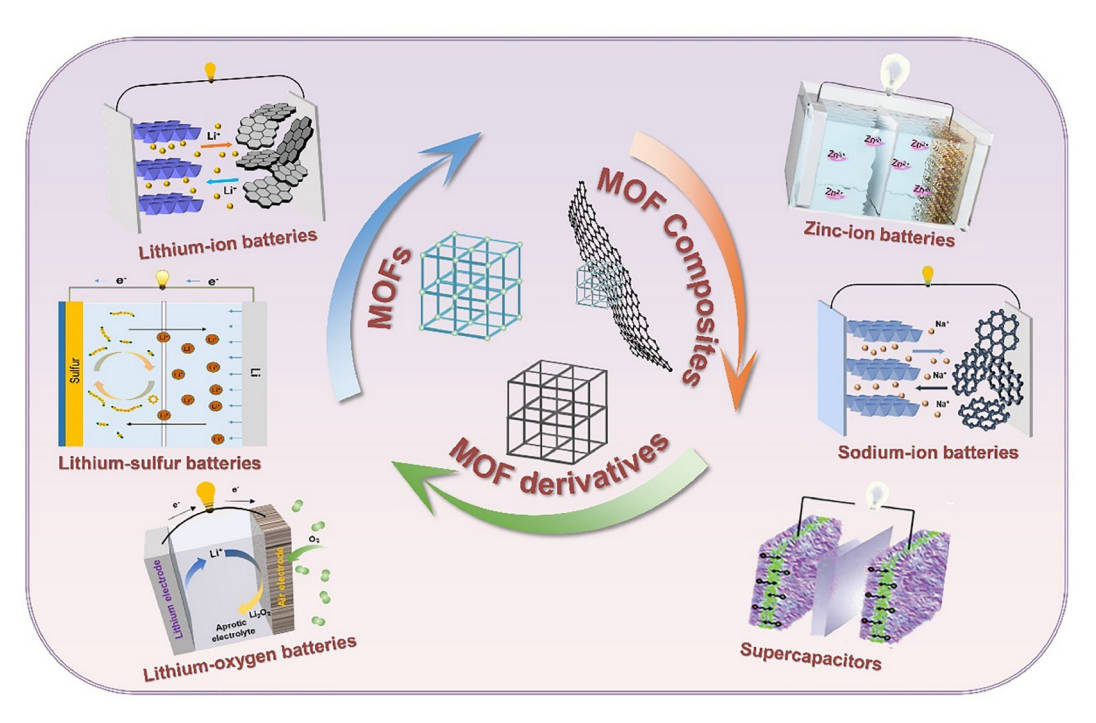


Figure 60 (Color online) Illustration of MOF-based materials for batteries and supercapacitors.

activity. As a cathode in LIBs, large reversible capacity (387 mAh g⁻¹) and high specific energy density (775 Wh kg⁻¹) are achieved. Lithium-sulfur batteries (LSBs) are another promising energy storage device due to ultrahigh theoretical specific capacity. The shuttle effect of the sulfur cathode is the main reason for the fast decline in the capacity of LSBs [507]. The polysulfides anchored on the cathode can improve LSB performance. Jiang et al. [508] combined the polarity and porosity of MOFs with the conductive feature of polypyrrole to construct ppy-MOF compartments (Figure 61a), thus effectively inhibiting the diffusion of polysulfides. Mao et al. [509] fabricated a MOFs/CNT thin film with interpenetrated 3D conductive networks, which endowed this sulfur cathode with a strong confinement effect to realize outstanding performance. In addition, lithium-oxygen (Li-O₂) batteries with high theoretical energy density are also a potential approach in energy storage applications. However, the redox events at the O₂ cathode restricted its efficiency and cyclability. One way to solve this problem is to use a catalyst to promote electrochemical oxygen reduction and evolution, thereby enhancing

specific capacity. Wu *et al.* [510] studied the influence of different MOFs on O_2 cathode performance and found Mn-MOF-74 can achieve a high discharge capacity of 9,420 mAh g⁻¹. The outstanding performance originated from the catalytic effect of metal active sites.

Moreover, the use of MOFs as cathode materials also displays the prospect of other types of batteries. Sodium-ion batteries (SIBs) have attracted widespread attention because of the low cost and abundance of Na. Owing to the rigid open framework and adjustable composition, Prussian blue (PB)based MOFs have received great interest in the preparation of high-performance cathodes for SIBs. Ren and co-workers [511] fabricated a nickel hexacyanoferrate (NiHCF) cathode with enhanced sodium storage activity, which delivered a superior electrochemical performance with rate capability of 71.0 mAh g^{-1} at 44.4 C and capacity retention of 83.2% after 5,000 cycles. Additionally, zinc-ion batteries (ZIBs) have gained great interest because of the low redox potential of Zn and chemical stability. Developing cathode materials with stability and high capacity is the key to ZIBs. Sang et al. [512] presented a highly crystalline 1D π -d conjugated

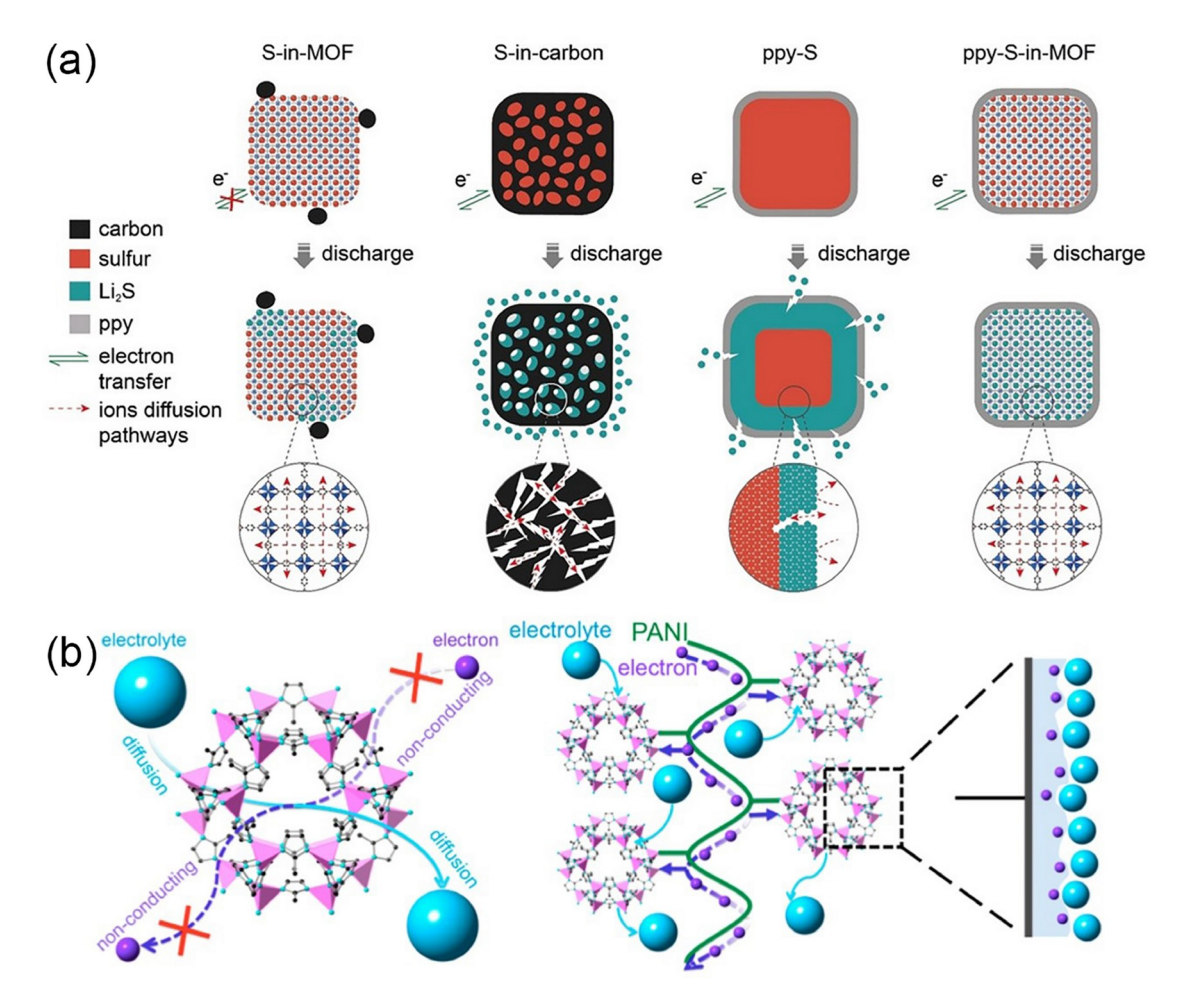


Figure 61 (Color online) (a) The advantages of ppy-MOF as a sulfur host, including polarity, porosity and conductivity. Reproduced with permission from Ref. [508]. Copyright@2018, Wiley-VCH. (b) Schematic diagram of electron and electrolyte conduction in MOF and MOF interwoven by PANI. Reproduced with permission from Ref. [527]. Copyright@2015, American Chemical Society.

conductive Cu-based MOF as a cathode for ZIBs, which results in outstanding rate capability and cycle stability. Recently, aqueous nickel-zinc batteries (NZBs) have also aroused people's extensive interest [513]. Ni-based MOFs used as cathode for aqueous NZBs exhibit high electrical conductivity and specific capacity [514].

9.2 Anode materials

The demand for higher capacity and stability urges researchers to explore more advanced anode materials. Since Chen's team [515] used MOF-177 as the electrode material of LIBs, the application of MOF-based materials in batteries has developed rapidly in China. Currently, MOFs as anode materials are mainly applied in LIBs and SIBs. In terms of LIBs, most LIBs use graphite anodes, but their advantage in specific capacity is not obvious [516]. Owing to their high porosity, diverse structures, and redox-active function, MOFs can play a crucial role in LIB anodes. For example, the porosity of MOFs can enable reversible storage of Li and ensure effective contact with an electrolyte solution to promote ion transportation. The redox-active metal centers can encourage the amount of stored Li⁺, thereby increasing theoretical capacity. Zhou and co-workers [517] reported self-supported nanorod arrays of CPO-27 MOF as an anode for LIBs. The unique 3D architecture design endows the CPO-27 nanoarray with enhanced electron and ion transport, thereby delivering high Li storage performance. Metal oxides as anodes in LIBs are considered promising materials to replace graphite. Cao et al. [518] synthesized mini-hollow polyhedron Mn₂O₃ derived from Mn-based MOFs. The material skillfully uses the nano-size effect and shows good cycling performance of 819.8 mAh g⁻¹ at 1 A g⁻¹ after 1,200 cycles. In SIBs, the development of anode materials is limited by fast capacity fading during cycling. MOF-derived carbon-based materials as anodes in SIBs show great prospects. Liang et al. [519] obtained a 3D porous superstructure assembled with carbon nanobelt arrays decorated with Bi nanospheres coated carbon layer by thermolysis of Bi-MOF nanorods. Owing to its unique structural superiority, this hybrid delivered excellent capacity and cycling stability. In addition, Liu et al. [520] fabricated N-rich porous carbon nanosheets using 2D hexamine-based MOF as a template. The as-obtained carbon material delivers good Na storage capability of 194 mAh g⁻¹ even at 10 A g⁻¹.

9.3 Separator film

The separator is an indispensable component in batteries, which can prevent short circuits inside the battery and provide a channel for ion transmission. At present, MOFs as separators are mainly applied in LIBs and LSBs. However, the problems of impedance increase and capacity attenuation

limit the development of LIBs. As a coping strategy, improving the performance of the separator by modification is advisable. Zhang et al. [521] fabricated a composite separator containing MOF particles and poly(vinyl alcohol). Complexation of anions in electrolytes with OMSs of MOF particles significantly improves Li⁺ migration number and Li⁺ conductivity. Moreover, the introduced MOF particles can effectively reduce the decomposition of electrolytes and promote the reaction kinetics within the electrode, thus improving power performance and extending cycle life. To reduce the shuttle of active materials, separators in LSBs are required to ensure the rapid transfer of Li⁺ and the strong polysulfides interception ability. Gao et al. [522] constructed a MOF-based triple-layer separator with stepped channels, which shows enhanced specific capacity and cycle stability. This may be because the obtained separator can effectively inhibit the shuttle of polysulfides, promote the rapid transfer of Li⁺/ electrolyte and inhibit the polarization of the battery. Moreover, Li et al. [523] reported a "single atom array mimic" on ultrathin MOF nanosheet as a bifunctional separator, which can simultaneously inhibit shuttling of polysulfides and Li dendrite growth. Specifically, the surface Co-O₄ moieties could homogenize Li-ion flux and inhibit Li dendrite growth. The Co single-atom array could efficiently capture polysulfides via Lewis acid-base interaction, thus hindering polysulfide diffusion and enhancing sulfur utilization. Thus, the assembled coin cells with this bifunctional separator exhibited high safety and long life.

9.4 Supercapacitor

Electrochemical capacitors, commonly called supercapacitors (SCs), have attracted increasing attention because of their high power density and long cycling life. Unlike batteries, SCs store charge through electrical double-layer capacitance or pseudocapacitance. Nevertheless, SCs have some issues, such as severe self-discharge, low energy density, and high production costs [524]. The development of high-performance electrode materials plays an important role in breaking through the bottleneck of SCs at present. The high surface area and redox-active metal centers of MOFs make it possible to realize high double-layer capacitance and pseudocapacitance, respectively. Wei's group [525] confirmed earlier that MOFs are promising electrode materials for SCs. However, most MOFs possess poor conductivity and chemical stability that need to be modified. Li and coworkers [526] fabricated conductive MOF nanowire arrays (Cu-CAT NWAs) as an electrode material for SCs. By taking advantage of its high porosity and good conductivity, Cu-CAT NWAs exhibit outstanding rate performance and areal capacitance. Furthermore, assembling MOFs and various functional materials is a greatly efficient strategy to further improve the properties of MOFs. Wang and co-workers

[527] interweaved MOF crystals with polyaniline (PANI) chains to achieve high-performance SCs and overcome MOF insulation problems. Specifically, as a bridge for electron transmission between external circuits and the inner surface of MOFs, PANI chains can effectively improve the conductivity of MOFs and enhance the Faradaic processes across the interface (Figure 61b). In addition, Liu *et al.* [528] combined the redox activity of MOF with the high conductivity of MXene to create a series of MXene/MOF composites. Interestingly, the obtained hollow Ti₃C₂TX/ZIF-67/CoV₂O₆ composites derived from Ti₃C₂TX/ZIF-67 showed significantly enhanced capacitance performance.

10 Summary and outlooks

MOFs have become one of the most popular novel crystalline porous materials in the research area of chemistry and materials, which show great application potential in many fields. In this review, we have discussed the application of MOFs in small molecule storage, separation, optical performance, sensing and detection, chemocatalysis, photocatalysis, electrocatalysis, and energy storage. Although advances have been achieved regarding the property investigation and regulation of MOFs, opportunities still wait regarding the new material development and large-scale application of MOFs. There is still insufficient research on the structure-performance relationship of MOF materials. Further research is needed on the intrinsic properties of MOF materials and the microscopic (atomic, electronic, and even more microscopic) mechanisms under the macroscopic properties of MOF materials. Considering the multi-scale structure and complex interface structure of MOFs, high spatiotemporal- and energy-resolved in situ characterization methods and efficient theoretical prediction methods need to be further developed, to reveal the real microscopic mechanism under working conditions. In addition, there is still a long way to go to achieve the industrialization of MOFs. Performance optimization based on rational chemical design is needed to obtain MOFs with performance surpassing other porous materials. It is also necessary to conduct large-scale "industrial verification" that is close to practical applications, in order to maintain performance and ensure long-term stability of MOFs under working conditions. We hope that this review will furtherance more research on the rational development of MOF materials, and further promote industrialization of this kind of novel porous crystalline materials.

Acknowledgements This work was supported by the National Key Research and Development Program of China (2022YFA1502901), the National Natural Science Foundation of China (22035003, 22201137, 22371137), and the Fundamental Research Funds for the Central Universities (63243115).

Conflict of interest The authors declare no conflict of interest.

- 1 Schoedel A, Ji Z, Yaghi OM. *Nat Energy*, 2016, 1: 16034
- 2 Ding TF, Ozawa S, Yamazaki T, Watanuki I, Ogino Y. *Langmuir*, 1988, 4: 392–396
- 3 Quinn DF, MacDonald JA. Carbon, 1992, 30: 1097-1103
- 4 Chen Z, Li P, Anderson R, Wang X, Zhang X, Robison L, Redfern LR, Moribe S, Islamoglu T, Gómez-Gualdrón DA, Yildirim T, Stoddart JF, Farha OK. Science, 2020, 368: 297–303
- 5 Yin Y, Zhang Y, Zhou X, Gui B, Wang W, Jiang W, Zhang YB, Sun J, Wang C. *Science*, 2024, 386: 693–696
- 6 Shi Z, Zhang Y. Israel J Chem, 2018, 58: 985-994
- 7 Lin J, He C, Liu Y, Liao P, Zhou D, Zhang J, Chen X. Angew Chem Int Ed. 2016, 55: 4674–4678
- 8 Liang CC, Shi ZL, He CT, Tan J, Zhou HD, Zhou HL, Lee Y, Zhang YB. J Am Chem Soc, 2017, 139: 13300–13303
- 9 Zhang M, Zhou W, Pham T, Forrest KA, Liu W, He Y, Wu H, Yildirim T, Chen B, Space B, Pan Y, Zaworotko MJ, Bai J. Angew Chem Int Ed, 2017, 56: 11426–11430
- 10 Wen HM, Li B, Li L, Lin RB, Zhou W, Qian G, Chen B. Adv Mater, 2018, 30: e1704792
- 11 Zhao D, Yu C, Jiang J, Duan X, Zhang L, Jiang K, Qian G. J Solid State Chem, 2019, 277: 139–142
- 12 Ye Y, Lin RB, Cui H, Alsalme A, Zhou W, Yildirim T, Zhang Z, Xiang S, Chen B. *Dalton Trans*, 2020, 49: 3658–3661
- 13 Zhang YF, Zhang ZH, Fang H, Guo XA, Ma YN, Zhang YZ, Xue DX. *Inorg Chem*, 2023, 62: 20513–20519
- 14 Jiang W, Liang C, Zhang Y. Adv Funct Mater, 2024, 34: 2308946
- 15 Li B, Wen HM, Wang H, Wu H, Yildirim T, Zhou W, Chen B. Energy Environ Sci, 2015, 8: 2504–2511
- 16 Li B, Wen HM, Wang H, Wu H, Tyagi M, Yildirim T, Zhou W, Chen B. J Am Chem Soc, 2014, 136: 6207–6210
- 17 Tan J, Tao Y, Zhang X, Wang Q, Zeng T, Shi Z, Cordova KE, Lee Y, Liu H, Zhang YB. *J Mater Chem A*, 2021, 9: 24857–24862
- 18 Kundu T, Shah BB, Bolinois L, Zhao D. Chem Mater, 2019, 31: 2842–2847
- 19 Han Z, Yang Y, Rushlow J, Liang RR, Zhou HC. Acc Chem Res, 2024, 57: 3217–3226
- 20 He B, Zhang H, Xu L, Liu Y, Lang F, Pang J. Chin J Inorg Chem, 2024, 40: 2041–2062
- 21 Li J, Yuan S, Qin J, Pang J, Zhang P, Zhang Y, Huang Y, Drake HF, Liu WR, Zhou H. Angew Chem Int Ed. 2020, 59: 9319–9323
- 22 Pang J, Di Z, Qin JS, Yuan S, Lollar CT, Li J, Zhang P, Wu M, Yuan D, Hong M, Zhou HC. J Am Chem Soc, 2020, 142: 15020–15026
- 23 Pang J, Yuan S, Qin JS, Lollar CT, Huang N, Li J, Wang Q, Wu M, Yuan D, Hong M, Zhou HC. *J Am Chem Soc*, 2019, 141: 3129–3136
- 24 Lollar CT, Pang J, Qin J, Yuan S, Powell JA, Zhou HC. *Cryst Growth Des*, 2019, 19: 2069–2073
- 25 Pang J, Yuan S, Qin J, Wu M, Lollar CT, Li J, Huang N, Li B, Zhang P, Zhou HC. *J Am Chem Soc*, 2018, 140: 12328–12332
- 26 Chen CX, Wei ZW, Jiang JJ, Zheng SP, Wang HP, Qiu QF, Cao CC, Fenske D, Su CY. *J Am Chem Soc*, 2017, 139: 6034–6037
- 27 Fang H, Zheng B, Zhang Z, Li H, Xue D, Bai J. Angew Chem Int Ed, 2021, 60: 16521–16528
- 28 Zhang ZH, Fang H, Xue DX, Bai J. ACS Appl Mater Interfaces, 2021, 13: 44956–44963
- 29 Lei J, Yuan W, Shang J, Xu J, Zhang P, Wang Y, Li YP, Zhai QG. Inorg Chem, 2023, 62: 15195–15205
- 30 Wang B, Zhang X, Huang H, Zhang Z, Yildirim T, Zhou W, Xiang S, Chen B. Nano Res, 2021, 14: 507–511
- 31 Zhang X, Lin RB, Alothman ZA, Alduhaish O, Yildirim T, Zhou W, Li JR, Chen B. *Inorg Chem Front*, 2023, 10: 454–459
- 32 Kaye SS, Dailly A, Yaghi OM, Long JR. J Am Chem Soc, 2007, 129: 14176–14177
- 33 Peng P, Anastasopoulou A, Brooks K, Furukawa H, Bowden ME, Long JR, Autrey T, Breunig H. Nat Energy, 2022, 7: 448–458

- 34 Rosi NL, Eckert J, Eddaoudi M, Vodak DT, Kim J, O'Keeffe M, Yaghi OM. Science, 2003, 300: 1127–1129
- 35 Zhang B, Sun Y, Xu H, He X. Carbon Neutr, 2023, 2: 632-645
- 36 Zhang Y, Zhang W, Feng F, Zhang J, Chen X. Angew Chem Int Ed, 2009, 48: 5287–5290
- 37 Zhang YB, Zhou HL, Lin RB, Zhang C, Lin JB, Zhang JP, Chen XM. Nat Commun, 2012, 3: 642
- 38 Zhang X, Lin RB, Wang J, Wang B, Liang B, Yildirim T, Zhang J, Zhou W, Chen B. Adv Mater, 2020, 32: 1907995
- 39 Sengupta D, Melix P, Bose S, Duncan J, Wang X, Mian MR, Kirlikovali KO, Joodaki F, Islamoglu T, Yildirim T, Snurr RQ, Farha OK. J Am Chem Soc, 2023, 145: 20492–20502
- 40 Yu C, Li H, Wang Y, Suo J, Guan X, Wang R, Valtchev V, Yan Y, Qiu S, Fang Q. Angew Chem Int Ed, 2022, 61: e202117101
- 41 Zhang YB, Furukawa H, Ko N, Nie W, Park HJ, Okajima S, Cordova KE, Deng H, Kim J, Yaghi OM. J Am Chem Soc, 2015, 137: 2641–2650
- 42 Zhang JP, Zhu AX, Lin RB, Qi XL, Chen XM. Adv Mater, 2011, 23: 1268–1271
- 43 Hanikel N, Prévot MS, Yaghi OM. Nat Nanotechnol, 2020, 15: 348– 355
- 44 Kim H, Yang S, Rao SR, Narayanan S, Kapustin EA, Furukawa H, Umans AS, Yaghi OM, Wang EN. Science, 2017, 356: 430–434
- 45 Almassad HA, Abaza RI, Siwwan L, Al-Maythalony B, Cordova KE. Nat Commun, 2022, 13: 4873
- 46 Cheng M, Bai H, Wang X, Chang Z, Cao M, Bu XH. Adv Mater, 2024, 36: e2411680
- 47 Ma D, Li P, Duan X, Li J, Shao P, Lang Z, Bao L, Zhang Y, Lin Z, Wang B. Angew Chem Int Ed, 2020, 59: 3905–3909
- 48 Zhang YZ, He T, Kong XJ, Lv XL, Wu XQ, Li JR. ACS Appl Mater Interfaces, 2018, 10: 27868–27874
- 49 Liu W, Wu E, Yu B, Liu Z, Wang K, Qi D, Li B, Jiang J. Angew Chem Int Ed, 2023, 62: e202305144
- 50 Xu H, Wu Y, Yang L, Rao Y, Wang J, Peng S, Li Q. Angew Chem Int Ed. 2023, 62: e202217864
- 51 Li J, Wang Y, Chen Y, Xiong Q, Yang J, Li L, Li J. Chin J Chem Eng, 2022, 49: 170–177
- 52 An H, Chen Y, Wang Y, Liu X, Ren Y, Kang Z, Li J, Li L. Chem Eng J, 2023, 461: 141955
- 53 Xu J, Li T, Chao J, Wu S, Yan T, Li W, Cao B, Wang R. Angew Chem Int Ed, 2020, 59: 5202–5210
- 54 Shao Z, Wang ZS, Lv H, Tang YC, Wang H, Du S, Sun R, Feng X, Poredoš P, Zhou DD, Zhang JP, Wang R. Appl Phys Rev, 2023, 10: 041409
- 55 Furukawa H, Gándara F, Zhang YB, Jiang J, Queen WL, Hudson MR, Yaghi OM. J Am Chem Soc, 2014, 136: 4369–4381
- 56 Hanikel N, Pei X, Chheda S, Lyu H, Jeong WS, Sauer J, Gagliardi L, Yaghi OM. Science, 2021, 374: 454–459
- 57 Rao X, Cai J, Yu J, He Y, Wu C, Zhou W, Yildirim T, Chen B, Qian G. *Chem Commun*, 2013, 49: 6719–6721
- 58 Pang J, Jiang F, Wu M, Liu C, Su K, Lu W, Yuan D, Hong M. Nat Commun, 2015, 6: 7575
- 59 Wen HM, Wang H, Li B, Cui Y, Wang H, Qian G, Chen B. *Inorg Chem*, 2016, 55: 7214–7218
- 60 Wang J, Fan S, Li H, Bu X, Xue Y, Zhai Q. Angew Chem Int Ed, 2023, 62: e202217839
- 61 Gillon X, Houssiau L. Plasma Sour Sci Technol, 2014, 23: 045010
- 62 Zhang JP, Chen XM. *J Am Chem Soc*, 2009, 131: 5516–5521
- 63 Sholl DS, Lively RP. *Nature*, 2016, 532: 435–437
- 64 Qian Q, Asinger PA, Lee MJ, Han G, Mizrahi Rodriguez K, Lin S, Benedetti FM, Wu AX, Chi WS, Smith ZP. *Chem Rev*, 2020, 120: 8161–8266
- 65 Yang L, Qian S, Wang X, Cui X, Chen B, Xing H. Chem Soc Rev, 2020, 49: 5359–5406
- 66 Hou R, Fong C, Freeman BD, Hill MR, Xie Z. Sep Purif Tech, 2022, 300: 121863
- 67 Ulbricht M. *Polymer*, 2006, 47: 2217–2262

- 68 Angelini PA, Counce T, Griffith R, Klasson WL, Muralidharan T, Narula G, Sikka C, Closset V, Keller G, Watson GJ. Materials for SeparationTechnologies. Energy and Emission Reduction Opportunities. OakRidge: Oak Ridge National Lab. (ORNL), 2005
- 69 Li JR, Kuppler RJ, Zhou HC. Chem Soc Rev, 2009, 38: 1477-1504
- 70 Guo FJ, Yang N, Li HX, Fang H, Xue DX. *Chin J Struct Chem*, 2023, 42: 100012
- 71 Adil K, Belmabkhout Y, Pillai RS, Cadiau A, Bhatt PM, Assen AH, Maurin G, Eddaoudi M. Chem Soc Rev, 2017, 46: 3402–3430
- 72 Di Z, Pang J, Hu F, Wu M, Hong M. Nano Res, 2021, 14: 2584–2588
- 73 Li H, Liu C, Chen C, Di Z, Yuan D, Pang J, Wei W, Wu M, Hong M. Angew Chem Int Ed, 2021, 60: 7547–7552
- 74 Liu HR, Wang SM, Dong YL, Zheng ST, Ni S, Xu J, Yang QY. Chin J Struct Chem, 2023, 42: 100022
- 75 Yang H, Xue L, Yang X, Xu H, Gao J. Chin J Struct Chem, 2023, 42: 100034
- 76 Yang SQ, Hu TL. Coord Chem Rev, 2022, 468: 214628
- 77 Yeo BC, Kim D, Kim H, Han SS. J Phys Chem C, 2016, 120: 24224– 24230
- 78 Wang T, Lin E, Peng YL, Chen Y, Cheng P, Zhang Z. Coord Chem Rev. 2020, 423: 213485
- 79 Reed DA, Keitz BK, Oktawiec J, Mason JA, Runčevski T, Xiao DJ, Darago LE, Crocellà V, Bordiga S, Long JR. *Nature*, 2017, 550: 96– 100
- 80 Lang F, Pang J, Bu XH. eScience, 2024, 4: 100231
- 81 Mason JA, Oktawiec J, Taylor MK, Hudson MR, Rodriguez J, Bachman JE, Gonzalez MI, Cervellino A, Guagliardi A, Brown CM, Llewellyn PL, Masciocchi N, Long JR. *Nature*, 2015, 527: 357–361
- 82 Chen Y, Lu W, Schröder M, Yang S. Acc Chem Res, 2023, 56: 2569– 2581
- 83 Lin RB, Zhang Z, Chen B. Acc Chem Res, 2021, 54: 3362–3376
- 84 Kökçam-Demir Ü, Goldman A, Esrafili L, Gharib M, Morsali A, Weingart O, Janiak C. Chem Soc Rev, 2020, 49: 2751–2798
- 85 Lee K, Howe JD, Lin LC, Smit B, Neaton JB. *Chem Mater*, 2015, 27: 668–678
- 86 Denysenko D, Grzywa M, Jelic J, Reuter K, Volkmer D. Angew Chem Int Ed, 2014, 53: 5832–5836
- 87 Jaramillo DE, Jaffe A, Snyder BER, Smith A, Taw E, Rohde RC, Dods MN, DeSnoo W, Meihaus KR, Harris TD, Neaton JB, Long JR. Chem Sci, 2022, 13: 10216–10237
- 88 Demessence A, D'Alessandro DM, Foo ML, Long JR. J Am Chem Soc, 2009, 131: 8784–8786
- 89 Liao PQ, Chen H, Zhou DD, Liu SY, He CT, Rui Z, Ji H, Zhang JP, Chen XM. Energy Environ Sci, 2015, 8: 1011–1016
- 90 Zhou DD, Zhang XW, Mo ZW, Xu YZ, Tian XY, Li Y, Chen XM, Zhang JP. EnergyChem, 2019, 1: 100016
- 91 Vaidhyanathan R, Iremonger SS, Shimizu GKH, Boyd PG, Alavi S, Woo TK. Science, 2010, 330: 650–653
- 92 Zhang JP, Zhang YB, Lin JB, Chen XM. Chem Rev, 2011, 112: 1001–1033
- 93 Lin JB, Zhang JP, Chen XM. *J Am Chem Soc*, 2010, 132: 6654–6656
- 94 Liao PQ, Zhang WX, Zhang JP, Chen XM. *Nat Commun*, 2015, 6: 8697
- 95 Wang Q, Ning D, Chen H, Chen Y, Li J, Li L. *Chin J Struct Chem*, 2023, 42: 100147
- 96 Sun M, Liu H, Wang X, Yang X, Gao F, Xie D, Fan W, Han Y, Xu B, Sun D. *Chin J Struct Chem*, 2023, 42: 100146
- 97 Wan Y, Kong D, Xiong F, Qiu T, Gao S, Zhang Q, Miao Y, Qin M, Wu S, Wang Y, Zhong R, Zou R. Chin J Chem Eng, 2023, 61: 82–89
- 98 Zhang Y, Han Y, Luan B, Wang L, Yang W, Jiang Y, Ben T, He Y, Chen B. J Am Chem Soc, 2024, 146: 17220–17229
- 99 Zhao Y, Chen Q, Zhang X, Li J. Adv Sci, 2024, 11: 2310025
- 100 Li J, Gan Y, Chen J, Lin R, Yang Y, Wu H, Zhou W, Chen B, Chen X. Angew Chem Int Ed, 2024, 63: e202400823
- 101 Zhang L, Lang F, Xi XJ, Yin S, Pang J, Zheng W, Bu XH. *Inorg Chem*, 2024, 63: 8329–8335
- 102 Yang SQ, Zhou L, Xing B, Zhang YH, Hu TL. Chin J Struct Chem,

- 2023, 42: 100004
- 103 Niu Z, Cui X, Pham T, Lan PC, Xing H, Forrest KA, Wojtas L, Space B, Ma S. *Angew Chem Int Ed*, 2019, 58: 10138–10141
- 104 Lin RB, Xiang S, Zhou W, Chen B. Chem, 2020, 6: 337-363
- 105 Zhang XW, Wang C, Mo ZW, Chen XX, Zhang WX, Zhang JP. *Nat Mater*, 2024, 23: 116–123
- 106 Zhou DD, Zhang JP. Acc Chem Res, 2022, 55: 2966-2977
- 107 Coudert FX, Jeffroy M, Fuchs AH, Boutin A, Mellot-Draznieks C. J Am Chem Soc, 2008, 130: 14294–14302
- 108 Li N, Pang J, Lang F, Bu XH. Acc Chem Res, 2024, 57: 2279–2292
- 109 Zhou DD, Chen P, Wang C, Wang SS, Du Y, Yan H, Ye ZM, He CT, Huang RK, Mo ZW, Huang NY, Zhang JP. *Nat Mater*, 2019, 18: 994–998
- 110 Wang H, Liu Y, Li J. Adv Mater, 2020, 32: 2002603
- 111 Zhang XW, Zhou DD, Zhang JP. Chem, 2021, 7: 1006-1019
- 112 Cadiau A, Adil K, Bhatt PM, Belmabkhout Y, Eddaoudi M. Science, 2016, 353: 137–140
- 113 Antypov D, Shkurenko A, Bhatt PM, Belmabkhout Y, Adil K, Cadiau A, Suyetin M, Eddaoudi M, Rosseinsky MJ, Dyer MS. Nat Commun. 2020. 11: 6099
- 114 Zhang JP, Chen XM. J Am Chem Soc, 2008, 130: 6010–6017
- 115 Ma S, Sun D, Wang X, Zhou H. Angew Chem Int Ed, 2007, 46: 2458–2462
- 116 Gu C, Hosono N, Zheng JJ, Sato Y, Kusaka S, Sakaki S, Kitagawa S. Science, 2019, 363: 387–391
- 117 He CT, Tian JY, Liu SY, Ouyang G, Zhang JP, Chen XM. Chem Sci, 2013, 4: 351–356
- 118 Liao PQ, Huang NY, Zhang WX, Zhang JP, Chen XM. Science, 2017, 356: 1193–1196
- 119 Walton KS, Sholl DS. AIChE J, 2015, 61: 2757–2762
- 120 Peng Y, Li Y, Ban Y, Jin H, Jiao W, Liu X, Yang W. Science, 2014, 346: 1356–1359
- 121 Song H, Peng Y, Wang C, Shu L, Zhu C, Wang Y, He H, Yang W. Angew Chem Int Ed, 2023, 62: e202218472
- 122 Peng Y, Li Y, Ban Y, Yang W. Angew Chem Int Ed, 2017, 56: 9757–9761
- 123 Yuan H, Li K, Shi D, Yang H, Yu X, Fan W, Buenconsejo PJS, Zhao D. *Adv Mater*, 2023, 35: e2211859
- 124 Ma X, Wu X, Caro J, Huang A. Angew Chem Int Ed, 2019, 58: 16156–16160
- 125 Chen G, Chen C, Guo Y, Chu Z, Pan Y, Liu G, Liu G, Han Y, Jin W, Xu N. Science, 2023, 381: 1350–1356
- 126 Xiang L, Sheng L, Wang C, Zhang L, Pan Y, Li Y. Adv Mater, 2017, 29: 1606999
- 127 Hou Q, Wu Y, Zhou S, Wei Y, Caro J, Wang H. Angew Chem Int Ed, 2019, 58: 327–331
- 128 Ban Y, Li Z, Li Y, Peng Y, Jin H, Jiao W, Guo A, Wang P, Yang Q, Zhong C, Yang W. Angew Chem Int Ed, 2015, 54: 15483–15487
- 129 Qu K, Huang K, Xu J, Dai L, Wang Y, Cao H, Xia Y, Wu Y, Xu W, Yao Z, Guo X, Lian C, Xu Z. Angew Chem Int Ed, 2022, 61: e202213333
- Yang Z, Belmabkhout Y, McHugh LN, Ao D, Sun Y, Li S, Qiao Z, Bennett TD, Guiver MD, Zhong C. Nat Mater, 2023, 22: 888–894
- 131 Ma C, Yang Z, Guo X, Qiao Z, Zhong C. J Membrane Sci, 2022, 663: 121069
- 132 Gu Z, Yang Z, Guo X, Qiao Z, Zhong C. Sep Purif Tech, 2021, 272: 118845
- 133 Gu Z, Yang Z, Sun Y, Qiao Z, Zhong C. *AIChE J*, 2022, 68: e17749
- 134 Zhou S, Shekhah O, Ramírez A, Lyu P, Abou-Hamad E, Jia J, Li J, Bhatt PM, Huang Z, Jiang H, Jin T, Maurin G, Gascon J, Eddaoudi M. *Nature*, 2022, 606: 706–712
- 135 Sun Y, Ji T, Gao Y, Yan J, He Y, Xu G, Yan F, Bian Q, Liu Y. ACS Mater Lett, 2023, 5: 558–564
- 136 Sun Y, Hu S, Yan J, Ji T, Liu L, Wu M, Guo X, Liu Y. Angew Chem Int Ed, 2023, 62: e202311336
- 137 Zhou S, Wei Y, Li L, Duan Y, Hou Q, Zhang L, Ding LX, Xue J, Wang H, Caro J. Sci Adv, 2018, 4: eaau1393

- 138 Guo X, Xue W, Sun Y, Zhang Z, Huang H, Qiao Z, Zhong C. J Mater Chem A, 2021, 9: 26045–26050
- Huang K, Li Q, Liu G, Shen J, Guan K, Jin W. ACS Appl Mater Interfaces, 2015, 7: 16157–16160
- 140 Jin H, Mo K, Wen F, Li Y. *J Membrane Sci*, 2019, 577: 129–136
- 141 Wang Y, Ban Y, Hu Z, Zhao Y, Zheng M, Yang W, Zhang T. Angew Chem Int Ed, 2022, 61: e202114479
- 142 Liu X, Li Y, Zhu G, Ban Y, Xu L, Yang W. Angew Chem Int Ed, 2011, 50: 10636–10639
- 143 Zhang W, Ying Y, Ma J, Guo X, Huang H, Liu D, Zhong C. J Membrane Sci., 2017, 527: 8–17
- 144 Xu LH, Li SH, Mao H, Li Y, Zhang AS, Wang S, Liu WM, Lv J, Wang T, Cai WW, Sang L, Xie WW, Pei C, Li ZZ, Feng YN, Zhao ZP. Science, 2022, 378: 308–313
- 145 Guo X, Liu D, Han T, Huang H, Yang Q, Zhong C. AIChE J, 2016, 63: 1303–1312
- 146 Dai R, Han H, Zhu Y, Wang X, Wang Z. Front Environ Sci Eng, 2021, 16: 40
- 147 Wang Z, Wang Z, Lin S, Jin H, Gao S, Zhu Y, Jin J. *Nat Commun*, 2018, 9: 2004
- 148 Zhang R, Ji S, Wang N, Wang L, Zhang G, Li J. Angew Chem Int Ed, 2014, 53: 9775–9779
- 149 Meng Y, Shu L, Liu L, Wu Y, Xie LH, Zhao MJ, Li JR. J Membrane Sci, 2019, 591: 117360
- 150 Cong S, Yuan Y, Wang J, Wang Z, Kapteijn F, Liu X. J Am Chem Soc, 2021, 143: 20055–20058
- 151 Xiao Y, Zhang W, Jiao Y, Xu Y, Lin H. J Membrane Sci, 2021, 624: 119101
- 152 Cai J, Song S, Zhu L, Lu Q, Lu Z, Wei Y, Wang H. Nano Res, 2023, 16: 6290–6297
- 153 Yang K, Ban Y, Guo A, Zhao M, Zhou Y, Cao N, Yang W. J Membrane Sci, 2020, 611: 118419
- 154 Yang K, Hu S, Ban Y, Zhou Y, Cao N, Zhao M, Xiao Y, Li W, Yang W. Sci Bull, 2021, 66: 1869–1876
- 155 Yan T, Sharif A, Zhang Z, Wang H, Yang J, He C, Lu J, Zhou L, He G. ACS Appl Mater Interfaces, 2024, 16: 65456–65468
- 156 Lv J, Zhou X, Yang J, Wang L, Lu J, He G, Dong Y. J Membrane Sci, 2022, 658: 120585
- 157 Liu H, Cong S, Yan X, Wang X, Gao A, Wang Z, Liu X. J Membrane Sci, 2023, 669: 121282
- 158 Ji T, Sun Y, Liu Y, Li M, Wang F, Liu L, He G, Liu Y. ACS Appl Mater Interfaces, 2020, 12: 15320–15327
- 159 Sun Y, Yan J, Gao Y, Ji T, Chen S, Wang C, Lu P, Li Y, Liu Y. Angew Chem Int Ed, 2023, 62: e202216697
- 160 Yan X, Song T, Li M, Wang Z, Liu X. Nat Commun, 2024, 15: 628
- 161 Duan S, Li D, Yang X, Niu C, Sun S, He X, Shan M, Zhang Y. J Membrane Sci, 2023, 671: 121396
- 162 Feng F, Wu J, Weber M, Zhang S, Chung TS. *J Membrane Sci*, 2024, 711: 123217
- 163 Gao A, Yan X, Cong S, Wang X, Liu H, Wang Z, Liu X. *J Membrane Sci*, 2023, 668: 121293
- 164 Cong S, Yuan Y, Wang J, Wang Z, Liu X. *AIChE J*, 2022, 69: e17983
- 165 Ding L, Wei Y, Li L, Zhang T, Wang H, Xue J, Ding LX, Wang S, Caro J, Gogotsi Y. Nat Commun, 2018, 9: 155
- 166 Wang J, Fan Y, Jiang J, Wan Z, Pang S, Guan Y, Xu H, He X, Ma Y, Huang A, Wu P. Angew Chem Int Ed. 2023, 62: e202304734
- 167 Qu K, Dai L, Xia Y, Wang Y, Zhang D, Wu Y, Yao Z, Huang K, Guo X, Xu Z. J Membrane Sci, 2021, 638: 119669
- 168 Luo M, Lu Z, Zhao Y, Wang Y, Wei Y, Wang H. AIChE J, 2023, 69: e18105
- 169 Wang Q, Fan Y, Wu C, Jin Y, Li C, Sunarso J, Meng X, Yang N. J Membrane Sci, 2022, 653: 120533
- 170 Hu L, Lee WI, Roy S, Subramanian A, Kisslinger K, Zhu L, Fan S, Hwang S, Bui VT, Tran T, Zhang G, Ding Y, Ajayan PM, Nam CY, Lin H. *Nat Commun*, 2024, 15: 5688
- 171 Han DY, Lee AH, Kang SK, Kim SW, Kwak WC, Jeon IS, Yang S, Lee PS. Chem Eng J, 2024, 479: 147435

- 172 Hu L, Bui VT, Krishnamurthy A, Fan S, Guo W, Pal S, Chen X, Zhang G, Ding Y, Singh RP, Lupion M, Lin H. Sci Adv, 2022, 8: eabl8160
- 173 Li Z, Zhang J, Zhang N, Li Z, Bao J, Zhang X, He G, Chen C, Song Y. *Carbon*, 2024, 216: 118524
- 174 Lei L, Pan F, Lindbråthen A, Zhang X, Hillestad M, Nie Y, Bai L, He X, Guiver MD. *Nat Commun*, 2021, 12: 268
- 175 Lei L, Lindbråthen A, Hillestad M, He X. *J Membrane Sci*, 2021, 627: 119241
- 176 Zhang Y, Wang H, Liu J, Hou J, Zhang Y. J Mater Chem A, 2017, 5: 19954–19962
- 177 Wang Y, Jin H, Ma Q, Mo K, Mao H, Feldhoff A, Cao X, Li Y, Pan F, Jiang Z. Angew Chem Int Ed, 2020, 59: 4365–4369
- 178 Yin H, Wang J, Xie Z, Yang J, Bai J, Lu J, Zhang Y, Yin D, Lin JYS. Chem Commun, 2014, 50: 3699–3701
- 179 Liu J, Canfield N, Liu W. Ind Eng Chem Res, 2016, 55: 3823-3832
- 180 Zhou F, Chen Y, Zhang Z, Gu Z, Sun Y, Tong M, Yang Q, Dong W, Pan Y, Qiao Z, Zhong C. AIChE J, 2024, 70: e18455
- 181 Rong R, Sun Y, Ji T, Liu Y. *J Membrane Sci*, 2020, 610: 118275
- 82 Wu W, Li Z, Chen Y, Li W. Environ Sci Technol, 2019, 53: 3764–3772
- 183 Xu X, Wang J, Dong J, Li HB, Zhang Q, Zhao X. J Membrane Sci, 2020, 602: 117967
- 184 Lu Y, Hao J, Li L, Song J, Xiao G, Zhao H, Hu Z, Wang T. React Funct Polyms, 2017, 119: 134–144
- 185 Hu X, Pang Y, Mu H, Meng X, Wang X, Wang Z, Yan J. J Membrane Sci, 2021, 620: 118825
- 186 Hou L, Wang Z, Chen Z, Chen W, Yang C. Sep Purif Tech, 2020, 242: 116766
- 187 Zhang C, Zhang W, Gao H, Bai Y, Sun Y, Chen Y. J Membrane Sci, 2017, 528: 72–81
- 188 Yang Z, Guo W, Mahurin SM, Wang S, Chen H, Cheng L, Jie K, Meyer Iii HM, Jiang D, Liu G, Jin W, Popovs I, Dai S. Chem, 2020, 6: 631–645
- 189 Yin L, Li D, Guo H, Wang S, Zhang T, Liu Y, Gai F, Zhao X. J Membrane Sci, 2022, 655: 120610
- 190 Wang Y, Sheng L, Zhang X, Li J, Wang R. J Membrane Sci, 2023, 666: 121127
- 191 Chuah CY, Lee J, Bao Y, Song J, Bae TH. J Membrane Sci, 2021, 622: 119031
- 192 Weng Y, Ji W, Ye C, Dong H, Gao Z, Li J, Luo C, Ma X. J Membrane Sci, 2022, 644: 120086
- 193 Yin L, Wang S, Shen T, Gai F, Ma Z, Liu G, Li J, Wang H. J Membrane Sci, 2025, 713: 123337
- 194 Wang K, Chen D, Tang J, Hong Z, Zhu Z, Yuan Z, Lin Z, Liu Y, Semiat R, He X. Chem Eng J, 2024, 483: 149305
- 195 Wang Y, Wang K, Zhang X, Li J. J Membrane Sci, 2023, 682: 121781
- 196 Song L, Pan M, Zhao R, Deng J, Wu Y. J Control Release, 2020, 324: 156–171
- 197 Das MC, Guo Q, He Y, Kim J, Zhao CG, Hong K, Xiang S, Zhang Z, Thomas KM, Krishna R, Chen B. J Am Chem Soc, 2012, 134: 8703– 8710
- 198 Peng Y, Gong T, Cui Y. Chem Commun, 2013, 49: 8253-8255
- 199 Peng Y, Gong T, Zhang K, Lin X, Liu Y, Jiang J, Cui Y. Nat Commun, 2014, 5: 4406
- 200 Liu J, Mukherjee S, Wang F, Fischer RA, Zhang J. Chem Soc Rev, 2021, 50: 5706–5745
- 201 Xie SM, Zhang ZJ, Wang ZY, Yuan LM. J Am Chem Soc, 2011, 133: 11892–11895
- 202 Jiang H, Yang K, Zhao X, Zhang W, Liu Y, Jiang J, Cui Y. J Am Chem Soc, 2021, 143: 390–398
- 203 Huang K, Dong X, Ren R, Jin W. *AIChE J*, 2013, 59: 4364–4372
- 204 Wang W, Dong X, Nan J, Jin W, Hu Z, Chen Y, Jiang J. Chem Commun, 2012, 48: 7022–7024
- 205 Lu Y, Zhang H, Chan JY, Ou R, Zhu H, Forsyth M, Marijanovic EM, Doherty CM, Marriott PJ, Holl MMB, Wang H. Angew Chem Int Ed,

- 2019, 58: 16928-16935
- 206 Patterson WC. Nuclear Power. London: Penguin Books, 1976
- 207 Https://www.world-nuclear.org/our-association/publications/global-trends-reports/nuclear-fuel-report.Aspx
- 208 Xie Y, Liu Z, Geng Y, Li H, Wang N, Song Y, Wang X, Chen J, Wang J, Ma S, Ye G. Chem Soc Rev, 2023, 52: 97–162
- 209 Boyarintsev AV, Stepanov SI, Kostikova GV, Zhilov VI, Safiulina AM, Tsivadze AY. Nucl Eng Tech, 2023, 55: 391–407
- 210 Ruhela R, Singh AK, Tomar BS, Hubli RC. RSC Adv, 2014, 4: 24344–24350
- 211 Fontaine JP, Pointurier F, Blanchard X, Taffary T. *J Environ Radioact*, 2004, 72: 129–135
- 212 Franks NP, Dickinson R, de Sousa SLM, Hall AC, Lieb WR. *Nature*, 1998, 396: 324
- 213 Driehuys B. Science, 2006, 314: 432-433
- 214 He H, Hashemi L, Hu ML, Morsali A. Coord Chem Rev, 2018, 376: 319–347
- 215 Wang Y, Liu Z, Li Y, Bai Z, Liu W, Wang Y, Xu X, Xiao C, Sheng D, Diwu J, Su J, Chai Z, Albrecht-Schmitt TE, Wang S. J Am Chem Soc, 2015, 137: 6144–6147
- 216 Feng L, Chen X, Cao M, Zhao S, Wang H, Chen D, Ma Y, Liu T, Wang N, Yuan Y. *Angew Chem Int Ed*, 2023, 62: e202312894
- 217 Xu H, Cao C, Hu H, Wang S, Liu J, Cheng P, Kaltsoyannis N, Li J, Zhao B. *Angew Chem Int Ed*, 2019, 58: 6022–6027
- 218 Ouyang H, Chen N, Chang G, Zhao X, Sun Y, Chen S, Zhang H, Yang D. Angew Chem Int Ed, 2018, 57: 13197–13201
- 219 Ma W, Lv TT, Tang JH, Feng ML, Huang XY. JACS Au, 2022, 2: 492–501
- 220 Zhang J, Chen L, Dai X, Zhu L, Xiao C, Xu L, Zhang Z, Alekseev EV, Wang Y, Zhang C, Zhang H, Wang Y, Diwu J, Chai Z, Wang S. Chem, 2019, 5: 977–994
- 221 Sheng D, Zhu L, Dai X, Xu C, Li P, Pearce CI, Xiao C, Chen J, Zhou R, Duan T, Farha OK, Chai Z, Wang S. Angew Chem Int Ed, 2019, 58: 4968–4972
- 222 Sheng D, Zhu L, Xu C, Xiao C, Wang Y, Wang Y, Chen L, Diwu J, Chen J, Chai Z, Albrecht-Schmitt TE, Wang S. *Environ Sci Technol*, 2017, 51: 3471–3479
- 223 Zhu L, Sheng D, Xu C, Dai X, Silver MA, Li J, Li P, Wang Y, Wang Y, Chen L, Xiao C, Chen J, Zhou R, Zhang C, Farha OK, Chai Z, Albrecht-Schmitt TE, Wang S. J Am Chem Soc, 2017, 139: 14873–14876.
- 224 Shen N, Yang Z, Liu S, Dai X, Xiao C, Taylor-Pashow K, Li D, Yang C, Li J, Zhang Y, Zhang M, Zhou R, Chai Z, Wang S. Nat Commun, 2020, 11: 5571
- 225 Chen L, Bai Z, Zhu L, Zhang L, Cai Y, Li Y, Liu W, Wang Y, Chen L, Diwu J, Wang J, Chai Z, Wang S. ACS Appl Mater Interfaces, 2017, 9: 32446–32451
- 226 Carboni M, Abney CW, Liu S, Lin W. Chem Sci, 2013, 4: 2396– 2402
- 227 Bai ZQ, Yuan LY, Zhu L, Liu ZR, Chu SQ, Zheng LR, Zhang J, Chai ZF, Shi WQ. J Mater Chem A, 2015, 3: 525–534
- 228 Qin X, Yang W, Yang Y, Gu D, Guo D, Pan Q. *Inorg Chem*, 2020, 59: 9857–9865
- 229 Zhao WW, Li LH, Liao JZ, Liang RP, Song AM, Zhang FD, Ke H, Qiu JD. *Chem Eng J*, 2022, 433: 133787
- 230 Zhao B, Yuan L, Wang Y, Duan T, Shi W. ACS Appl Mater Interfaces, 2021, 13: 16300–16308
- 231 Zhang N, Yuan LY, Guo WL, Luo SZ, Chai ZF, Shi WQ. ACS Appl Mater Interfaces, 2017, 9: 25216–25224
- 232 Guo XG, Su J, Xie WQ, Ni SN, Gao Y, Su X, Sun XQ. *Dalton Trans*, 2020, 49: 4060–4066
- 233 Chen X, Liu X, Xiao S, Xue W, Zhao X, Yang Q. Sep Purif Tech, 2022, 297: 121517
- 234 Wu J, Zhang Y, Zhou J, Cao R, Wang C, Li J, Song Y. *J Radioanal Nucl Chem*, 2021, 328: 769–783
- 235 Aguila B, Banerjee D, Nie Z, Shin Y, Ma S, Thallapally PK. *Chem Commun*, 2016, 52: 5940–5942

- 236 Guo C, Yuan M, He L, Cheng L, Wang X, Shen N, Ma F, Huang G, Wang S. *CrystEngComm*, 2021, 23: 3349–3355
- 237 Daliran S, Ghazagh-Miri M, Oveisi AR, Khajeh M, Navalón S, Âlvaro M, Ghaffari-Moghaddam M, Samareh Delarami H, García H. ACS Appl Mater Interfaces, 2020, 12: 25221–25232
- 238 Tang J, Chen Y, Wang S, Kong D, Zhang L. *Environ Res*, 2022, 210: 112870
- 239 Zha M, Liu J, Wong YL, Xu Z. J Mater Chem A, 2015, 3: 3928–3934
- 240 Sengupta S, Sahoo M, Sravani VV, Sreenivasulu B, Rao CVSB, Suresh A. New J Chem, 2023, 47: 14921–14932
- 241 Banerjee D, Cairns AJ, Liu J, Motkuri RK, Nune SK, Fernandez CA, Krishna R, Strachan DM, Thallapally PK. Acc Chem Res, 2015, 48: 211–219
- 242 Lai C, Wang Z, Qin L, Fu Y, Li B, Zhang M, Liu S, Li L, Yi H, Liu X, Zhou X, An N, An Z, Shi X, Feng C. *Coord Chem Rev*, 2021, 427: 213565
- 243 Li L, Guo L, Zhang Z, Yang Q, Yang Y, Bao Z, Ren Q, Li J. J Am Chem Soc, 2019, 141: 9358–9364
- 244 Simon CM, Mercado R, Schnell SK, Smit B, Haranczyk M. Chem Mater, 2015, 27: 4459–4475
- 245 Gu C, Yu Z, Liu J, Sholl DS. ACS Appl Mater Interfaces, 2021, 13: 11039–11049
- 246 Wang X, Ma F, Liu S, Chen L, Xiong S, Dai X, Tai B, He L, Yuan M, Mi P, Gong S, Li G, Tao Y, Wan J, Chen L, Sun X, Tang Q, He L, Yang Z, Chai Z, Wang S. J Am Chem Soc, 2022, 144: 13634–13642
- 247 Zadehahmadi F, Eden NT, Mahdavi H, Konstas K, Mardel JI, Shaibani M, Banerjee PC, Hill MR. *Environ Sci-Water Res Technol*, 2023, 9: 1305–1330
- 248 Sun Q, Qin L, Lai C, Liu S, Chen W, Xu F, Ma D, Li Y, Qian S, Chen Z, Chen W, Ye H. J Hazard Mater, 2023, 447: 130848
- 249 Li W, Li J, Duong TD, Sapchenko SA, Han X, Humby JD, White-head GFS, Victórica-Yrezábal IJ, da Silva I, Manuel P, Frogley MD, Cinque G, Schröder M, Yang S. *J Am Chem Soc*, 2022, 144: 13196–13204
- 250 McKinlay AC, Eubank JF, Wuttke S, Xiao B, Wheatley PS, Bazin P, Lavalley JC, Daturi M, Vimont A, De Weireld G, Horcajada P, Serre C, Morris RE. *Chem Mater*, 2013, 25: 1592–1599
- 251 Xiong XH, Wei ZW, Wang W, Meng LL, Su CY. J Am Chem Soc, 2023, 145: 14354–14364
- 252 Mercuri G, Moroni M, Galli S, Tuci G, Giambastiani G, Yan T, Liu D, Rossin A. ACS Appl Mater Interfaces, 2021, 13: 58982–58993
- 253 Bian Y, Chen C, Wang R, Wang S, Pan Y, Zhao B, Chen C, Zhang L. Appl Mater Today, 2020, 20: 100653
- 254 He T, Kong XJ, Bian ZX, Zhang YZ, Si GR, Xie LH, Wu XQ, Huang H, Chang Z, Bu XH, Zaworotko MJ, Nie ZR, Li JR. Nat Mater, 2022, 21: 689–695
- 255 Li GP, Zhang K, Zhang PF, Liu WN, Tong WQ, Hou L, Wang YY. *Inorg Chem*, 2019, 58: 3409–3415
- 256 Huo JB, Xu L, Yang JCE, Cui HJ, Yuan B, Fu ML. Colloids Surfs A-Physicochem Eng Aspects, 2018, 539: 59–68
- 257 Lv J, Chen Q, Liu JH, Yang HS, Wang P, Yu J, Xie Y, Wu YF, Li JR. *Inorg Chem*, 2021, 60: 1814–1822
- 258 Yang Y, Jiang F, Liu C, Chen L, Gai Y, Pang J, Su K, Wan X, Hong M. Cryst Growth Des, 2016, 16: 2266–2276
- 259 Li B, Chen X, Hu P, Kirchon A, Zhao YM, Pang J, Zhang T, Zhou HC. ACS Appl Mater Interfaces, 2019, 11: 8227–8233
- 260 Li J, Yuan S, Qin JS, Huang L, Bose R, Pang J, Zhang P, Xiao Z, Tan K, Malko AV, Cagin T, Zhou HC. ACS Appl Mater Interfaces, 2020, 12: 26727–26732
- 261 Hao J, Lang F, Hao L, Yang Y, Zhang L, Zhang H, Li QW, Pang J, Bu XH. *Chin Chem Lett*, 2023, 34: 108310
- 262 Li X, Jiang F, Chen L, Wu M, Lu S, Pang J, Zhou K, Chen X, Hong M. CrystEngComm, 2016, 18: 2239–2243
- 263 Zeng L, Wang XY, Li N, Pang J, Bu XH. Coord Chem Rev, 2024, 511: 215868
- 264 Zhang B, Li XW, Fang H, Li CT, Yu SJ, Yu MH, Chang Z, Bu XH. Sci China Chem, 2024, 67: 4175–4183

- 265 Cui Y, Zhang J, He H, Qian G. Chem Soc Rev, 2018, 47: 5740–5785
- 266 Cui Y, Yue Y, Qian G, Chen B. Chem Rev, 2012, 112: 1126-1162
- 267 Zheng HQ, Zhang L, Lu M, Xiao X, Yang Y, Cui Y, Qian G. Research, 2022, 2022: 2022/9869510
- 268 Jiang Z, Zheng HQ, Guan L, Yang Y, Cui Y, Qian G. J Mater Chem C, 2022, 10: 10473–10479
- 269 Pan M, Liao WM, Yin SY, Sun SS, Su CY. Chem Rev, 2018, 118: 8889–8935
- 270 Zheng HQ, Yang Y, Wang Z, Yang D, Qian G, Cui Y. Adv Mater, 2023. 35: e2300177
- 271 Zheng HQ, Cui Y, Qian G. Acc Mater Res, 2023, 4: 982–994
- 272 Cui Y, Song T, Yu J, Yang Y, Wang Z, Qian G. Adv Funct Mater, 2015, 25: 4796–4802
- 273 Wen Y, Sheng T, Zhu X, Zhuo C, Su S, Li H, Hu S, Zhu QL, Wu X. Adv Mater, 2017, 29: 1700778
- 274 Liu XY, Xing K, Li Y, Tsung CK, Li J. J Am Chem Soc, 2019, 141: 14807–14813
- 275 Tang Y, Xia T, Song T, Cui Y, Yang Y, Qian G. Adv Opt Mater, 2018, 6: 1800968
- 276 Tang Y, Cao W, Yao L, Cui Y, Yu Y, Qian G. J Mater Chem C, 2020, 8: 12308–12313
- 277 Chen Y, Yu B, Cui Y, Xu S, Gong J. Chem Mater, 2019, 31: 1289– 1295
- 278 Wang Z, Zhu C, Mo J, Fu P, Zhao Y, Yin S, Jiang J, Pan M, Su C. Angew Chem Int Ed, 2019, 58: 9752–9757
- 279 Ren J, Zhou X, Wang Y. *Chem Eng J*, 2020, 391: 123622
- 280 Peng C, Song X, Yin J, Zhang G, Fei H. Angew Chem Int Ed, 2019, 58: 7818–7822
- 281 Cui Y, Xu H, Yue Y, Guo Z, Yu J, Chen Z, Gao J, Yang Y, Qian G, Chen B. J Am Chem Soc, 2012, 134: 3979–3982
- 282 Zhao D, Yue D, Jiang K, Zhang L, Li C, Qian G. *Inorg Chem*, 2019, 58: 2637–2644
- 283 Xia T, Shao Z, Yan X, Liu M, Yu L, Wan Y, Chang D, Zhang J, Zhao D. *Chem Commun*, 2021, 57: 3143–3146
- 284 Cui Y, Song R, Yu J, Liu M, Wang Z, Wu C, Yang Y, Wang Z, Chen B, Qian G. Adv Mater, 2015, 27: 1420–1425
- 285 Cao W, Cui Y, Yang Y, Qian G. ACS Mater Lett, 2021, 3: 1426– 1432
- Wang S, Gong M, Han X, Zhao D, Liu J, Lu Y, Li C, Chen B. ACS Appl Mater Interfaces, 2021, 13: 11078–11088
- 287 Cai H, Lu W, Yang C, Zhang M, Li M, Che C, Li D. Adv Opt Mater, 2019, 7: 1801149
- 288 Yang X, Zou H, Sun X, Sun T, Guo C, Fu Y, Wu CL, Qiao X, Wang F. *Adv Opt Mater*, 2019, 7: 1900336
- 289 Feng T, Ye Y, Liu X, Cui H, Li Z, Zhang Y, Liang B, Li H, Chen B. Angew Chem Int Ed, 2020, 59: 21752–21757
- 290 Ding Y, Lu Y, Yu K, Wang S, Zhao D, Chen B. Adv Opt Mater, 2021, 9: 2100945
- 291 Zheng HQ, Zhang L, Cui Y, Qian G. Adv Photon, 2023, 5: 054001
- 292 Zhang X, Fang L, Jiang K, He H, Yang Y, Cui Y, Li B, Qian G. Biosens Bioelectron, 2019, 130: 65–72
- 293 Zhang M, Feng G, Song Z, Zhou YP, Chao HY, Yuan D, Tan TTY, Guo Z, Hu Z, Tang BZ, Liu B, Zhao D. J Am Chem Soc, 2014, 136: 7241–7244
- 294 Li Z, Jiang F, Yu M, Li S, Chen L, Hong M. Nat Commun, 2022, 13: 2142
- 295 Pang J, Yao Z, Zhang K, Li Q, Fu Z, Zheng R, Li W, Xu J, Bu X. Angew Chem Int Ed, 2023, 62: e202217456
- 296 Li W, Wu Y, Zhong X, Chen X, Liang G, Ye J, Mo Z, Chen X. Angew Chem Int Ed, 2023, 62: e202303500
- 297 Liu CY, Chen XR, Chen HX, Niu Z, Hirao H, Braunstein P, Lang JP. J Am Chem Soc, 2020, 142: 6690–6697
- 298 Dou Z, Yu J, Cui Y, Yang Y, Wang Z, Yang D, Qian G. J Am Chem Soc, 2014, 136: 5527–5530
- 299 Zhang X, Zhang Q, Yue D, Zhang J, Wang J, Li B, Yang Y, Cui Y, Qian G. Small, 2018, 14: 1801563
- 300 Zhang J, Liu F, Gan J, Cui Y, Li B, Yang Y, Qian G. Sci China

- Mater, 2019, 62: 1445-1453
- 301 Wu S, Min H, Shi W, Cheng P. Adv Mater, 2020, 32: 1805871
- 302 Chen B, Xiang S, Qian G. Acc Chem Res, 2010, 43: 1115-1124
- 303 Hu Z, Deibert BJ, Li J. Chem Soc Rev, 2014, 43: 5815-5840
- 304 Yang Y, Jiang F, Chen L, Pang J, Wu M, Wan X, Pan J, Qian J, Hong M. J Mater Chem A, 2015, 3: 13526–13532
- 305 Yang Y, Chen L, Jiang F, Wu M, Pang J, Wan X, Hong M. CrystEngComm, 2019, 21: 321–328
- 306 Yang Y, Pang J, Li Y, Sun L, Zhang H, Zhang L, Xu S, Jiang T. Inorg Chem. 2021, 60: 19189–19196
- 307 Wang XN, Zhao Y, Li JL, Pang JD, Wang Q, Li B, Zhou HC. *Dalton Trans*, 2021, 50: 3854–3861
- 308 Wan XY, Jiang FL, Chen L, Pan J, Zhou K, Su KZ, Pang JD, Lyu GX, Hong MC. CrystEngComm, 2015, 17: 3829–3837
- 309 Gao X, Chen N, Cao M, Shi Y, Zhang Q. Chin J Struct Chem, 2022, 41: 2211110–2211116
- 310 Liu PD, Liu AG, Wang PM, Chen Y, Bao Li Y. Chin J Struct Chem, 2023, 42: 100001
- 311 Xu S, Pang J, Zhang B, Li Y, Yang Y, Li J. *Cryst Growth Des*, 2024, 24: 1410–1420
- 312 Li D, Wang X, Zhu C, Meng Z, Zhang L, Yuan G. Chin J Struct Chem, 2023, 42: 100094
- 313 Hao JN, Niu D, Gu J, Lin S, Li Y, Shi J. Adv Mater, 2020, 32: 2000791
- 314 Wu S, Lin Y, Liu J, Shi W, Yang G, Cheng P. *Adv Funct Mater*, 2018, 28: 1707169
- 315 Hao J, Li Y. Adv Funct Mater, 2019, 29: 1903058
- 316 Xu S, Zhang B, Li Y, Yang Y, Li J, Pang J. *Inorg Chem*, 2023, 62: 11168–11178
- 317 Ji W, Wang G, Wang B, Yan B, Liu L, Xu L, Ma T, Yao S, Fu Y, Zhang L, Zhai Q. *Chin J Struct Chem*, 2023, 42: 100062
- 318 Han Z, Wang K, Guo Y, Chen W, Zhang J, Zhang X, Siligardi G, Yang S, Zhou Z, Sun P, Shi W, Cheng P. Nat Commun, 2019, 10: 5117
- 319 Han Z, Wang K, Min H, Xu J, Shi W, Cheng P. Angew Chem Int Ed, 2022, 61: e202204066
- 320 Wang B, Wang P, Xie LH, Lin RB, Lv J, Li JR, Chen B. Nat Commun, 2019, 10: 3861
- 321 Xian JY, Huang ZY, Xie XX, Lin CJ, Zhang XJ, Song HY, Zheng SR. Chin J Struct Chem, 2023, 42: 100005
- 322 Guan L, Jiang Z, Cui Y, Yang Y, Yang D, Qian G. Adv Opt Mater, 2021, 9: 2002180
- 323 Wang G, Liao Z, Jiang Z, Cao W, Yang Y, Qian G, Cui Y. J Mater Chem C, 2023, 11: 14551–14558
- 324 Wang J, Li D, Ye Y, Qiu Y, Liu J, Huang L, Liang B, Chen B. Adv Mater, 2021, 33: 2008020
- 325 Bavykina A, Kolobov N, Khan IS, Bau JA, Ramirez A, Gascon J. Chem Rev, 2020, 120: 8468–8535
- 326 Wang Y, Liu ZX, Zhao XP, Ma YY, Zhang SM, Cui WJ, Du J, Han ZG. *Chin J Struct Chem*, 2023, 42: 100011
- 327 Li HY, Kong XJ, Han SD, Pang J, He T, Wang GM, Bu XH. Chem Soc Rev, 2024, 53: 5626–5676
- 328 Zhang MJ, Ge Y, Cao C, Xue XR, Li QY, Liu Q, Lang JP. Chin J Struct Chem, 2023, 42: 100125
- 329 Cavka JH, Jakobsen S, Olsbye U, Guillou N, Lamberti C, Bordiga S, Lillerud KP. J Am Chem Soc, 2008, 130: 13850–13851
- 330 Fei H, Cohen SM. Chem Commun, 2014, 50: 4810-4812
- 331 Wang Z, Heising JM, Clearfield A. J Am Chem Soc, 2003, 125: 10375–10383
- 332 Jiang J, Gándara F, Zhang YB, Na K, Yaghi OM, Klemperer WG. J Am Chem Soc, 2014, 136: 12844–12847
- 333 Nguyen LHT, Nguyen TT, Nguyen HL, Doan TLH, Tran PH. Catal Sci Technol, 2017, 7: 4346–4350
- 334 Qi C, Ramella D, Wensley AM, Luan Y. Adv Synth Catal, 2016, 358: 2604–2611
- 335 Mortazavi S, Abbasi A, Masteri-Farahani M, Farzaneh F. ChemistrySelect, 2019, 4: 7495–7501

- 336 Li B, Leng K, Zhang Y, Dynes JJ, Wang J, Hu Y, Ma D, Shi Z, Zhu L, Zhang D, Sun Y, Chrzanowski M, Ma S. *J Am Chem Soc*, 2015, 137: 4243–4248
- 337 Seo JS, Whang D, Lee H, Jun SI, Oh J, Jeon YJ, Kim K. *Nature*, 2000, 404: 982–986
- 338 Zhou Q L, Xie J H. Chiral Spiro Catalysts. Berlin, Heidelberg: Springer, 2011. 1–28
- 339 Wu CD, Hu A, Zhang L, Lin W. J Am Chem Soc, 2005, 127: 8940– 8941
- 340 Falkowski JM, Sawano T, Zhang T, Tsun G, Chen Y, Lockard JV, Lin W. J Am Chem Soc. 2014, 136: 5213–5216
- 341 Mo K, Yang Y, Cui Y. J Am Chem Soc, 2014, 136: 1746–1749
- 342 Chen X, Jiang H, Hou B, Gong W, Liu Y, Cui Y. J Am Chem Soc, 2017, 139: 13476–13482
- 343 Zhu C, Yuan G, Chen X, Yang Z, Cui Y. J Am Chem Soc, 2012, 134: 8058–8061
- 344 Xuan W, Ye C, Zhang M, Chen Z, Cui Y. *Chem Sci*, 2013, 4: 3154–3159
- 345 Yang Z, Zhu C, Li Z, Liu Y, Liu G, Cui Y. Chem Commun, 2014, 50: 8775–8778
- 346 Xi W, Liu Y, Xia Q, Li Z, Cui Y. Chem Eur J, 2015, 21: 12581– 12585
- 347 Xia Q, Liu Y, Li Z, Gong W, Cui Y. *Chem Commun*, 2016, 52: 13167–13170
- 348 Liu Y, Li Z, Yuan G, Xia Q, Yuan C, Cui Y. *Inorg Chem*, 2016, 55: 12500–12503
- 349 Zhu C, Xia Q, Chen X, Liu Y, Du X, Cui Y. ACS Catal, 2016, 6: 7590–7596
- 350 Xia Q, Li Z, Tan C, Liu Y, Gong W, Cui Y. J Am Chem Soc, 2017, 139: 8259–8266
- 351 Chen X, Jiang H, Li X, Hou B, Gong W, Wu X, Han X, Zheng F, Liu Y, Jiang J, Cui Y. Angew Chem Int Ed, 2019, 58: 14748–14757
- 352 Gong W, Chen X, Jiang H, Chu D, Cui Y, Liu Y. J Am Chem Soc, 2019, 141: 7498–7508
- 353 Fang R, Dhakshinamoorthy A, Li Y, Garcia H. *Chem Soc Rev*, 2020, 49: 3638–3687
- 354 Akiyama G, Matsuda R, Sato H, Takata M, Kitagawa S. Adv Mater, 2011, 23: 3294–3297
- 355 Zi G, Yan Z, Wang Y, Chen Y, Guo Y, Yuan F, Gao W, Wang Y, Wang J. *Carbohydr Polyms*, 2015, 115: 146–151
- 356 Lu X, Wang L, Lu X. Catal Commun, 2018, 110: 23-27
- 357 Feng L, Pang J, She P, Li JL, Qin JS, Du DY, Zhou HC. Adv Mater, 2020, 32: e2004414
- 358 Cirujano FG, Corma A, Llabrés i Xamena FX. Chem Eng Sci, 2015, 124: 52–60
- 359 Rojas-Buzo S, García-García P, Corma A. ChemSusChem, 2018, 11: 432–438
- 360 Su Y, Chang G, Zhang Z, Xing H, Su B, Yang Q, Ren Q, Yang Y, Bao Z. AIChE J, 2016, 62: 4403–4417
- 361 Herbst A, Janiak C. New J Chem, 2016, 40: 7958-7967
- 362 Scott V, Gilfillan S, Markusson N, Chalmers H, Haszeldine RS. Nat Clim Change, 2012, 3: 105–111
- 363 Sakakura T, Choi JC, Yasuda H. *Chem Rev*, 2007, 107: 2365–2387
- 364 Chen Y, Luo R, Ren Q, Zhou X, Ji H. Ind Eng Chem Res, 2020, 59: 20269–20277
- 365 Pal TK, De D, Bharadwaj PK. Coord Chem Rev, 2020, 408: 213173
- 366 Guillerm V, Weseliński ŁJ, Belmabkhout Y, Cairns AJ, D'Elia V, Wojtas Ł, Adil K, Eddaoudi M. Nat Chem, 2014, 6: 673–680
- 367 Zou R, Li P, Zeng Y, Liu J, Zhao R, Duan H, Luo Z, Wang J, Zou R, Zhao Y. Small, 2016, 12: 2334–2343
- 368 Beyzavi H, Klet RC, Tussupbayev S, Borycz J, Vermeulen NA, Cramer CJ, Stoddart JF, Hupp JT, Farha OK. J Am Chem Soc, 2014, 136: 15861–15864
- 369 Cho HY, Yang DA, Kim J, Jeong SY, Ahn WS. Catal Today, 2012, 185: 35–40
- 370 Gao W, Chen Y, Niu Y, Williams K, Cash L, Perez PJ, Wojtas L, Cai J, Chen Y, Ma S. *Angew Chem Int Ed*, 2014, 53: 2615–2619

- 371 Feng D, Chung WC, Wei Z, Gu ZY, Jiang HL, Chen YP, Darensbourg DJ, Zhou HC. *J Am Chem Soc*, 2013, 135: 17105–17110
- 372 Ren Y, Shi Y, Chen J, Yang S, Qi C, Jiang H. *RSC Adv*, 2013, 3: 2167
- 373 Lescouet T, Chizallet C, Farrusseng D. *ChemCatChem*, 2012, 4: 1725–1728
- Wang Y, Feng L, Pang J, Li J, Huang N, Day GS, Cheng L, Drake HF, Wang Y, Lollar C, Qin J, Gu Z, Lu T, Yuan S, Zhou H. Adv Sci, 2019. 6: 1802059
- 375 Zhang Y, Pang J, Li J, Yang X, Feng M, Cai P, Zhou HC. Chem Sci, 2019, 10: 8455–8460
- 376 Cai P, Xu M, Meng S, Lin Z, Yan T, Drake HF, Zhang P, Pang J, Gu Z, Zhou H. *Angew Chem Int Ed*, 2021, 60: 27258–27263
- 377 Zhang H, Li C, Li Y, Pang J, Bu X. Catalysts, 2022, 12: 1350
- 378 Li J, Speyer G, Sankey OF. Phys Rev Lett, 2004, 93: 248302
- 379 Huynh MHV, Meyer TJ. Chem Rev, 2007, 107: 5004-5064
- 380 Pannwitz A, Wenger OS. Chem Commun, 2019, 55: 4004-4014
- 381 Albero J, Peng Y, García H. ACS Catal, 2020, 10: 5734–5749
- 382 Fu J, Jiang K, Qiu X, Yu J, Liu M. Mater Today, 2020, 32: 222-243
- 383 Dhakshinamoorthy A, Li Z, Garcia H. Chem Soc Rev, 2018, 47: 8134–8172
- 384 Younis SA, Kwon EE, Qasim M, Kim KH, Kim T, Kukkar D, Dou X, Ali I. Prog Energy Combust Sci, 2020, 81: 100870
- 385 Fuhrhop J. Angew Chem Int Ed Engl, 1974, 13: 321-335
- 386 Li C, Zhang J, Song J, Xie Y, Jiang J. Sci China Chem, 2018, 61: 511–514
- 387 Xu HQ, Hu J, Wang D, Li Z, Zhang Q, Luo Y, Yu SH, Jiang HL. J Am Chem Soc, 2015, 137: 13440–13443
- 388 Zhang H, Wei J, Dong J, Liu G, Shi L, An P, Zhao G, Kong J, Wang X, Meng X, Zhang J, Ye J. Angew Chem Int Ed, 2016, 55: 14310–14314
- 389 Huang Q, Liu J, Feng L, Wang Q, Guan W, Dong LZ, Zhang L, Yan LK, Lan YQ, Zhou HC. Natl Sci Rev, 2020, 7: 53–63
- 390 Cheng XM, Dao XY, Wang SQ, Zhao J, Sun WY. ACS Catal, 2021, 11: 650–658
- 391 Chen D, Xing H, Wang C, Su Z. *J Mater Chem A*, 2016, 4: 2657–
- 392 Yan ZH, Du MH, Liu J, Jin S, Wang C, Zhuang GL, Kong XJ, Long LS, Zheng LS. Nat Commun, 2018, 9: 3353
- 393 Zhuo TC, Song Y, Zhuang GL, Chang LP, Yao S, Zhang W, Wang Y, Wang P, Lin W, Lu TB, Zhang ZM. J Am Chem Soc, 2021, 143: 6114–6122
- 394 Li N, Liu J, Liu J, Dong L, Xin Z, Teng Y, Lan Y. Angew Chem Int Ed, 2019, 58: 5226–5231
- 395 Ming MT, Wang YC, Tao WX, Shi WJ, Zhong DC, Lu TB. Green Chem, 2023, 25: 6207–6211
- 396 Li J, Huang H, Xue W, Sun K, Song X, Wu C, Nie L, Li Y, Liu C, Pan Y, Jiang HL, Mei D, Zhong C. Nat Catal, 2021, 4: 719–729
- 397 Wang S, Yao W, Lin J, Ding Z, Wang X. Angew Chem Int Ed, 2014, 53: 1034–1038
- 398 Yang W, Wang H, Liu R, Wang J, Zhang C, Li C, Zhong D, Lu T. Angew Chem Int Ed, 2021, 60: 409–414
- 399 Ye L, Gao Y, Cao S, Chen H, Yao Y, Hou J, Sun L. Appl Catal B-Environ, 2018, 227: 54–60
- 400 Xu R, Si DH, Zhao SS, Wu QJ, Wang XS, Liu TF, Zhao H, Cao R, Huang YB. *J Am Chem Soc*, 2023, 145: 8261–8270
- 401 Zhao C, Pan X, Wang Z, Wang CC. Chem Eng J, 2021, 417: 128022
- 402 Zhao Z, Zheng D, Guo M, Yu J, Zhang S, Zhang Z, Chen Y. Angew Chem Int Ed, 2022, 61: e202200261
- 403 Jiang Z, Xu X, Ma Y, Cho HS, Ding D, Wang C, Wu J, Oleynikov P, Jia M, Cheng J, Zhou Y, Terasaki O, Peng T, Zan L, Deng H. *Nature*, 2020, 586: 549–554
- 404 Kong ZC, Liao JF, Dong YJ, Xu YF, Chen HY, Kuang DB, Su CY.
 ACS Energy Lett, 2018, 3: 2656–2662
- 405 Wu L, Mu Y, Guo X, Zhang W, Zhang Z, Zhang M, Lu T. Angew Chem Int Ed, 2019, 58: 9491–9495
- 406 Zhang JH, Yang W, Zhang M, Wang HJ, Si R, Zhong DC, Lu TB.

- Nano Energy, 2021, 80: 105542
- 407 Gong YN, Shao BZ, Mei JH, Yang W, Zhong DC, Lu TB. *Nano Res*, 2022, 15: 551–556
- 408 Preethi V, Kanmani S. Mater Sci Semicon Proc, 2013, 16: 561-575
- 409 Teets TS, Nocera DG. Chem Commun, 2011, 47: 9268-9274
- 410 Lai GQ, Jiang Z, Zhong H, Chung LH, Li N, He J. Chin J Struct Chem, 2023, 42: 100090
- 411 Zhang X, Li Z, Li H, Yang D, Ren Z, Zhang Y, Zhang J, Bu X-. Angew Chem Int Ed, 2024, 63: e202404386
- 412 Shi Y, Yang AF, Cao CS, Zhao B. *Coord Chem Rev*, 2019, 390: 50–75
- 413 Shi J, Chen F, Hou L, Li G, Li Y, Guan X, Liu H, Guo L. *Appl Catal B-Environ*, 2021, 280: 119385
- 414 Han S, Pan D, Chen H, Bu X, Gao Y, Gao H, Tian Y, Li G, Wang G, Cao S, Wan C, Guo G. Angew Chem Int Ed, 2018, 57: 9864–9869
- 415 Zhao J, Wang Y, Zhou J, Qi P, Li S, Zhang K, Feng X, Wang B, Hu C. J Mater Chem A, 2016, 4: 7174–7177
- 416 Leng F, Liu H, Ding M, Lin QP, Jiang HL. ACS Catal, 2018, 8: 4583–4590
- 417 Yang S, Pattengale B, Kovrigin EL, Huang J. ACS Energy Lett, 2017, 2: 75–80
- 418 Shi D, Zheng R, Sun M, Cao X, Sun C, Cui C, Liu C, Zhao J, Du M. Angew Chem Int Ed, 2017, 56: 14637–14641
- 419 Liu W, Zhang S, Wu B, Gong X, Shao J, Wang S, Tian J. ACS Appl Nano Mater, 2023, 6: 16826–16836
- 420 An Y, Liu Y, Bian H, Wang Z, Wang P, Zheng Z, Dai Y, Whangbo MH, Huang B. Sci Bull, 2019, 64: 1502–1509
- 421 Huang G, Yang L, Yin Q, Fang Z, Hu X, Zhang A, Jiang J, Liu T, Cao R. *Angew Chem Int Ed*, 2020, 59: 4385–4390
- 422 Zhu QL, Li J, Xu Q. J Am Chem Soc, 2013, 135: 10210-10213
- 423 Shen L, Luo M, Huang L, Feng P, Wu L. *Inorg Chem*, 2015, 54: 1191–1193
- 424 Xiao J, Han L, Luo J, Yu S, Jiang H. Angew Chem Int Ed, 2018, 57: 1103–1107
- 425 Li D, Yu SH, Jiang HL. Adv Mater, 2018, 30: 1707377
- 426 Dabhane H, Ghotekar S, Tambade P, Pansambal S, Murthy HCA, Oza R, Medhane V. Environ Chem Ecotox, 2021, 3: 209–219
- 427 Zhou JJ, Wang R, Liu XL, Peng FM, Li CH, Teng F, Yuan YP. Appl Surf Sci, 2015, 346: 278–283
- 428 Xu HQ, Yang S, Ma X, Huang J, Jiang HL. ACS Catal, 2018, 8: 11615–11621
- 429 Tian L, Yang X, Liu Q, Qu F, Tang H. *Appl Surf Sci*, 2018, 455: 403–409
- 430 Pan Y, Li D, Jiang H. Chem Eur J, 2018, 24: 18403-18407
- 431 Zhang H, Sun R, Li D C, Dou J M. Chin J Struct Chem, 2022, 41: 2211071–2211083
- 432 Qiao G, Yuan S, Pang J, Rao H, Lollar CT, Dang D, Qin J, Zhou H, Yu J. Angew Chem Int Ed, 2020, 59: 18224–18228
- 433 Sun D, Ye L, Li Z. Appl Catal B-Environ, 2015, 164: 428-432
- 434 Long J, Wang S, Ding Z, Wang S, Zhou Y, Huang L, Wang X. Chem Commun, 2012, 48: 11656–11658
- 435 Ji G, Zhao L, Wang Y, Tang Y, He C, Liu S, Duan C. ACS Catal, 2022, 12: 7821–7832
- 436 Xie MH, Yang XL, Zou C, Wu CD. *Inorg Chem*, 2011, 50: 5318–5320
- 437 Wang C, Xie Z, deKrafft KE, Lin W. J Am Chem Soc, 2011, 133: 13445–13454
- 438 Nasalevich MA, Goesten MG, Savenije TJ, Kapteijn F, Gascon J. Chem Commun, 2013, 49: 10575–10577
- 439 He C, Liang J, Zou YH, Yi JD, Huang YB, Cao R. Natl Sci Rev, 2022, 9: nwab157
- 440 Wu P, He C, Wang J, Peng X, Li X, An Y, Duan C. J Am Chem Soc, 2012, 134: 14991–14999
- 441 Shi D, He C, Qi B, Chen C, Niu J, Duan C. Chem Sci, 2015, 6: 1035– 1042
- 442 Lu G, Li S, Guo Z, Farha OK, Hauser BG, Qi X, Wang Y, Wang X, Han S, Liu X, DuChene JS, Zhang H, Zhang Q, Chen X, Ma J, Loo

- SCJ, Wei WD, Yang Y, Hupp JT, Huo F. Nat Chem, 2012, 4: 310-316
- 443 Chen L, Peng Y, Wang H, Gu Z, Duan C. Chem Commun, 2014, 50: 8651–8654
- 444 Hermes S, Schröter M, Schmid R, Khodeir L, Muhler M, Tissler A, Fischer RW, Fischer RA. Angew Chem Int Ed, 2005, 44: 6237–6241
- 445 Yang Q, Xu Q, Yu S, Jiang H. Angew Chem Int Ed, 2016, 55: 3685–3689
- 446 Ke F, Wang L, Zhu J. Nano Res, 2015, 8: 1834-1846
- 447 Shen L, Liang S, Wu W, Liang R, Wu L. J Mater Chem A, 2013, 1: 11473–11482
- 448 Qiu X, Zhong W, Bai C, Li Y. J Am Chem Soc, 2016, 138: 1138– 1141
- 449 Feng D, Liu TF, Su J, Bosch M, Wei Z, Wan W, Yuan D, Chen YP, Wang X, Wang K, Lian X, Gu ZY, Park J, Zou X, Zhou HC. Nat Commun, 2015, 6: 5979
- 450 Lykourinou V, Chen Y, Wang XS, Meng L, Hoang T, Ming LJ, Musselman RL, Ma S. J Am Chem Soc, 2011, 133: 10382–10385
- 451 Shi Y, Zhao Z, Yang D, Tan J, Xin X, Liu Y, Jiang Z. Chem Soc Rev, 2023, 52: 6938–6956
- 452 Zhao Z, Ren H, Yang D, Han Y, Shi J, An K, Chen Y, Shi Y, Wang W, Tan J, Xin X, Zhang Y, Jiang Z. ACS Catal, 2021, 11: 9986–9995
- 453 An K, Ren H, Yang D, Zhao Z, Gao Y, Chen Y, Tan J, Wang W, Jiang Z. Appl Catal B-Environ, 2021, 292: 120167
- 454 Xiong Y, Li B, Gu Y, Yan T, Ni Z, Li S, Zuo JL, Ma J, Jin Z. Nat Chem, 2023, 15: 286–293
- 455 Wang F, Zhao D, Li B, Li W, Zhang H, Pang J, Fan L. Cryst Growth Des, 2022, 22: 2775–2792
- 456 Li C, Zhang H, Liu M, Lang FF, Pang J, Bu XH. *Ind Chem Mater*, 2023, 1: 9–38
- 457 Liang Z, Qiu T, Gao S, Zhong R, Zou R. Adv Energy Mater, 2021, 12: 2003410
- 458 Wang Y, Hou P, Wang Z, Kang P. *ChemPhysChem*, 2017, 18: 3142–3147
- 459 Zhao S, Wang Y, Dong J, He CT, Yin H, An P, Zhao K, Zhang X, Gao C, Zhang L, Lv J, Wang J, Zhang J, Khattak AM, Khan NA, Wei Z, Zhang J, Liu S, Zhao H, Tang Z. Nat Energy, 2016, 1: 16184
- 460 Wu Y, Tian J, Liu S, Li B, Zhao J, Ma L, Li D, Lan Y, Bu X. Angew Chem Int Ed, 2019, 58: 12185–12189
- 461 Zhao S, Tan C, He CT, An P, Xie F, Jiang S, Zhu Y, Wu KH, Zhang B, Li H, Zhang J, Chen Y, Liu S, Dong J, Tang Z. Nat Energy, 2020, 5: 881–890
- 462 Ge K, Sun S, Zhao Y, Yang K, Wang S, Zhang Z, Cao J, Yang Y, Zhang Y, Pan M, Zhu L. *Angew Chem Int Ed*, 2021, 60: 12097– 12102
- 463 Li W, Fang W, Wu C, Dinh KN, Ren H, Zhao L, Liu C, Yan Q. J Mater Chem A, 2020, 8: 3658–3666
- 464 Wang CP, Feng Y, Sun H, Wang Y, Yin J, Yao Z, Bu XH, Zhu J. ACS Catal, 2021, 11: 7132–7143
- 465 Wang X, Dong L, Qiao M, Tang Y, Liu J, Li Y, Li S, Su J, Lan Y.
 Angew Chem Int Ed, 2018, 57: 9660–9664
- 466 Li F, Shao Q, Huang X, Lang J. Angew Chem Int Ed, 2018, 57: 1888–1892
- 467 Yi J, Si D, Xie R, Yin Q, Zhang M, Wu Q, Chai G, Huang Y, Cao R. Angew Chem Int Ed, 2021, 60: 17108–17114
- 468 Wang H, Gu M, Huang X, Gao A, Liu X, Sun P, Zhang X. J Mater Chem A, 2023, 11: 7239–7245
- 469 Wang M, Dong R, Feng X. Chem Soc Rev, 2021, 50: 2764-2793
- 470 Liu J, Yang D, Zhou Y, Zhang G, Xing G, Liu Y, Ma Y, Terasaki O, Yang S, Chen L. Angew Chem Int Ed, 2021, 60: 14473–14479
- 471 Huang W, Li J, Liao X, Lu R, Ling C, Liu X, Meng J, Qu L, Lin M, Hong X, Zhou X, Liu S, Zhao Y, Zhou L, Mai L. Adv Mater, 2022, 34: 2200270
- 472 Mu X, Yuan H, Jing H, Xia F, Wu J, Gu X, Chen C, Bao J, Liu S, Mu S. *Appl Catal B-Environ*, 2021, 296: 120095
- 473 Xue Z, Liu K, Liu Q, Li Y, Li M, Su CY, Ogiwara N, Kobayashi H, Kitagawa H, Liu M, Li G. *Nat Commun*, 2019, 10: 5048

- 474 Zhang G, Yang H, Fei H. ACS Catal, 2018, 8: 2519-2525
- 475 Ma W, Wu F, Yu P, Mao L. Chem Sci, 2021, 12: 7908-7917
- 476 Wen L, Sun K, Liu X, Yang W, Li L, Jiang H. Adv Mater, 2023, 35: 2210669
- 477 Chen M, Zhou Y, Ren S B, Wang J. Chin J Struct Chem, 2022, 41: 2212107–2212119
- 478 Chen WJ, Zhang TY, Wu XQ, Li YS, Liu Y, Wu YP, He ZB, Li DS. Chin J Struct Chem, 2023, 42: 100018
- 479 Huang J, Chang K, Liu Q, Xie Y, Song Z, Zheng Z, Kuang Q. Chin J Struct Chem, 2023, 42: 100097
- 480 Wei YS, Zhang M, Zou R, Xu Q. Chem Rev, 2020, 120: 12089–12174
- 481 Paitandi RP, Wan Y, Aftab W, Zhong R, Zou R. Adv Funct Mater, 2022. 33: 2203224
- 482 Wan Y, Chen W, Wu S, Gao S, Xiong F, Guo W, Feng L, Cai K, Zheng L, Wang Y, Zhong R, Zou R. Adv Mater, 2024, 36: e2308798
- 483 Wei S, Yang R, Wang Z, Zhang J, Bu XH. Adv Mater, 2024, 36: e2404692
- 484 Zhang Y, Liu M, Zhang L, Lu N, Wang X, Li Z, Zhang X, Li N, Bu X. Adv Funct Mater, 2024, 34: 2412406
- 485 Liu M, Wang X, Cao S, Lu X, Li W, Li N, Bu XH. *Adv Mater*, 2024, 36: e2309231
- 486 Zhang W, Xia Y, Chen S, Hu Y, Yang S, Tie Z, Jin Z. *Nano Lett*, 2022, 22: 3340–3348
- 487 Chen S, Li W, Jiang W, Yang J, Zhu J, Wang L, Ou H, Zhuang Z, Chen M, Sun X, Wang D, Li Y. Angew Chem Int Ed, 2022, 61: e202114450
- 488 Yi J, Xie R, Xie Z, Chai G, Liu T, Chen R, Huang Y, Cao R. *Angew Chem Int Ed*, 2020, 59: 23641–23648
- 489 Kusama S, Saito T, Hashiba H, Sakai A, Yotsuhashi S. ACS Catal, 2017, 7: 8382–8385
- 490 Qiu X, Huang J, Yu C, Zhao Z, Zhu H, Ke Z, Liao P, Chen X. Angew Chem Int Ed, 2022, 61: e202206470
- 491 Qiu XF, Zhu HL, Huang JR, Liao PQ, Chen XM. J Am Chem Soc, 2021, 143: 7242–7246
- 492 Liu C, Zhang XD, Huang JM, Guan MX, Xu M, Gu ZY. ACS Catal, 2022, 12: 15230–15240
- 493 Wen CF, Zhou M, Liu PF, Liu Y, Wu X, Mao F, Dai S, Xu B, Wang XL, Jiang Z, Hu P, Yang S, Wang HF, Yang HG. Angew Chem Int Ed, 2022, 61: e202111700
- 494 Nie M, Sun H, Lei D, Kang S, Liao J, Guo P, Xue Z, Xue F. Mater Chem Phys, 2020, 254: 123481
- 495 Liu T, Li P, Yao N, Cheng G, Chen S, Luo W, Yin Y. Angew Chem Int Ed, 2019, 58: 4679–4684
- 496 Wang L, Wu Y, Cao R, Ren L, Chen M, Feng X, Zhou J, Wang B. ACS Appl Mater Interfaces, 2016, 8: 16736–16743
- 497 Duan J, Chen S, Zhao C. Nat Commun, 2017, 8: 15341
- 498 Zhang L, Chen J, Huang W, Hu Y, Cheng J, Chen Y. J Electrochem, 2019, 25: 511–521
- 499 Sun X, Li Y, Su H, Zhang X, Xu Y, Zhou W, Liu M, Cheng W, Liu Q. Appl Catal B-Environ, 2022, 317: 121706
- 500 Chang H, Guo YF, Liu X, Wang PF, Xie Y, Yi TF. *Appl Catal B-Environ*, 2023, 327: 122469
- 501 Zhao R, Liang Z, Zou R, Xu Q. Joule, 2018, 2: 2235-2259
- 502 Kong L, Cheng M, Huang H, Pang J, Liu S, Xu Y, Bu XH. *EnergyChem*, 2022, 4: 100090
- 503 Qiu T, Liang Z, Guo W, Tabassum H, Gao S, Zou R. ACS Energy Lett, 2020, 5: 520–532
- 504 Yin J, Lian X, Li Z, Cheng M, Liu M, Xu J, Li W, Xu Y, Li N, Bu X. Adv Funct Mater, 2024, 34: 2403656
- 505 Kong L, Liu M, Huang H, Xu Y, Bu XH. Adv Energy Mater, 2022, 12: 2100172
- 506 Jiang Q, Xiong P, Liu J, Xie Z, Wang Q, Yang X, Hu E, Cao Y, Sun J, Xu Y, Chen L. *Angew Chem Int Ed*, 2020, 59: 5273–5277
- 507 Zhang L, Liu Y, Zhao Z, Jiang P, Zhang T, Li M, Pan S, Tang T, Wu T, Liu P, Hou Y, Lu H. ACS Nano, 2020, 14: 8495–8507
- 508 Jiang H, Liu X, Wu Y, Shu Y, Gong X, Ke F, Deng H. Angew Chem

- Int Ed., 2018, 57: 3916-3921
- 509 Mao Y, Li G, Guo Y, Li Z, Liang C, Peng X, Lin Z. Nat Commun, 2017, 8: 14628
- 510 Wu D, Guo Z, Yin X, Pang Q, Tu B, Zhang L, Wang YG, Li Q. Adv Mater, 2014, 26: 3258–3262
- 511 Ren W, Qin M, Zhu Z, Yan M, Li Q, Zhang L, Liu D, Mai L. Nano Lett, 2017, 17: 4713–4718
- 512 Sang Z, Liu J, Zhang X, Yin L, Hou F, Liang J. *ACS Nano*, 2023, 17: 3077–3087
- 513 Su Y, Hu J, Yuan G, Zhang G, Wei W, Sun Y, Zhang X, Liu Z, Suen NT, Chen HC, Pang H. *Adv Mater*, 2023, 35: e2307003
- 514 Chen T, Wang F, Cao S, Bai Y, Zheng S, Li W, Zhang S, Hu SX, Pang H. *Adv Mater*, 2022, 34: e2201779
- 515 Li X, Cheng F, Zhang S, Chen J. *J Power Sources*, 2006, 160: 542–547
- 516 Lu Y, Zhang Q, Chen J. Sci China Chem, 2019, 62: 533-548
- 517 Zhou D, Ni J, Li L. Nano Energy, 2019, 57: 711-717
- 518 Cao K, Jiao L, Xu H, Liu H, Kang H, Zhao Y, Liu Y, Wang Y, Yuan H. *Adv Sci*, 2016, 3: 1500185

- 519 Liang Y, Song N, Zhang Z, Chen W, Feng J, Xi B, Xiong S. Adv Mater, 2022, 34: e2202673
- 520 Liu ST, Zhou JS, Song HH. Adv Energy Mater, 2018, 8: 9
- 521 Zhang C, Shen L, Shen J, Liu F, Chen G, Tao R, Ma S, Peng Y, Lu Y. *Adv Mater*, 2019, 31: e1808338
- 522 Gao G, Wang Y, Wang S, Yang R, Chen Y, Zhang Y, Jiang C, Wei M, Ma H, Lan Y. *Angew Chem Int Ed*, 2021, 60: 10147–10154
- 523 Li Y, Lin S, Wang D, Gao T, Song J, Zhou P, Xu Z, Yang Z, Xiao N, Guo S. Adv Mater, 2020, 32: e1906722
- 524 Xu B, Zhang H, Mei H, Sun D. Coord Chem Rev, 2020, 420: 213438
- 525 Yang J, Xiong P, Zheng C, Qiu H, Wei M. *J Mater Chem A*, 2014, 2: 16640–16644
- 526 Li W, Ding K, Tian H, Yao M, Nath B, Deng W, Wang Y, Xu G. Adv Funct Mater, 2017, 27: 1702067
- 527 Wang L, Feng X, Ren L, Piao Q, Zhong J, Wang Y, Li H, Chen Y, Wang B. J Am Chem Soc, 2015, 137: 4920–4923
- 528 Liu C, Bai Y, Li W, Yang F, Zhang G, Pang H. *Angew Chem Int Ed*, 2022, 61: e202116282